Cell Reports

Article

Modeling iPSC-derived human neurofibroma-like tumors in mice uncovers the heterogeneity of Schwann cells within plexiform neurofibromas

Graphical abstract

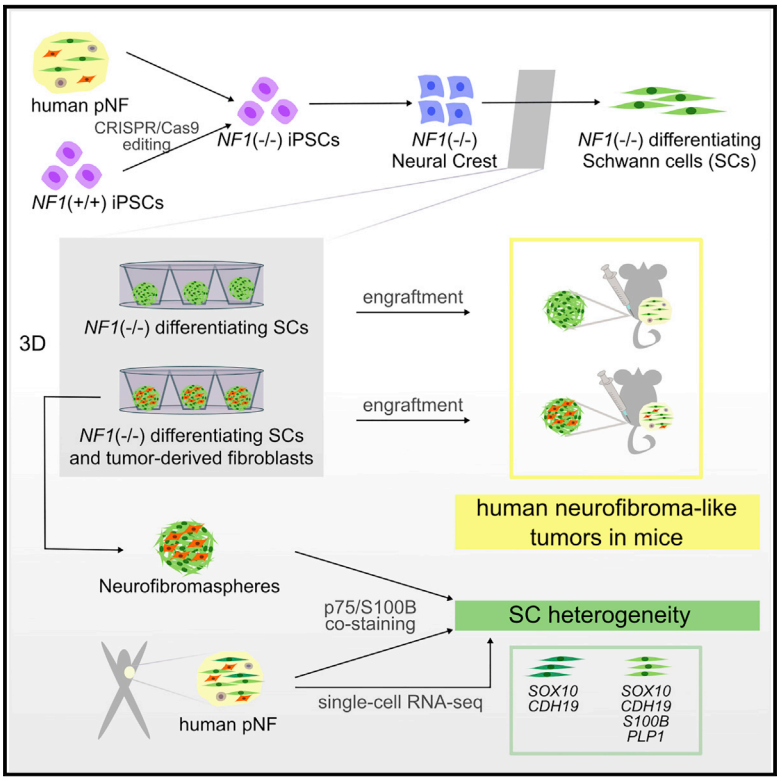

Highlights

- Development of an iPSC-based *in vitro*/*in vivo* 3D model system for neurofibromas
- Importance of SC-SC and SC-fibroblast interactions for neurofibroma formation
- Expression roadmap of the NC-SC *in vitro* differentiation axis
- Cells at different maturation states along the NC-SC axis compose neurofibromas

Authors

Helena Mazuelas, Míriam Magallón-Lorenz, Juana Fernández-Rodríguez, ..., Bernat Gel, Meritxell Carrió, Eduard Serra

Correspondence

eserra@igtp.cat (E.S.), mcarriol@igtp.cat (M.C.), bgel@igtp.cat (B.G.)

In brief

Mazuelas et al. develop an *in vitro*/*in vivo* model for human neurofibromas, consisting of an admixture of iPSC-derived differentiating *NF1*(−/−) Schwann cells (SCs) with *NF1*(+/−) neurofibroma-derived fibroblasts. They identify that plexiform neurofibromas are made up of cells at different maturation states along the neural crest (NC)-SC axis.

Mazuelas et al., 2022, Cell Reports *38*, 110385
February 15, 2022
https://doi.org/10.1016/j.celrep.2022.110385

Cell Reports

CellPress
OPEN ACCESS

Article

Modeling iPSC-derived human neurofibroma-like tumors in mice uncovers the heterogeneity of Schwann cells within plexiform neurofibromas

Helena Mazuelas,[1] Míriam Magallón-Lorenz,[1] Juana Fernández-Rodríguez,[2,12] Itziar Uriarte-Arrazola,[1] Yvonne Richaud-Patin,[3,4] Ernest Terribas,[1,12] Alberto Villanueva,[5] Elisabeth Castellanos,[6,7] Ignacio Blanco,[6,7] Ángel Raya,[3,4,8] Jakub Chojnacki,[9] Holger Heyn,[10,13] Cleofé Romagosa,[11,12] Conxi Lázaro,[2,12] Bernat Gel,[1,*] Meritxell Carrió,[1,14,*] and Eduard Serra[1,12,14,15,*]

[1]Hereditary Cancer Group, Germans Trias i Pujol Research Institute (IGTP), Can Ruti Campus, Badalona, 08916 Barcelona, Spain
[2]Hereditary Cancer Program, Catalan Institute of Oncology (ICO-IDIBELL), L'Hospitalet de Llobregat, 08098 Barcelona, Spain
[3]Regenerative Medicine Program, Bellvitge Institute for Biomedical Research (IDIBELL) and Program for Clinical Translation of Regenerative Medicine in Catalonia (P-CMRC), L'Hospitalet de Llobregat, 08098 Barcelona, Spain
[4]Center for Networked Biomedical Research on Bioengineering, Biomaterials, and Nanomedicine (CIBER-BBN), 28029 Madrid, Spain
[5]Procure Program, Catalan Institute of Oncology (ICO), L'Hospitalet de Llobregat, 08098, Barcelona, Spain
[6]Clinical Genomics Research Unit, Germans Trias i Pujol Research Institute (IGTP), Can Ruti Campus, Badalona, Barcelona, Spain
[7]Clinical Genetics Service, Northern Metropolitan Clinical Laboratory, Germans Trias i Pujol University Hospital (HGTP), Can Ruti Campus, Badalona, Barcelona, Spain
[8]Catalan Institution for Research and Advanced Studies (ICREA), 08010 Barcelona, Spain
[9]IrsiCaixa AIDS Research Institute, Can Ruti Campus, Badalona, 08916 Barcelona, Spain
[10]Centre for Genomic Regulation (CNAG-CRG), Barcelona Institute of Science and Technology (BIST), 08028 Barcelona, Spain
[11]Department of Pathology, Vall d'Hebron University Hospital (VHIR-CIBERONC), Barcelona, Spain
[12]Centro de Investigación Biomédica en Red de Cáncer (CIBERONC), Madrid, Spain
[13]Universitat Pompeu Fabra (UPF), Barcelona, Spain
[14]These authors contributed equally
[15]Lead contact
*Correspondence: eserra@igtp.cat (E.S.), mcarriol@igtp.cat (M.C.), bgel@igtp.cat (B.G.)
https://doi.org/10.1016/j.celrep.2022.110385

SUMMARY

Plexiform neurofibromas (pNFs) are developmental tumors that appear in neurofibromatosis type 1 individuals, constituting a major source of morbidity and potentially transforming into a highly metastatic sarcoma (MPNST). pNFs arise after *NF1* inactivation in a cell of the neural crest (NC)-Schwann cell (SC) lineage. Here, we develop an iPSC-based NC-SC *in vitro* differentiation system and construct a lineage expression roadmap for the analysis of different 2D and 3D NF models. The best model consists of generating heterotypic spheroids (neurofibromaspheres) composed of iPSC-derived differentiating *NF1*(−/−) SCs and *NF1*(+/−) pNF-derived fibroblasts (Fbs). Neurofibromaspheres form by maintaining highly proliferative *NF1*(−/−) cells committed to the NC-SC axis due to SC-SC and SC-Fb interactions, resulting in SC linage cells at different maturation points. Upon engraftment on the mouse sciatic nerve, neurofibromaspheres consistently generate human NF-like tumors. Analysis of expression roadmap genes in human pNF single-cell RNA-seq data uncovers the presence of SC subpopulations at distinct differentiation states.

INTRODUCTION

Neurofibromatosis type 1 (NF1) is a tumor predisposition genetic disease affecting ~1 in 3,500 people worldwide, caused by the inheritance of a mutated copy of the *NF1* tumor suppressor gene (Riccardi, 1992). Different types of pathogenic variants (e.g., splicing, frameshift, nonsense) can be located across the entire *NF1* coding region (Messiaen, 2020). The major clinical manifestations of the disease involve the nervous system, the skin, and the skeletal system, implicating cells derived from the neural crest (NC). The development of different tumors of the peripheral nervous system, such as cutaneous neurofibromas (cNFs), plexiform NFs (pNFs), atypical NFs (aNFs), or malignant peripheral nerve sheath tumors (MPNSTs), constitutes one of the hallmarks of the disease (Ferner et al., 2007).

pNFs are large NF lesions that initiate during development and grow along large nerves. A pNF may be visible or may lie internally and is normally diagnosed in early childhood (Dombi et al., 2007; Tucker et al., 2009; Akshintala et al., 2020). pNFs constitute a major source of morbidity for NF1 patients (Prada et al., 2012) and, in some cases, may undergo malignant transformation to an MPNST (Ducatman et al., 1986; McCarron and

Goldblum, 1998). The MEK inhibitor (MEKi) selumetinib reduces tumor volume in ~70% of children with inoperable disease, lowering their pain and improving their quality of life (Dombi et al., 2016; Gross et al., 2020). However, despite their benign nature, there is no complete curative approach for pNFs, which underscores a lack of fundamental understanding of the cells composing these tumors.

The identity of the cell that originates pNFs and its impact on tumor formation, composition, and treatment response is still being investigated. During embryo development, NC cells differentiate into Schwann cells (SCs) in a multistep differentiation process, involving the generation of an intermediate cell population called SC precursors (SCPs), which can differentiate into immature SCs, that will finally form myelinating or non-myelinating SCs (Jessen and Mirsky, 2005; Woodhoo and Sommer, 2008; Monk et al., 2015; Kastriti and Adameyko, 2017). Different markers have been identified to characterize the NC-SC differentiation axis (Jessen and Mirsky, 2005). However, their informativity regarding the precise identity of the different cell stages along this differentiation axis is still quite limited.

NFs are composed of different cell types, mainly *NF1*(−/−) SCs and *NF1*(+/−) fibroblasts (Fbs), but also perineurial cells, infiltrating immune cells, axons, and others that are embedded in an abundant collagen-rich extracellular matrix (Krone et al., 1983; Peltonen et al., 1986). Most of what we know about the pNF cell of origin comes from genetically modified mouse models (GEMMs) (reviewed in Buchstaller et al., 2012a; Li et al., 2019). Different GEMMs that develop pNFs have been generated using the Cre-loxP system to ablate the *Nf1* gene in specific developmental cell stages of the NC-SC axis (Zhu et al., 2002; Joseph et al., 2008; Wu et al., 2008; Zheng et al., 2008; Chen et al., 2019). In addition, the transplantation of *Nf1*-deficient embryonic dorsal root ganglia/nerve root neurospheres to the sciatic nerves of nude mice also generates pNFs (Chen et al., 2014). NC cells give rise to SCPs, satellite cells, and boundary cap (BC) cells. Ablation of *Nf1* in Prss56-expressing BC cells generated both cNF and pNF tumors (Radomska et al., 2019). These models point to an SCP deriving from the BC (Radomska and Topilko, 2017) as the most probable pNF cell of origin.

In clear contrast, there is a lack of human models for pNFs, especially those amenable to combined *in vitro* and *in vivo* use. NF-derived primary SCs have a limited life span (Rosenbaum et al., 2000; Serra et al., 2000; Wallace et al., 2000), and their immortalization (Li et al., 2016) implies an alteration of their physiology. In addition, the engraftment of these cells in the sciatic nerves of nude mice has a very limited expansion capacity, as occurs for the engraftment of pieces of pNF tumors, in contrast to their MPNST counterparts, for which many xenografts have been generated, expanded, and preserved (Castellsagué et al., 2015; Fernández-Rodríguez et al., 2020).

Induced pluripotent stem cells (iPSCs) have been generated to model NF1 disease (Wegscheid et al., 2018). Our group demonstrated that pNF-derived *NF1*(−/−) cells can be reprogrammed and has successfully generated isogenic *NF1*(+/−) and *NF1*(−/−) iPSC lines from different pNFs (Carrió et al., 2019). These cells represent a non-perishable iPSC-based model system for the study of pNFs. We showed that control *NF1*(+/+) and pNF-derived iPSCs could be efficiently differentiated toward NC and homogenously expressed NC lineage markers, and these iPSCs were able to undergo further differentiation into NC-derived cell types (peripheral neurons, melanocytes, and SCs), indicating a clear NC identity that is independent of the iPSC *NF1* genotype. In contrast, while *NF1*(+/+) cells can fully differentiate into myelinating SCs when co-cultured with neurons, *NF1*(−/−) differentiating SCs exhibited a high proliferation rate, a poor differentiation capacity, and a tendency to form spheroids that recapitulate pNF marker expression (Carrió et al., 2019). Recently, Mo et al. (2020) generated *NF1*(−/−) SC lineage cells from iPSCs that formed neurofibromas when implanted within the sciatic nerves of mice. Tumor-forming cells were identified as SOX10^{+}. Since SOX10 is expressed along the whole NC-SC axis, further characterization is required to narrow the window within the differentiation lineage and to better understand its cell identity and properties.

In the present study, we investigated the suitability of different *in vitro* iPSC-based *NF1*(−/−) models to generate human NF tumors when engrafted in the sciatic nerves of nude mice. A heterotypic spheroid system composed of iPSC-derived differentiating SCs and pNF-derived Fbs (neurofibromaspheres) was the most robust NF-forming model. We performed an in-depth characterization of neurofibromaspheres comparing the cell expression and heterogeneity of the NC-SC lineage with primary pNFs.

RESULTS

We have previously generated several *NF1*(−/−) and (+/−) iPSC lines by reprogramming pNF-derived cells and have set up conditions to differentiate them into NC cells and then further into SCs (Carrió et al., 2019). We validated the *in vitro* NC-SC differentiation system using control *NF1*(+/+) cells and analyzed the expression of classic markers of the NC-SC differentiation axis (Jessen and Mirsky, 2005).

The generation of an expression roadmap of the *in vitro* NC-SC differentiation axis expands the palette of NC-SC markers

We aimed to better understand pNF formation and cellular composition by developing an *in vitro/in vivo* human pNF model system. We started by extending the expression characterization of the different stages and differentiation time points of the NC-SC axis by RNA sequencing (RNA-seq) analysis. Control *NF1*(+/+) (wild-type [WT]) iPSCs were differentiated into NC cells and then further into SCs. NC cells represented a stable cell stage, co-expressing high levels of Hnk1 and p75 markers in >90% of the cell population, and being amenable to multiple passages without losing marker expression and potency (Carrió et al., 2019). On the contrary, NC cells differentiating into SCs for 30 days generated a continuum of cells that progressed from a precursor state into a committed SC phenotype, according to the acquisition of NC-SC markers (Jessen and Mirsky, 2005), without reaching a mature myelinating phenotype unless co-cultured with neurons (Carrió et al., 2019). To better characterize the *in vitro* NC-SC differentiation process, different time points along the NC-SC axis were sampled for control *NF1*(+/+) cells (at 7, 14, and 30 days, after the induction of SC differentiation)

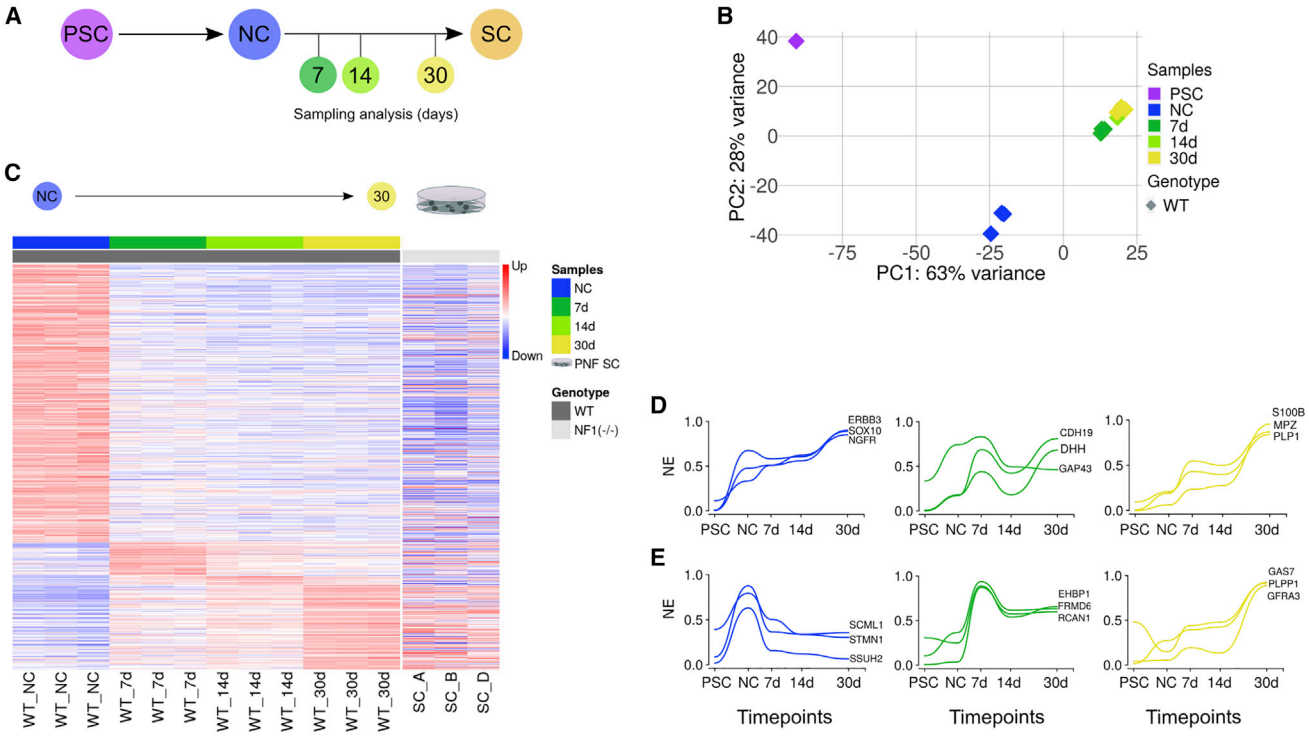

Figure 1. Generation of an expression roadmap of the *in vitro* NC-SC differentiation axis using *NF1*(+/+) cells

(A) Schematic representation of the *in vitro* NC-SC differentiation protocol from pluripotent stem cells (PSCs). Samples were collected at the PSC and NC stages, and at 7, 14, and 30 days after SC differentiation for RNA-seq analysis.

(B) Principal-component analysis of the *in vitro* PSC-NC-SC differentiation process of *NF1*(+/+) cells. Three differentiation experiments are shown compared to a PSC sample.

(C) *In vitro* NC-SC expression roadmap. Heatmap representing the differentially upregulated genes (adjusted $p < 0.05$) in each stage/time point throughout the NC-SC differentiation process of *NF1*(+/+) cells (wild type [WT]). Three independent differentiation experiments, and 3 different pNF-derived SC cultures (SC_A, SC_B, and SC_D) were analyzed. See also Data S1.

(D and E) Expression plots of selected classic (D) and roadmap (E) NC-SC markers along the PSC-NC-SC *in vitro* differentiation process. Data represent the mean of 3 independent differentiation experiments. See also Figure S1.

NC, neural crest; SC, Schwann cell.

(Figure 1A), and bulk RNA-seq analysis was performed. A principal-component analysis (PCA) validated the robustness of the differentiation protocol, as triplicates of the same cell state clustered together (Figure 1B). The variance captured in PC1 faithfully reproduced the NC-SC *in vitro* differentiation process over time (Figure 1B). We then performed a differential expression analysis considering the distinct differentiation stages and time points. Differentially upregulated genes in each stage/time point were grouped to construct an expression roadmap of the NC-SC *in vitro* differentiation process (Data S1). A heatmap representing a supervised cluster analysis of this expression roadmap is shown in Figure 1C. The expression roadmap was consistent among the three independent differentiation assays, drawing a temporal continuum throughout SC differentiation. The expression profile of three patient pNF-derived SC cultures indicated a signature closer to that expressed by *NF1*(+/+) SCs at 30 days of differentiation, although they also expressed genes upregulated at NC and other SC time points (7 and 14 days) (Figure 1C). Thus, the roadmap gene signature strengthened the validity of the established *in vitro* NC-SC differentiation assay and uncovered potential new markers of the NC-SC differentiation axis (Data S1). In this regard, we compared expression curves along the NC-SC temporal axis of already established (classic, from now on) markers such as *SOX10*, *ERBB3*, *NGFR*, *CDH19*, *DHH*, *GAP43*, *S100B*, *MPZ*, and *PLP1* (Figures 1D and S1) and of newly selected genes from the expression roadmap (Figures 1E and S1), such as *SCML1*, *SSUH2*, *STMN1*, *EHBP1*, *FRND6*, *RCAN1*, *GAS7*, *GFRA3*, and *PLPP1*. The expression of these roadmap genes (and many others) (Data S1) was also present in the SC component of pNFs (see below), and they may emerge as new markers of the NC-SC axis.

NF1(−/−) differentiating SCs in 2D cultures switch from an NC-SC axis to an NC-mesenchymal path

The *in vitro* NC-SC expression roadmap generated using *NF1*(+/+) cells facilitated the analysis of the *NF1* role along the NC-SC differentiation route. To obtain a thorough characterization of *NF1*-deficient cells, we generated a new *NF1*-deficient iPSC line that, in addition to the two already existing pNF-derived *NF1*(−/−) iPSC lines from two different patients (NF1_A and NF1_B), formed

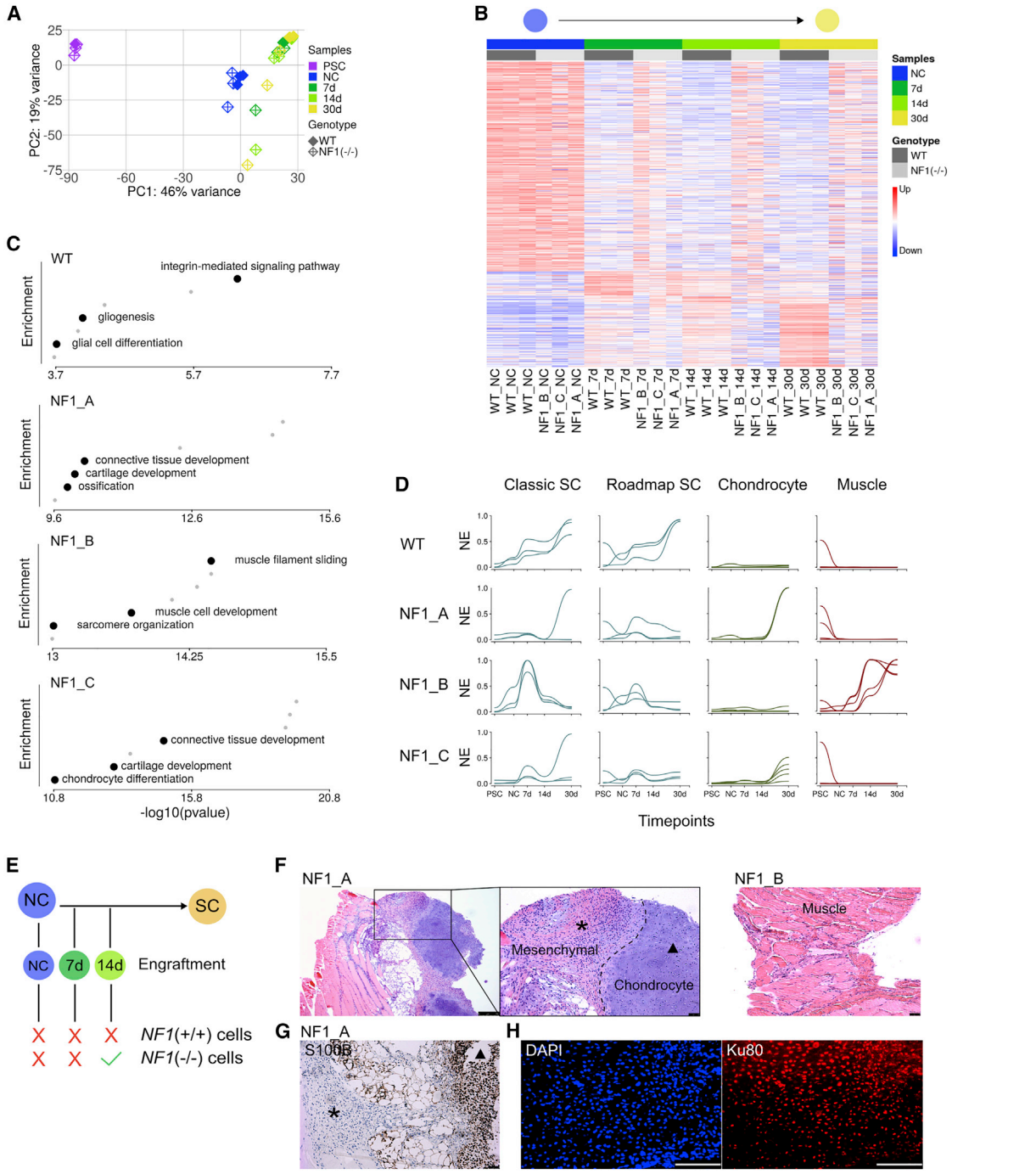

Figure 2. *NF1*(−/−) differentiating SCs in 2D cultures acquire an NC-mesenchymal path

(A) Principal-component analysis of the *in vitro* PSC-NC-SC differentiation process comparing 3 differentiation experiments from *NF1*(+/+) (WT) cells with 3 independent *NF1*(−/−) cell lines (NF1_A, NF1_B, and NF1_C).

(B) Heatmap representing the *in vitro* NC-SC expression roadmap comparing 3 differentiation experiments from *NF1*(+/+) WT cells with 3 independent *NF1*(−/−) cell lines (NF1_A, NF1_B, and NF1_C).

(C) Enrichment analysis of expression profiles at 30 days under SC differentiation conditions, showing enriched biological processes (adjusted $p < 0.05$) in *NF1*(+/+) (WT) and in the 3 independent *NF1*(−/−) cell lines. See also Data S2 and S3.

(D) Expression of selected SC (classic or roadmap), chondrocytes, or muscle markers along the PSC-NC-SC *in vitro* differentiation process for WT and *NF1*(−/−) cell lines. WT: Mean of 3 differentiation experiments; *NF1*(−/−): 3 biological replicates; values of each cell line are graphed separately. See also Figure S4.

(legend continued on next page)

a biological triplicate. The new *NF1*(−/−) iPSC line (NF1_C) was generated by editing the *NF1* gene by CRISPR-Cas9 in control *NF1*(+/+) fibroblast induced pluripotent stem cell line (FiPS) (Figure S2). NF1_C exhibited the same functional characteristics as the pNF-derived *NF1*(−/−) iPSCs: an increased proliferation capacity compared with controls; a genuine generation of NC cells; and, when differentiating toward SCs, a higher proliferation rate, an altered differentiation capacity, and a tendency to form spheres (Figure S3). These results demonstrated that, thus far, all of the altered proliferation and differentiation properties of *NF1*(−/−) iPSC and iPSC-derived SCs can be attributed to the lack of neurofibromin function.

We then differentiated the three *NF1*(−/−) iPSC lines to NC and further to SCs. Differentiating SCs were collected at 7, 14, and 30 days throughout the process and split to analyze both their transcriptome and their capacity to form NFs upon sciatic nerve engraftment in mice. Using RNA-seq data, a PCA containing both *NF1*(+/+) and *NF1*(−/−) triplicates showed a similar expression of cells with both genotypes at the NC stage, but revealed an altered SC differentiation capacity of *NF1*(−/−) cells compared with controls, and a substantial degree of variation among the three *NF1*(−/−) cell lines (Figure 2A). We visually compared the expression roadmap signature in control and *NF1*-deficient cells (Figure 2B). The heatmap generated showed a highly similar expression profile of cells from both *NF1* genotypes at the NC stage. However, as early as at 7 days of SC differentiation, *NF1*(−/−) cells exhibited an altered NC-SC pattern of differentiation according to the roadmap signature (Figure 2B). Gene enrichment analysis of expression profiles at 30 days of differentiation indicated an enrichment in biological processes related to glial cell differentiation, SC differentiation, and peripheral nervous system development in *NF1*(+/+) cells (Figure 2C). In *NF1*(−/−) cells, enriched biological processes were related to muscle cell development and differentiation (NF1_B) or cartilage development and chondrocyte differentiation (NF1_A and NF1_C) (Figure 2C; Data S2 and S3). Different muscle- and chondrocyte-specific genes, together with classic and roadmap SC markers, were selected to plot their expression along the temporal axis of NC differentiation (Figures 2D and S4). These analyses showed that while WT *NF1*(+/+) cells remained in the NC-SC differentiation axis, the same *in vitro* conditions led *NF1*(−/−) cells to take a different path (Figures 2C and 2D).

In parallel to RNA-seq analysis, we performed an *in vivo* experiment and injected the same *NF1*(+/+) and *NF1*(−/−) cells (NF1_A and NF1_B) in contact with the sciatic nerves of nude mice. Since *NF1*(−/−) cells able to generate NFs are presumed to be in a precursor state (Buchstaller et al., 2012a), we injected cells at the NC stage and early SC differentiation time points (at 7 and 14 days) (Figure 2E). None of the *NF1*(+/+) cells at any differentiation stage or time point (NC, 7 or 14 days of SC differentiation) were able to generate an engrafted cell mass. We only observed the formation of tumor-like masses in mice injected with *NF1*(−/−) cells at 14 days of SC differentiation (not at the NC stage, nor at 7 days of SC differentiation) (Figure 2E). Histological analysis of these tumor-like masses mostly revealed the presence of mesenchymal-like cells (negative for S100B) and areas of chondrocytes (positive for S100B) (NF1_A) and muscle cells (NF1_B) (Figures 2F and 2G), which were positive for the human-specific antibody Ku80 (Figure 2H), indicating that they originated from the engrafted *NF1*(−/−) cells. These results demonstrated that *NF1*(−/−) cells differentiating toward SCs in 2D cultures acquired an altered path of differentiation (toward chondrocytes and muscle cells), both *in vitro* and *in vivo*. Results also support the lack of capacity of *NF1*(−/−) NC cells to form NFs as reported for GEMMs (Joseph et al., 2008). Moreover, these results highlight a strong correlation between the expression identity acquired *in vitro* by differentiating cells and the cell type developed *in vivo* after engraftment.

In vitro 3D homotypic and heterotypic pNF model systems preserve the expression of markers of the NC-SC axis

The adoption of a majority of *NF1*(−/−) differentiating SCs in 2D cultures of an NC-mesenchymal cell differentiation axis and the high tendency of *NF1*(−/−) differentiating SCs to form spheres that better recapitulate pNF-derived SC expression (Carrió et al., 2019) prompted us to improve our iPSC-derived pNF model system by setting up a 3D NC-SC differentiation protocol (Figure 3A). NC cells were subjected to SC differentiation in 2D culture conditions for 5 days. Then, differentiating SCs were seeded in uncoated culture plates (AggreWell 800) for spheroid generation. They were cultured in SC differentiating media until day 14, the only time point at which 2D cultures were able to generate tumor growths upon nerve injection. The format of the culture plates allowed the generation of hundreds of individual spheroids at the same time and in the same culture well (Figure 3B).

We generated two types of spheroids: homotypic, containing only differentiating SCs, and heterotypic, containing both differentiating SCs (70%) and *NF1*(+/−) pNF-derived Fbs (30%) (Figure 3C). The latter was meant to provide a pNF-like microenvironment component to differentiating SCs. *NF1*(+/+) differentiating SCs alone only generated very small and inconsistent spheroids, which are not suitable for experimentation. Instead, *NF1*(−/−) homotypic spheroids were able to grow, forming spheres of ∼200 μm in diameter on average (n = 40 spheroids) (Figure 3D). Contrary to homotypic spheroids, *NF1*(+/+) heterotypic spheroids were able to consistently form

(E) Schematic representation of the engraftment experiment. 2 × 10^6 *NF1*(+/+) or *NF1*(−/−) differentiating cells were injected at the NC stage and at 7 and 14 days of SC differentiation in contact with the sciatic nerves of nude mice. After 4 months, mice were sacrificed and tumors were excised and processed. N = 2 mice per experimental group and stage, 2 injections per mouse: 1 *NF1*(+/+) and 2 *NF1*(−/−) cell lines (NF1_A and NF1_B).

(F) H&E-stained tumors containing areas of mesenchymal-like cells (asterisk), chondrocytes (triangle), and muscle cells. Scale bar: 250 μm (left panel), 50 μm (inset and right panel).

(G) S100B immunohistochemistry from paraffin sections showing no expression of this marker in mesenchymal-like cells (asterisk) and expression in chondrocytes (triangle). Scale bar: 50 μm.

(H) Ku80 immunofluorescence staining from OCT sections, showing that tumors were derived from human-engrafted cells. Scale bar: 100 μm.

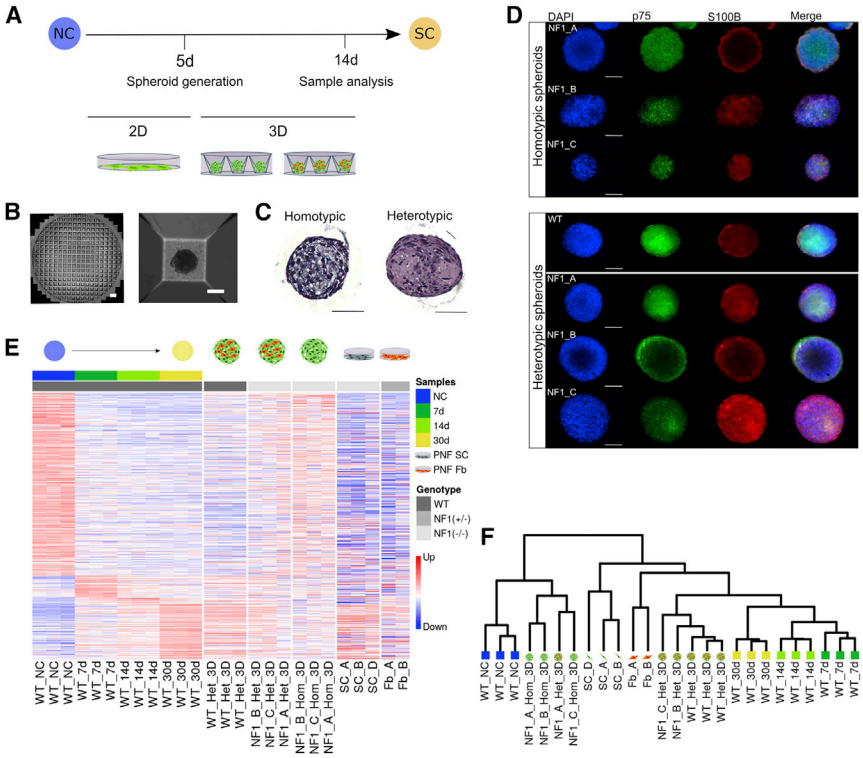

Figure 3. Homotypic and heterotypic spheroids preserve the expression of markers of the NC-SC axis

(A) Schematic representation of the 3D *in vitro* NC-SC differentiation protocol.

(B) Left: Micrograph of 1 Aggrewell containing 300 microwells with 1 spheroid per well. Scale bar: 1 mm. Right: detail of a representative spheroid. Scale bar: 100 μm.

(C) H&E-stained *NF1*(−/−) homotypic (left) and heterotypic (right) spheroids from paraffin sections. Scale bar: 50 μm.

(D) Representative immunofluorescence images showing p75 and S100B expression in homotypic and heterotypic spheroids. Scale bar: 100 μm.

(E) Heatmap representing the *in vitro* NC-SC expression roadmap of *NF1*(+/+) WT cells in 2D conditions compared to 3D homotypic and heterotypic spheroids, either *NF1*(+/+) (WT) or *NF1*(−/−) (NF1). Roadmap expression profiles of pNF-derived primary SCs and Fbs are also shown. See also Figure S5 and Data S4.

(F) Dendrogram computed using Euclidean distances showing an unsupervised hierarchical clustering of samples in (E).

firm spheroids of 200–300 μm in diameter (n = 40 spheroids). *NF1*(−/−) heterotypic spheroids also formed easily, being 200–350 μm in size (n = 40 spheroids; Figure 3D).

To gain global insight on the identity of the cells composing the spheroids, we performed RNA-seq analysis, comparing those generated from *NF1*(+/+) cells with the three independent *NF1*(−/−) cell lines. We then analyzed the expression roadmap for all of them (Figure 3E). *NF1*(+/+) heterotypic spheroids exhibited an expression profile of roadmap genes closer to that displayed by *NF1*(+/+) differentiating SCs at 30 days in 2D cultures and by pNF-derived SC cultures (Figure 3E), confirmed by an unsupervised cluster analysis (Figure 3F). Remarkably, two of the *NF1*(−/−) heterotypic spheroid lines (NF1_B and NF1_C) also expressed a similar expression roadmap profile (Figure 3E) and also clustered together (Figure 3F). However, this was not the case for the third *NF1*(−/−) heterotypic spheroid line (NF1_A), and for none of the three homotypic spheroid cultures, that expressed a roadmap profile resembling a less differentiated state (closer to the NC stage), despite the detection of classic markers (p75, S100B) by immunostaining (Figure 3D). All of these samples also clustered together in an unsupervised cluster analysis (Figure 3F). NF1_B and NF1_C heterotypic spheroids, despite exhibiting a roadmap expression profile closely resembling *NF1*(+/+) differentiating SCs at 30 days, also expressed genes at the NC stage and at 7 and 14 days of SC differentiation (Data S4). The expression of classic and roadmap NC-SC markers in 3D models indicated that contrary to 2D *in vitro* conditions, *NF1*(−/−) differentiating cells in 3D conditions followed an NC-SC axis of differentiation (Figure S5).

Engraftment of heterotypic 3D spheroids in mouse sciatic nerve consistently generates human NF-like tumors

In parallel to the RNA-seq characterization of homotypic and heterotypic spheroids, we used the same spheroids to evaluate their capacity to engraft and form tumors *in vivo.* Spheroids representing ∼2 million cells were injected in contact with the sciatic nerves of nude mice. Homotypic and heterotypic spheroids generated from the same *NF1*(−/−) cell line were injected in the left and right sciatic nerve of the same mouse, respectively. pNF-derived Fbs used for the formation of heterotypic spheroids were also injected as a control for their capacity to engraft and generate cell masses as single cultures. After 4 months, mice were euthanized and tumors were excised and analyzed. One mouse was euthanized 2 weeks earlier due to a prominent growth in the right leg that impaired its movement (B1 mice; Table S2). Table S1 summarizes the overall results of the *in vivo* experiment indicating the number of mice used for each condition and the number of tumors obtained. None of the *NF1*(+/+) heterotypic spheroid cultures were able to generate a tumor or cell mass outgrowth in the injected area, nor did the pNF-derived Fbs alone. In clear contrast, both *NF1*(−/−) homotypic and heterotypic spheroids were able to engraft, grow, and generate tumor masses containing areas of *bona fide* NF-like tumors, particularly after heterotypic spheroid engraftment, as defined by an expert NF1 pathologist.

NF1(−/−) homotypic spheroids (Figure 4A) grew attached to the gastrocnemius muscle as small masses or inside it as

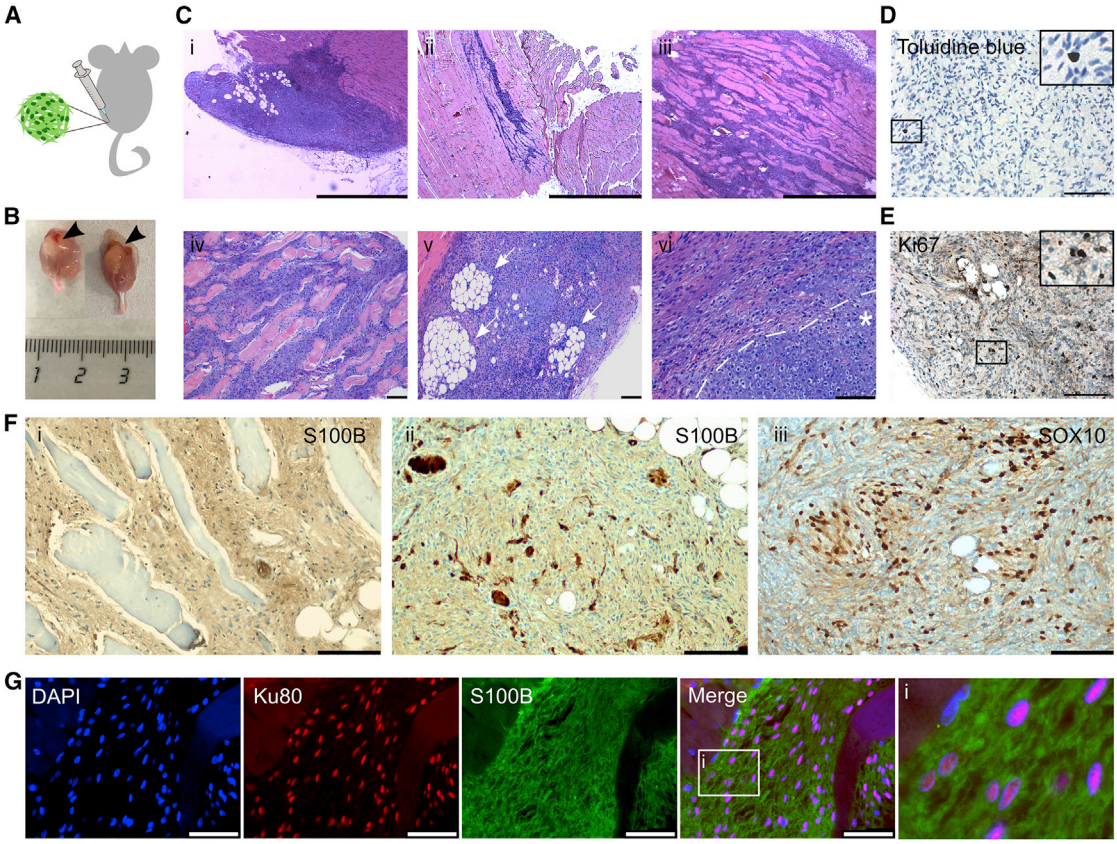

Figure 4. *NF1*(−/−) homotypic spheroids generate small and infiltrative NF-like tumors *in vivo*

(A) Homotypic spheroids were engrafted in the left leg of nude mice. N = 3 mice per group: *NF1*(+/+) and 3 *NF1*(−/−) cell lines (NF1_A, NF1_B, and NF1_C).

(B) Representative images showing *NF1*(−/−) homotypic tumors (arrowheads) that grew attached to the gastrocnemius muscle.

(C) H&E-stained *NF1*(−/−) homotypic tumors that grew attached to the gastrocnemius muscle (i) or inside it as infiltrative tumors (ii, iii, iv). Scale bars: 1 cm (i, ii, iii) and 100 μm (iv, v, vi). White arrows show areas of fat (v). Asterisk shows an area of chondrocyte differentiation (vi).

(D) Toluidine blue staining. Scale bar: 100 μm.

(E) Ki67 expression. Scale bar: 100 μm.

(F) S100B (i and ii) and SOX10 (iii) expression in paraffin sections of *NF1*(−/−) homotypic tumors. Diffuse (i) and focal (ii) $S100B^+$ and $SOX10^+$ patterns (iii). Scale bars: 100 μm.

(G) Ku80 and S100B expression in paraffin sections of *NF1*(−/−) homotypic tumors. Ku80 stains human nuclear cells. DAPI was used to stain cell nuclei. Scale bar: 50 μm, except in enlarged view (i).

See also Tables S1 and S2.

infiltrative tumors (Figures 4B and 4Ci–iv). All except 1 (5 from 6 tumors, out of 17 injections) contained areas with NF-like features, including immature SCs, different cellular densities, presence of myxoid areas (Figure 4C; Table S2), presence of mast cells (Figure 4D), and some positivity for Ki67 (Figure 4E). Immunohistochemistry analysis showed that most of these tumors contained areas of S100B staining with diffuse or focal expression patterns and were also positive for SOX10 (Figure 4F). Moreover, tumor cells were positive for the human-specific antibody Ku80, confirming that they originated from the implanted *NF1*(−/−) homotypic spheroids (Figure 4G). Many $Ku80^+$ cells also expressed the S100B marker. Although most of the homotypic tumors contained NF-like areas, we also observed the formation of cartilage and fat in some of them (Figures 4Cv and vi), indicating that some of the engrafted cells did not undergo an SC commitment upon engraftment.

NF1(−/−) heterotypic spheroids (Figure 5A) generated large tumors that grew either attached to the gastrocnemius muscle or inside it, or as large independent tumor masses adjacent to this muscle (Figures 5B and 5C). All but 1 (7 of 8 tumors grown after 17 injections) recapitulated histological features of mature human pNFs, including SCs with a spindle shape and wavy nuclei, different cellular densities (Figure 5Di), collagen deposition (Figure 5Dii), mast cell infiltration (Figures 5Diii and 5F), some positivity for Ki67 (Figure 5G), and the presence of Meissner-like corpuscles (encapsulated nerve ending structures commonly present in NFs), denoting a clear SC maturation (Figure 5Div). Some of them also contained areas resembling NFs with epithelioid cell change (Figure 5Dii; Table S2). Immunohistochemistry analysis confirmed that all heterotypic tumors contained large areas of $S100B^+$ and $SOX10^+$ cells (Figures 5E and 5H). S100B staining was mainly diffuse and more intense in

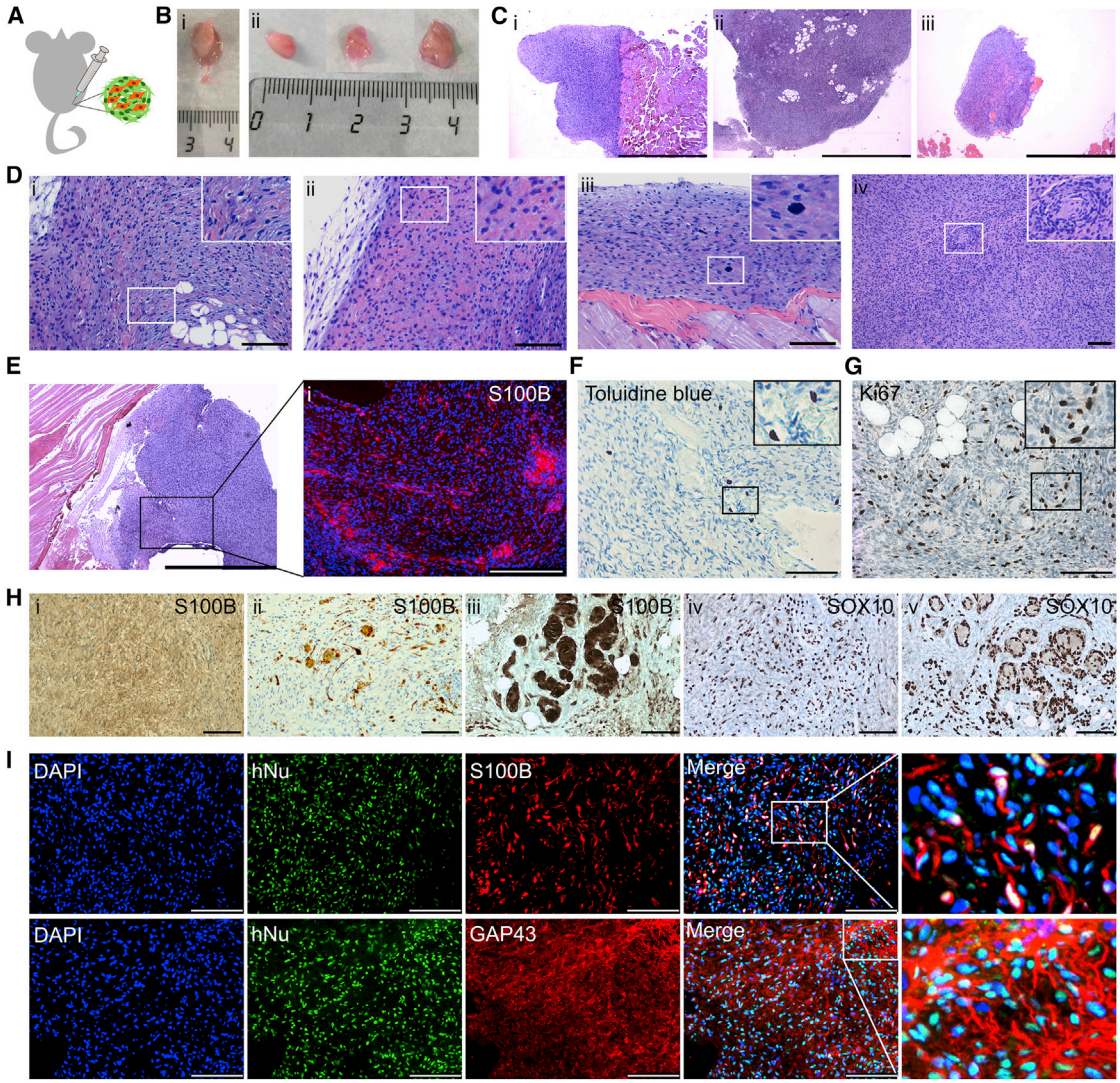

Figure 5. *NF1*(−/−) heterotypic spheroids generate large and compact NF-like tumors *in vivo*

(A) Heterotypic spheroids were engrafted in the right legs of nude mice. N = 3 mice per group: *NF1*(+/+), and 3 *NF1*(−/−) cell lines (NF1_A, NF1_B, and NF1_C).

(B) Representative images showing *NF1*(−/−) heterotypic tumors that grew attached to the gastrocnemius muscle (i) or as independent masses next to it (ii).

(C) H&E-stained *NF1*(−/−) heterotypic tumors grown attached to the gastrocnemius muscle (i) or as independent tumor masses (ii and iii). Scale bars: 1 cm.

(D) H&E-stained tumors showing NF-like features: NF-like SCs (i), collagen (ii), infiltrative mast cell (iii), and Meissner-like corpuscles (iv). Scale bar: 100 μm, except in enlarged view.

(E) H&E-stained tumors and S100B expression in paraffin sections of 1 *NF1*(−/−) heterotypic tumor containing Meissner-like corpuscles. DAPI was used to stain cell nuclei. Scale bars: 1 cm (H&E), 250 μm (i).

(F) Toluidine blue staining. Scale bar: 100 μm.

(G) Ki67 expression. Scale bar: 100 μm.

(H) S100B (i, ii, and iii) and SOX10 (iv and v) expression in paraffin sections of *NF1*(−/−) heterotypic tumors. Diffuse (i) and focal (ii and iii) $S100B^+$ and $SOX10^+$ (iv and v) patterns. Scale bars: 100 μm.

(I) hNu, S100B, and GAP43 expression in OCT sections of *NF1*(−/−) heterotypic tumors. hNu stains human nuclear cells. Insets show co-localization of hNu and S100B or GAP43. DAPI was used to stain cell nuclei. Scale bars: 100 μm, except in enlarged view.

See also Tables S1 and S2.

Meissner corpuscles, highlighting their architecture (Figures 5E and 5H). Tumor cells were positive for the human-specific antibody hNu, which colocalized in cells expressing S100B and GAP43 markers, confirming the human SC identity of the grown NFs (Figure 5I). Since heterotypic spheroids contained two of the main NF cell types and exhibited a high capacity to form NF-like tumors *in vivo*, we called them neurofibromaspheres.

All together, these results showed that homotypic spheroids were capable of generating NF-like tumors, although small, infiltrative, and with few collagen depositions. Remarkably,

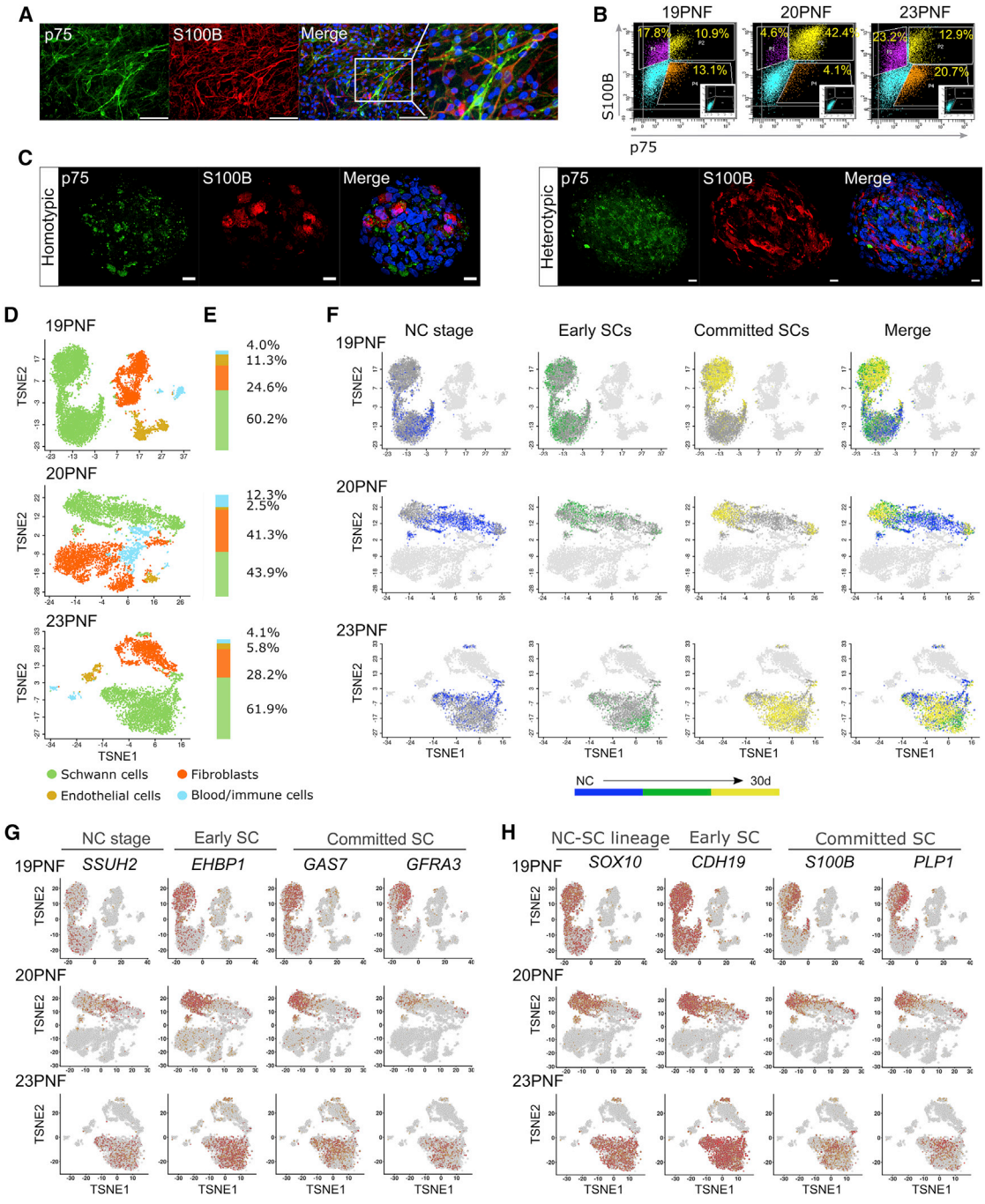

Figure 6. SC component of pNFs is heterogeneous, containing cells at different maturation stages along the NC-SC axis

(A) p75 and S100B expression in human pNF-derived SCs, showing heterogeneity in cell culture. DAPI was used to stain cell nuclei. Scale bars: 50 μm, except in enlarged view.

(B) Flow cytometry analysis for p75 and S100B expression of cells dissociated from 3 independent human pNFs (19PNF, 20PNF, and 23PNF). The percentage of the different populations (inside each graph) and control non-stained cells for each tumor (insets) are shown. See also Figure S7.

(C) Representative confocal micrographs of homotypic (left) and heterotypic (right) spheroids stained with p75 and S100B, showing heterogeneity. Scale bar: 20 μm.

(D) scRNA-seq t-SNE plots of 3 human pNFs from NF1 patients in (B) showing the 4 main cell components: SCs, fibroblasts, endothelial cells, and blood/immune cells. 5,087, 6,155, and 9,092 single cells were analyzed for each pNF, respectively.

(E) Stacked bar charts showing the proportions of each cell type component for each pNF analyzed by scRNA-seq analysis. The percentage of each component is shown.

(legend continued on next page)

neurofibromaspheres were capable of generating large tumors, exhibiting most of the histological features of NFs. These results highlight the importance of the *NF1*(+/−) Fbs environment. Nonetheless, we still detected a few areas of cartilage and fat in some of the tumors generated (Figure S6).

Unexpectedly, one of the three *NF1*(−/−) cell lines, NF1_A, was not able to form tumors from heterotypic spheroids. In contrast, some of the homotypic spheroids of this cell line did indeed form tumors and even NF-like tumors, possibly pointing to an adverse effect of the specific Fb culture used to generate NF1_A neurofibromaspheres. Thus, considering only cell lines NF1_B and NF1_C, neurofibromasphere engraftment generated NFs in 63.3% of cases (Table S1). These two cell lines were the ones that exhibited an NC-SC expression roadmap profile similar to *NF1*(+/+)-differentiating SCs at 30 days, heterotypic WT spheroids, and pNF-derived primary SC cultures (Figure 3E). Again, the cell identity provided by the expression signatures of neurofibromaspheres greatly coincided with the identity of the cell types that engrafted and expanded *in vivo*.

The SC component of pNFs is heterogeneous, containing cells at different maturation stages within the NC-SC axis

The generation of an *in vitro* NC-SC expression roadmap provided an opportunity to analyze the SC component of pNFs according to the new stage-specific lineage markers. pNF-derived SC cultures exhibited an NC-SC expression roadmap signature similar to the one of differentiating *NF1*(+/+) SCs at 30 days (Figures 3E and 3F). However, despite this similarity, pNF-derived SC cultures also expressed genes present at earlier NC-SC stages (Data S4; Carrió et al., 2019). We wondered whether the expression of NC-SC markers was homogeneous throughout the entire SC culture population or whether SC cultures were composed of a heterogeneous population of cells differentially expressing NC-SC markers. Thus, we selected two markers, one expressed along the NC-SC differentiation axis (p75/NGFR), and one expressed upon SC commitment (S100B). p75 and S100B co-staining of pNF-derived SC cultures revealed heterogeneity in the expression of these two markers in all of the SC cultures analyzed (Figure 6A). We then analyzed the p75/S100B co-expression directly in pNF-dissociated cells from 5 independent human pNFs by flow cytometry (Figures 6B and S7). This analysis revealed that within the pNF SC component, three types of cell populations coexist according to p75/S100B expression—a main population of double-positive cells and two minor populations preferentially expressing one of the markers. This analysis also showed inter-pNF variation on the percentages of these different subpopulations. For instance, the $p75^{+}$ $S100B^{-}$ cell population ranged from 5% to 23% among the different pNFs. We reasoned that these three SC subpopulations probably represented cells within the NC-SC lineage at distinct differentiation or maturation states. At this point, we analyzed whether this *NF1*(−/−) SC heterogeneity also existed in the developed homotypic and heterotypic spheroid models. We performed the same p75 and S100B co-staining in spheroids. Confocal images showed that both homotypic and heterotypic *NF1*(−/−) spheroids also contained cells differentially expressing these two markers (Figure 6C), similar to patient pNFs, and thus, also presented heterogeneity within the SC component.

To further characterize the heterogeneity of the pNF SCs, we performed single-cell RNA-seq analysis (scRNA-seq) of the same 3 independent pNFs (19PNF, 20PNF, 23PNF) shown in Figure 6B, using 10X Genomics technology. We analyzed the expression of >2,000 genes in 5,087, 6,155 and 9,092 single cells, respectively. scRNA-seq analysis identified clusters of cells representing different cell types composing pNFs. We assigned these clusters into 4 main components: SCs, Fbs, endothelial cells, and blood/immune cells (Figure 6D; Data S5). In the three pNFs, the two main cell components were SCs and Fbs (Figure 6E), both composed at the same time as different clusters of cells (Data S5).

We analyzed the heterogeneity within the SC component of pNFs regarding the expression of markers along the NC-SC axis. We used genes in the NC-SC *in vitro* expression roadmap signature to analyze genes at the NC stage, at an early differentiating stage (at day 7 of SC differentiation), and at an SC commitment stage (30 days of SC differentiation). We assigned an identity to the cells using a scoring system based on the expression of genes from each stage/time point present in single-cell pNF data (Data S1) and plotted these cell identities in t-distributed stochastic neighbor embedding (t-SNE) plots (Figure 6F). We identified a cell subpopulation with an identity closer to the NC stage, another at an early SC differentiation point, and finally a cell subpopulation with an identity of committed SCs, revealing the existence of a heterogeneous population of cells at different maturation stages of the NC-SC axis within patients pNFs. A merged plot (Figure 6F) revealed the existence of regions of the SC component enriched in cells of distinct identities, showing that the stage along the NC-SC differentiation axis plays a role in defining the structure of the SC component displayed in t-SNE plots. To further clarify this heterogeneity, we selected individual genes differentially expressed along the roadmap (Figure 6G; Data S5), as well as classic NC-SC markers (Jessen and Mirsky, 2005) (Figure 6H). Many individual roadmap genes fairly reproduced the global stage-specific expression patterns, with slight differences. We also plotted the expression of classic markers preferentially expressed in SCPs or induced before SC commitment (*SOX10*, *CDH19*) and others strongly induced upon SC commitment (*S100B*, *PLP1*) (Figure 6H), reinforcing the existence of subpopulations of SCs within pNFs at different maturation stages. Some markers, such as *CDH19,* were expressed in most of the cells of the SC component, while markers of SC commitment, such as S100B, were restricted to a specific subpopulation.

(F) scRNA-seq t-SNE plots as in (D) showing the expression identity of cells within the SC component of pNFs based on genes of the *in vitro* NC-SC expression roadmap: NC stage (blue), early differentiating SC stage (early SCs, at day 7 of SC differentiation, green), and at SC commitment stage (at day 30 of SC differentiation, yellow). Merge plot shows the existence of distinct SC subpopulations.
(G and H) scRNA-seq t-SNEs plotting the expression of specific roadmap-selected (G) and classic (H) NC-SC markers. See also Data S5.

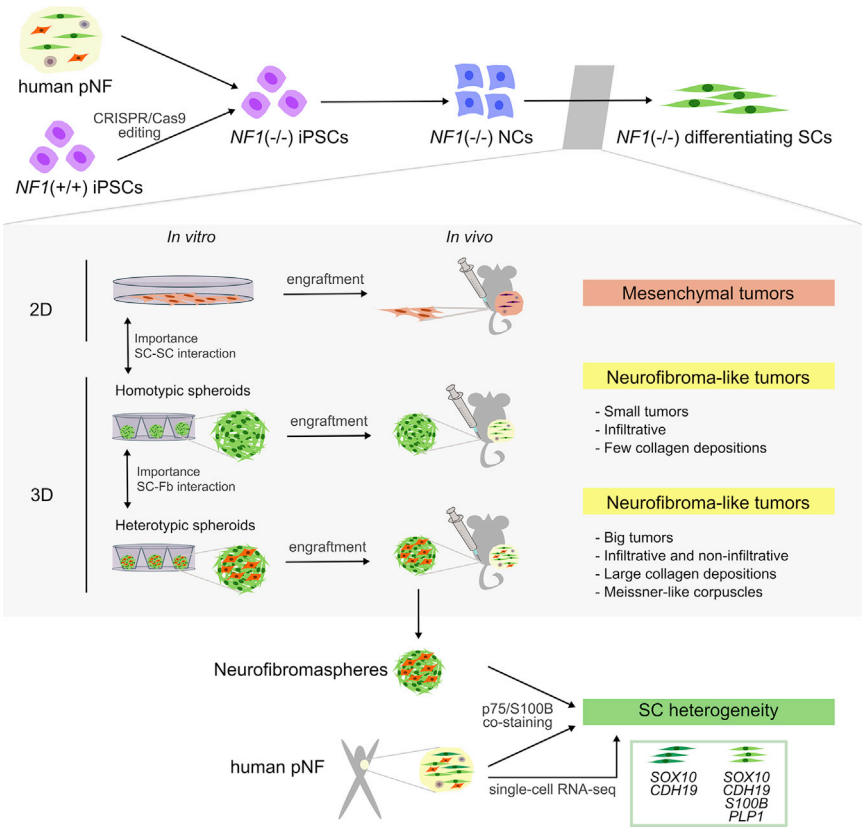

Figure 7. Schematic representation of human *in vitro*/*in vivo* 3D NF model development

NF1(−/−) iPSCs were obtained either by reprogramming pNF-derived cells or by editing the *NF1* gene in control iPSCs using CRISPR-Cas9 technology. *NF1*(−/−) iPSC cells were differentiated toward NC cells and SCs. In 2D, *NF1*(−/−) cells under SC differentiating conditions acquire an NC-mesenchymal cell path and generate mesenchymal tumors *in vivo*. In 3D, *NF1*(−/−) homotypic and heterotypic spheroids were able to generate NF-like tumors after their engraftment in contact with the sciatic nerves of nude mice. The engraftment of neurofibromaspheres, composed of *NF1*(−/−) differentiating SCs and pNF-derived Fbs, represented the most efficient and consistent way of producing human NF-like tumors in mice. The SC component within pNFs is composed of cells differently expressing genes of the NC-SC lineage, denoting different maturation states along this differentiation axis.

DISCUSSION

In this work, we describe the development of an *in vitro* 3D model system for NF, consisting of an admixture of iPSC-derived differentiating *NF1*(−/−) SCs with primary *NF1*(+/−) pNF-derived Fbs. These heterotypic spheroids (neurofibromaspheres) are amenable to multiplex screening, and most importantly, upon engraftment in contact with the sciatic nerves of nude mice consistently generate human NF-like tumors. This development allowed us to compare different cell-based models, being able to characterize their expression profiles and gaining understanding of different aspects of NF formation, such as the importance of SC-SC and SC-Fb interactions, and the resulting cell heterogeneity of the SC linage within NFs.

The *in vivo* modeling of pNFs has been successfully accomplished with the use of GEMMs (reviewed in Buchstaller et al., 2012a,; Li et al., 2019). However, in the literature, only a few attempts have been made to generate NF patient-derived xenograft (PDX) models directly from human tumors (Gleiss et al., 2013; Lee et al., 1992), probably due to their low growth rate after engraftment. Margaret Wallace's and David Muir's labs engrafted human *NF1*(−/−) primary SCs or immortalized SCs into nude mice (Li et al., 2010, 2016; Perrin et al., 2007), also exhibiting a slow growth pattern. In this context, we envisioned the possible development of an experimentally amenable human NF model by generating NC-SC lineage cells derived from iPSCs, with the precise identity and in sufficient quantity to engraft and form tumors in mice consistently (Mazuelas et al., 2020). Recently, Mo et al. (2020) also used *NF1*(−/−) iPSCs to differentiate them toward the SC lineage and engrafted them into the sciatic nerves of nude mice to model NFs. Their results confirmed that the loss of *NF1* alters both the proliferation and differentiation capacity of cells differentiating toward SCs, as previously described (Carrió et al., 2019). In fact, the generation, in the present work, of a new *NF1*(−/−) iPSC line by editing a control *NF1*(+/+) iPSC line, and its functional comparison with *NF1*(−/−) iPSCs generated directly from pNF cells, definitely confirms that the observed proliferation and differentiation alterations in differentiating SCs can be attributed to the absence of *NF1*.

Remarkably, in contrast to differentiating SCs, NC cells lacking the *NF1* gene exhibited an expression signature closely resembling control *NF1*(+/+) cells (Figure 2B), consistent with their previously described identical potency and migration capabilities (Carrió et al., 2019). Furthermore, *NF1*(−/−) NC cells were unable to form NF-like tumors upon engraftment in contact with the sciatic nerve (Figure 2E), confirming results from Joseph et al. (2008) in which the ablation of *NF1* in NC cells did not form pNFs in GEMM.

The comparison of the 2D and 3D model systems developed (Figure 7) provided valuable information about the key role of SC-SC and SC-Fb interactions for NF development. The development of NFs from homotypic spheroids but not from 2D cultures, where cells mostly end up adopting a mesenchymal phenotype, stresses the importance of SC-SC signaling provided by their close physical interaction for the maintenance of axis commitment. At the same time, the generation of NFs from neurofibromaspheres was the most robust and efficient way. Grown NFs were large and faithfully recapitulated NF histological characteristics (e.g., collagen deposition, formation of

Meissner-like corpuscles). This result highlights the importance of pNF-derived Fbs in NF formation, probably by providing collagen deposition, trophic factors, and a niche effect, confirming once more the importance of the microenvironment in facilitating NF formation (Brosseau et al., 2018; Staser et al., 2012; Yang et al., 2008). One of the iPSC lines (NF1_A) generated heterotypic spheroids that did not produce NFs upon engraftment, nor any other tumor, while homotypic counterparts generated NFs. The physiological state of the specific primary Fb cell culture used for these heterotypic spheres could provide an explanation for this result. Primary Fb cultures used for the generation of NF1_A neurofibromaspheres were from cultures that underwent many passages, probably aging and exhausting the culture, which may have resulted in the loss of trophic and niche capacity. In this regard, it would be interesting to investigate whether the type of Fbs used for generating spheroids and their physiological status or the presence of other cell types (e.g., immune cells) has any influence on the formation of NFs *in vivo*.

RNA-seq profiles of the different *in vitro* models developed strongly coincided with the type of tumor generated *in vivo*, highlighting their predictive value. The characterization of the *in vitro* NC-SC lineage by RNA-seq using control *NF1*(+/+) cells allowed the generation of a genuine expression roadmap of the *in vitro* NC-SC differentiation lineage. The expression roadmap guided us in this analysis and facilitated the identification of new lineage markers that may be useful for the characterization of cell identity at different stages along the NC-SC axis (Data S1). In the last decades, there has been a long-standing effort to characterize the development of the SC lineage (Jessen and Mirsky, 2005; Woodhoo and Sommer, 2008; Monk et al., 2015; Kastriti and Adameyko, 2017), looking for the physiological capabilities of the different cell stages and their specific markers. Many of the markers captured by the roadmap are also expressed in pNF-derived SC cultures and are present in the SC component of scRNA-seq data, supporting their potential validity as lineage markers (Data S1).

pNFs originate during development, and collectively GEMM models point to an SCP derived from the boundary cap (Radomska and Topilko, 2017) as the most probable cell type originating pNFs (Radomska et al., 2019). However, the exact identity and potency of these cells within the NC-SC axis remain poorly characterized. We lack specific markers for identifying and isolating these cells, since many NC-SC markers are expressed throughout differentiation axis (e.g., *SOX10*, *NGFR*) or are common to distinct stages (Jessen and Mirsky, 2019). In this regard, markers of the *in vitro* NC-SC expression roadmap (e.g., *SSUH2*, *EHBP1*, *GAS7*; Data S1) expressed in pNFs and neurofibromaspheres could facilitate this identification. NF-forming neurofibromaspheres (NF1_B and NF1_C) displayed an expression roadmap similar to *NF1*(+/+) cells at 30 days of SC differentiation in 2D (Figure 3), but they also expressed roadmap genes at earlier time points (NC, 7 and 14 days) (Data S4) that may facilitate the identification of markers of NF-originating cells. However, the SC heterogeneity identified within neurofibromaspheres and pNFs complicates this analysis from bulk RNA expression.

pNFs and neurofibromaspheres contain cells differentially expressing early-stage SC and SC committed markers (e.g., p75, S100B). scRNA-seq analysis of pNFs confirmed the SC component heterogeneity (Figure 6F). We observed that some pNF cells better captured the expression of genes at the NC stage, while others captured the expression of early SC differentiation genes, and a highly homogeneous subpopulation expressed SC commitment genes, although most are probably still immature SCs. This SC heterogeneity may reflect a continuous cell differentiation process of the SC lineage within human pNFs, with less differentiated cells giving rise to cells advancing in the maturation process. The fact that many cells seem to express markers along the whole NC-SC axis (*SOX10*, *CDH19*, *PLP1*, *S100B*) makes the characterization of their identity even more challenging. A functional characterization separating subpopulations of the SC component of pNFs and neurofibromaspheres may help clarify the identity of the cells originating pNFs, their impact on tumor composition, and potential differential treatment responses (Rybinski and Yun, 2016).

In summary, we presented here the successful generation of an *in vitro/in vivo* model for human NFs. To do so, we compared the suitability of 2D and 3D models, gaining understanding of the importance of SC-SC interaction and the presence of Fbs to faithfully model this tumor type. The generation of an expression roadmap of the NC-SC *in vitro* differentiation process using *NF1*(+/+) cells guided the monitoring of differentiating *NF1*(−/−) SC systems and allowed the identification of new potential state-specific NC-SC lineage markers. In addition, RNA-seq analysis of NF-forming heterotypic spheroids allowed a better characterization of the expression identity of cells able to form an NF. Finally, we uncovered the heterogeneity of the pNF SC component, also present in neurofibromaspheres. We identified distinct cell subpopulations expressing genes that characterize different maturation stages along the NC-SC differentiation axis. This work draws a picture in which NF development results from a balance between a high cellular proliferation capacity, provided by the loss of *NF1*, and a commitment to the NC-SC lineage, provided by cellular-cellular interactions and the presence of Fbs. This results in tumors with a heterogeneous SC component that is composed of cells at different maturation states along the NC-SC axis.

Limitations of the study

Neurofibromaspheres constitute a successful *in vitro/in vivo* model for NFs. However, a better standardization will require the quantification of cells and sizes of neurofibromaspheres generated, as well as a better understanding of the role of different types of Fbs and their physiological status (or conceivable substitutes such as Matrigel). In addition, the identification of new potential state-specific lineage markers through the analysis of the NC-SC *in vitro* differentiation expression roadmap will require the use of additional *in vivo* and *in vitro* systems for their validation. Finally, despite our experience in NF dissociation and SC culture procedures, and despite the high concordance between the proportions of pNF cell components identified by single-cell analysis and by previous pNF histological characterizations, the single-cell data generated could be somehow biased by sample preparation and by limitations in the current knowledge of the assignment of identities to peripheral nerve cells from expression data.

STAR★METHODS

Detailed methods are provided in the online version of this paper and include the following:

- KEY RESOURCES TABLE
- RESOURCE AVAILABILITY
  - Lead contact
  - Materials availability
  - Data and code availability
- EXPERIMENTAL MODEL AND SUBJECT DETAILS
  - Patients, plexiform neurofibromas (pNFs), and tumor processing
  - pNF-derived Schwann cells (SCs) and fibroblast cultures
  - Human iPS cell culture
  - iPSC lines and CRISPR/Cas9 gene edition
  - Animal models
- METHOD DETAILS
  - Differentiations toward neural crest (NC) and Schwann cells (SCs) in 2D
  - Differentiation towards SC in 3D: spheroid generation
  - RNA extraction and RT-qPCR analysis
  - RNA-seq and analysis
  - Single-cell RNA-Seq and analysis
  - Western Blot
  - Flow cytometry of pNFs
  - Engraftment experiments
  - Immunocytochemical analysis
  - Confocal microscopy
  - Immunohistochemical analysis of paraffin samples
  - Fluorescent immunohistochemistry of paraffin samples
  - Fluorescent immunohistochemistry of OCT samples
- QUANTIFICATION AND STATISTICAL ANALYSIS

SUPPLEMENTAL INFORMATION

Supplemental information can be found online at https://doi.org/10.1016/j.celrep.2022.110385.

ACKNOWLEDGMENTS

We thank Erica Hurtado and Mónica Suelves for technical advice and assistance in mice tumor dissection. We thank the IGTP core facilities and their staff for their contribution and technical support: Translational Genomics Core Facility; High Content Genomics and Bioinformatics Core Facility; Flow Cytometry (Gerard Requena and Marco A. Fernández); IGTP-Hospital Universitari Germans Trias i Pujol (HUGTP) Biobank Facility (Laia Pérez-Roca and Christel Kisser Pioch) and Pathology Department (Dr. Pedro Luis González); and the Barcelona Stem Cell Bank, Regenerative Medicine Program, IDIBELL, Barcelona, for iPSC characterization. We are also grateful to the Fundación Proyecto Neurofibromatosis, the Asociación de Afectados de Neurofibromatosis (AANF), and the Catalan Neurofibromatosis Association (ACNefi) for their constant support. This work has mainly been supported by an agreement from the Johns Hopkins University School of Medicine and the Neurofibromatosis Therapeutic Acceleration Program (NTAP). Its contents are solely the responsibility of the authors and do not necessarily represent the official views of the Johns Hopkins University School of Medicine. The work has also been partially supported by the Spanish Ministry of Science and Innovation, Carlos III Health Institute (ISCIII) (PI17/00524; PI20/00228) Plan Estatal de I + D + I 2013–2016, co-financed by the FEDER program – a way to build Europe, the Fundación PROYECTO NEUROFIBROMATOSIS, and by the Government of Catalonia (2017-SGR-496) and CERCA Program/Generalitat de Catalunya. M.M.-L. is supported by Fundación PROYECTO NEUROFIBROMATOSIS.

AUTHOR CONTRIBUTIONS

Conceptualization, E.S., M.C., and B.G.; methodology, H.M. and M.C.; software and formal analysis, M.M.-L. and B.G.; investigation, H.M., J.F.-R., I.U.-A., Y.R.-P., E.T., J.C., C.R., and M.C.; resources, C.L., H.H., A.R., I.B., E.C., and A.V.; writing – original draft, H.M., M.C., and E.S.; writing – review & editing, M.M.-L., B.G., E.C., H.M., M.C., and E.S.; visualization, H.M., M.M.-L., B.G., M.C., and E.S.; supervision, B.G., M.C., and E.S.; project administration, M.C. and E.S.; funding acquisition, E.S.

DECLARATION OF INTERESTS

The authors declare no competing interests.

Received: July 5, 2021
Revised: November 4, 2021
Accepted: January 24, 2022
Published: February 15, 2022

REFERENCES

Akshintala, S., Baldwin, A., Liewehr, D.J., Goodwin, A., Blakeley, J.O., Gross, A.M., Steinberg, S.M., Dombi, E., and Widemann, B.C. (2020). Longitudinal evaluation of peripheral nerve sheath tumors in neurofibromatosis type 1: growth analysis of plexiform neurofibromas and distinct nodular lesions. Neuro. Oncol. *22*, 1368–1378.

Aran, D., Looney, A.P., Liu, L., Wu, E., Fong, V., Hsu, A., Chak, S., Naikawadi, R.P., Wolters, P.J., Abate, A.R., et al. (2019). Reference-based analysis of lung single-cell sequencing reveals a transitional profibrotic macrophage. Nat. Immunol. *20*, 163–172.

Brosseau, J.P., Liao, C.P., Wang, Y., Ramani, V., Vandergriff, T., Lee, M., Patel, A., Ariizumi, K., and Le, L.Q. (2018). NF1 heterozygosity fosters de novo tumorigenesis but impairs malignant transformation. Nat. Commun. *9*, 1–11.

Buchstaller, J., Clapp, D.W., Parada, L.F., and Zhu, Y. (2012). Neurofibromatosis type 1: molecular and cellular biology. In Cell of Origin and the Contribution of Microenvironment in NF1 Tumorigenesis and Therapeutic Implications, M. Upadhyaya and D.N. Cooper, eds. (Springer), pp. 549–568.

Buchstaller, J., McKeever, P.E., and Morrison, S.J. (2012a). Tumorigenic cells are common in mouse MPNSTs but their frequency depends upon tumor genotype and assay conditions. Cancer Cell *21*, 240–252.

Carrió, M., Mazuelas, H., Richaud-Patin, Y., Gel, B., Terribas, E., Rosas, I., Jimenez-Delgado, S., Biayna, J., Vendredy, L., Blanco, I., et al. (2019). Reprogramming captures the genetic and tumorigenic properties of neurofibromatosis type 1 plexiform neurofibromas. Stem Cell Rep. *12*, 1–16.

Castellsagué, J., Gel, B., Fernández-Rodríguez, J., Llatjós, R., Blanco, I., Benavente, Y., Pérez-Sidelnikova, D., García-del Muro, J., Viñals, J.M., Vidal, A., et al. (2015). Comprehensive establishment and characterization of orthoxenograft mouse models of malignant peripheral nerve sheath tumors for personalized medicine. EMBO Mol. Med. *7*, 608–627.

Chen, Z., Liu, C., Patel, A.J., Liao, C.P., Wang, Y., and Le, L.Q. (2014). Cells of origin in the embryonic nerve roots for NF1-associated plexiform neurofibroma. Cancer Cell *26*, 695–706.

Chen, Z., Mo, J., Brosseau, J.P., Shipman, T., Wang, Y., Liao, C.P., Cooper, J.M., Allaway, R.J., Gosline, S.J.C., Guinney, J., et al. (2019). Spatiotemporal loss of NF1 in schwann cell lineage leads to different types of cutaneous neurofibroma susceptible to modification by the hippo pathway. Cancer Discov. *9*, 114–129.

DeBella, K., Szudek, J., and Friedman, J.M. (2000). Use of the National Institutes of Health criteria for diagnosis of neurofibromatosis 1 in children. Pediatrics *105*, 608–614.

Dombi, E., Solomon, J., Gillespie, A.J., Fox, E., Balis, F.M., Patronas, N., Korf, B.R., Babovic-Vuksanovic, D., Packer, R.J., Belasco, J., et al. (2007). NF1 plexiform neurofibroma growth rate by volumetric MRI: relationship to age and body weight. Neurology *68*, 643–647.

Dombi, E., Baldwin, A., Marcus, L.J., Fisher, M.J., Weiss, B., Kim, A., Whitcomb, P., Martin, S., Aschbacher-Smith, L.E., Rizvi, T.A., et al. (2016). Activity of selumetinib in neurofibromatosis type 1-related plexiform neurofibromas. N. Engl. J. Med. *375*, 2550–2560.

Ducatman, B.S., Scheithauer, B.S., Piepgras, D.G., Reiman, H.M., and Ilstrup, D.M. (1986). Malignant peripheral nerve sheath tumors. A clinicopathologic study of 120 cases. Cancer *57*, 2006–2021.

Fernández-Rodríguez, J., Morales La Madrid, A., Gel, B., Castañeda Heredia, A., Salvador, H., Martínez-Iniesta, M., Moutinho, C., Morata, J., Heyn, H., Blanco, I., et al. (2020). Use of patient derived orthotopic xenograft models for real-time therapy guidance in a pediatric sporadic malignant peripheral nerve sheath tumor. Ther. Adv. Med. Oncol. *12*, 1–11.

Ferner, R.E., Huson, S.M., Thomas, N., Moss, C., Willshaw, H., Evans, D.G., Upadhyaya, M., Towers, R., Gleeson, M., Steiger, C., et al. (2007). Guidelines for the diagnosis and management of individuals with neurofibromatosis. J. Med. Genet. *44*, 81–88.

Galili, T. (2015). dendextend: an R package for visualizing, adjusting and comparing trees of hierarchical clustering. Bioinformatics *31*, 3718–3720.

Gleiss, J., Demestre, M., Spyra, M., Eschenhagen, T., Hagel, C., Mautner, V.F., Kluwe, L., and Friedrich, R.E. (2013). B-scan ultrasonographic monitoring of orthotopic xenografted plexiform neurofibroma in mice. In Vivo. *27*, 723–727.

Griffiths, J.A., Richard, A.C., Bach, K., Lun, A.T.L., and Marioni, J.C. (2018). Detection and removal of barcode swapping in single-cell RNA-seq data. Nat. Commun. *9*, 1–6.

Gross, A.M., Wolters, P.L., Dombi, E., Baldwin, A., Whitcomb, P., Fisher, M.J., Weiss, B., Kim, A., Bornhorst, M., Shah, A.C., et al. (2020). Selumetinib in children with inoperable plexiform neurofibromas. N. Engl. J. Med. *383*, 1290, NEJMoa1912735.

Jessen, K.R., and Mirsky, R. (2005). The origin and development of glial cells in peripheral nerves. Nat. Rev. Neurosci. *6*, 671–682.

Jessen, K.R., and Mirsky, R. (2019). Schwann cell precursors; multipotent glial cells in embryonic nerves. Front. Mol. Neurosci. *12*, 1–16.

Joseph, N.M., Mosher, J.T., Buchstaller, J., Snider, P., McKeever, P.E., Lim, M., Conway, S.J., Parada, L.F., Zhu, Y., and Morrison, S.J. (2008). The loss of Nf1 transiently promotes self-renewal but not tumorigenesis by neural crest stem cells. Cancer Cell *13*, 129–140.

Kastriti, M.E., and Adameyko, I. (2017). Specification, plasticity and evolutionary origin of peripheral glial cells. Curr. Opin. Neurobiol. *47*, 196–202.

Krone, W., Jirikowski, G., Mühleck, O., Kling, H., and Gall, H. (1983). Cell culture studies on neurofibromatosis (von Recklinghausen). II. Occurrence of glial cells in primary cultures of peripheral neurofibromas. Hum. Genet. *63*, 247–251.

Lee, J.K., Sobel, R.A., Chiocca, E.A., Kim, T.S., and Martuza, R.L. (1992). Growth of human acoustic neuromas, neurofibromas and schwannomas in the subrenal capsule and sciatic nerve of the nude mouse. J. Neurooncol. *14*, 101–112.

Li, H., Zhang, X., Fishbein, L., Kweh, F., Thompson, M.C., Perrin, G.Q., Muir, D., and Wallace, M. (2010). Analysis of steroid hormone effects on xenografted human NF1 tumor Schwann cells. Cancer Biol. Ther. *10*, 758–764.

Li, H., Chang, L.J., Neubauer, D.R., Muir, D.F., and Wallace, M.R. (2016). Immortalization of human normal and NF1 neurofibroma Schwann cells. Lab. Investig. *96*, 1105–1115.

Li, S., Chen, Z., and Le, L.Q. (2019). New insights into the neurofibroma tumor cells of origin. Neurooncol. Adv. *2*, i13–i22.

Love, M.I., Huber, W., and Anders, S. (2014). Moderated estimation of fold change and dispersion for RNA-seq data with DESeq2. Genome Biol. *15*, 1–21.

Mabbott, N.A., Baillie, J.K., Brown, H., Freeman, T.C., and Hume, D.A. (2013). An expression atlas of human primary cells: inference of gene function from coexpression networks. BMC Genomics *14*, 632.

Mazuelas, H., Carrió, M., and Serra, E. (2020). Modeling tumors of the peripheral nervous system associated with Neurofibromatosis type 1: reprogramming plexiform neurofibroma cells. Stem Cell Res. *49*, 102068.

McCarron, K.F., and Goldblum, J.R. (1998). Plexiform neurofibroma with and without associated malignant peripheral nerve sheath tumor: a clinicopathologic and immunohistochemical analysis of 54 cases. Mod. Pathol. *11*, 612–617.

McCarthy, D.J., Campbell, K.R., Lun, A.T.L., and Wills, Q.F. (2017). Scater: pre-processing, quality control, normalization and visualization of single-cell RNA-seq data in R. Bioinformatics *33*, 1179–1186.

Menendez, L., Kulik, M.J., Page, A.T., Park, S.S., Lauderdale, J.D., Cunningham, M.L., and Dalton, S. (2013). Directed differentiation of human pluripotent cells to neural crest stem cells. Nat. Protoc. *8*, 203–212.

Messiaen, L.M. (2020). Molecular diagnosis for NF1. In Multidisciplinary Approach to Neurofibromatosis Type 1, G. Tadini, E. Legius, and H. Brems, eds. (Springer), pp. 15–34.

Mo, J., Anastasaki, C., Chen, Z., Shipman, T., Papke, J.B., Yin, K.Y., Gutmann, D.H., and Le, L.Q. (2020). Humanized neurofibroma model from induced pluripotent stem cells delineates tumor pathogenesis and developmental origins. J. Clin. Invest. *131*, e139807.

Monk, K.R., Feltri, M.L., and Taveggia, C. (2015). New insights on schwann cell development. Glia *63*, 1376–1393.

Patro, R., Duggal, G., Love, M.I., Irizarry, R.A., and Kingsford, C. (2017). Salmon provides fast and bias-aware quantification of transcript expression. Nat. Methods *14*, 417–419.

Peltonen, J., Penttinen, R., Larjava, H., and Aho, H. (1986). Collagens in neurofibromas and neurofibroma cell cultures. Ann. N. Y. Acad. Sci. *486*, 260–270.

Perrin, G., Fishbein, L., Thomson, S.A., Thomas, S.T., Stephens, K., Garbern, J.Y., DeVries, G.H., Yachnis, A.T., Wallace, M.R., and Muir, D. (2007). Plexiform-like neurofibromas develop in the mouse by intraneural xenograft of an NF1 tumor-derived schwann cell line. J. Neurosci. Res. *85*, 1347–1357.

Prada, C.E., Rangwala, F.A., Martin, L.J., Lovell, A.M., Saal, H.M., Schorry, E.K., and Hopkin, R.J. (2012). Pediatric plexiform neurofibromas: impact on morbidity and mortality in neurofibromatosis type 1. J. Pediatr. *160*, 461–467.

Radomska, K.J., and Topilko, P. (2017). Boundary cap cells in development and disease. Curr. Opin. Neurol. *47*, 209–215.

Radomska, K.J., Coulpier, F., Gresset, A., Schmitt, A., Debbiche, A., Lemoine, S., Wolkenstein, P., Vallat, J.M., Charnay, P., and Topilko, P. (2019). Cellular origin, tumor progression, and pathogenic mechanisms of cutaneous neurofibromas revealed by mice with Nf1 knockout in boundary cap cells. Cancer Discov. *9*, 130–147.

Riccardi, V.M. (1992). Type 1 neurofibromatosis and the pediatric patient. Curr. Probl. Pediatr. *22*, 66–106.

Rosenbaum, T., Rosenbaum, C., Winner, U., Müller, H.W., Lenard, H.G., and Hanemann, C.O. (2000). Long-term culture and characterization of human neurofibroma-derived Schwann cells. J. Neurosci. Res. *61*, 524–532.

Rybinski, B., and Yun, K. (2016). Addressing intra-tumoral heterogeneity and therapy resistance. Oncotarget *7*, 72322–72342.

Serra, E., Rosenbaum, T., Winner, U., Aledo, R., Ars, E., Estivill, X., Lenard, H.G., and Lázaro, C. (2000). Schwann cells harbor the somatic NF1 mutation in neurofibromas: evidence of two different Schwann cell subpopulations. Hum. Mol. Genet. *9*, 3055–3064.

Soneson, C., Love, M.I., and Robinson, M.D. (2016). Differential analyses for RNA-seq: transcript-level estimates improve gene-level inferences [version 2; referees: 2 approved]. F1000Res. *4*, 1–23.

Staser, K., Yang, F.-C., and Clapp, D.W. (2012). Pathogenesis of plexiform neurofibroma: tumor-stromal/hematopoietic interactions in tumor progression. Annu. Rev. Pathol. Mech. Dis. *7*, 469–495.

Terribas, E., Garcia-Linares, C., Lázaro, C., and Serra, E. (2013). Probe-based quantitative PCR assay for detecting constitutional and somatic deletions in the NF1 gene: application to genetic testing and tumor analysis. Clin. Chem. *59*, 928–937.

Tucker, T., Friedman, J.M., Friedrich, R.E., Wenzel, R., Fünsterer, C., and Mautner, V.F. (2009). Longitudinal study of neurofibromatosis 1 associated plexiform neurofibromas. J. Med. Genet. *46*, 81–85.

Wallace, M.R., Rasmussen, S.A., Lim, I.T., Gray, B.A., Zori, R.T., and Muir, D. (2000). Culture of cytogenetically abnormal Schwann cells from benign and malignant NFI tumors. Genes Chromosom. Cancer *27*, 117–123.

Wegscheid, M.L., Anastasaki, C., and Gutmann, D.H. (2018). Human stem cell modeling in neurofibromatosis type 1 (NF1). Exp. Neurol. *299*, 270–280.

Woodhoo, A., and Sommer, L. (2008). Development of the schwann cell lineage: from the neural crest to the myelinated nerve. Glia *56*, 1481–1490.

Wu, J., Williams, J.P., Rizvi, T.A., Kordich, J.J., Witte, D., Meijer, D., Stemmer-Rachamimov, A.O., Cancelas, J.A., and Ratner, N. (2008). Plexiform and dermal neurofibromas and pigmentation are caused by Nf1 loss in desert hedgehog-expressing cells. Cancer Cell *13*, 105–116.

Yang, F.C., Ingram, D.A., Chen, S., Zhu, Y., Yuan, J., Li, X., Yang, X., Knowles, S., Horn, W., Li, Y., et al. (2008). Nf1-Dependent tumors require a microenvironment containing Nf1+/– and c-kit-Dependent. Bone Marrow Cell *135*, 437–448.

Yu, G., Wang, L.G., Han, Y., and He, Q.Y. (2012). ClusterProfiler: an R package for comparing biological themes among gene clusters. Omi. A. J. Integr. Biol. *16*, 284–287.

Zheng, H., Chang, L., Patel, N., Yang, J., Lowe, L., Burns, D.K., and Zhu, Y. (2008). Induction of abnormal proliferation by nonmyelinating schwann cells triggers neurofibroma formation. Cancer Cell *13*, 117–128.

Zhu, A., Ibrahim, J.G., and Love, M.I. (2018). Heavy-tailed prior distributions for sequence count data: removing the noise and preserving large differences. Bioinformatics *35*, 2084–2092.

Zhu, Y., Ghosh, P., Charnay, P., Burns, D.K., and Parada, L.F. (2002). Neurofibromas in NF1: schwann cell origin and role of tumor environment. Science *296*, 920–922.

Ziegler, L., Grigoryan, S., Yang, I.H., Thakor, N.V., and Goldstein, R.S. (2011). Efficient generation of schwann cells from human embryonic stem cell-derived neurospheres. Stem Cell Rev. Rep. *7*, 394–403.

STAR★METHODS

KEY RESOURCES TABLE

REAGENT or RESOURCE	SOURCE	IDENTIFIER
Antibodies		
Mouse IgG anti-Nerve growth factor (p75) receptor	Abcam	Cat# ab3125 RRID:AB_303531
Rabbit IgG anti-S100B	DAKO	Cat# Z0311 RRID:AB_10013383
Mouse anti-S100B	Abcam	Cat# Ab14849 RRID:AB_301508
Rabbit IgG anti-GAP43	Novus Biologicals	Cat# NB300-143SS RRID:AB_921392
Mouse IgG anti-AP2	Thermo Scientific	Cat# MA1-872 RRID:AB_2199412
Rabbit IgG anti-Sox10	Abcam	Cat# ab108408 RRID:AB_10859341
Mouse IgG anti-HNK1	Sigma	Cat# C6680 RRID:AB_1078474
Rabbit monoclonal Ki67 (clone 30-9)	Ventana Medical Systems	Cat# 790-4286 RRID:AB_2631262
Rabbit IgG anti-Ku80	Cell Signaling Technology	Cat# 2180 RRID:AB_2218736
Mouse IgG antinuclear antigen (hNu)	Novus Biological	Cat# NBP2-34342 RRID:AB_2802648
Rabbit IgG anti-NF1	Bethyl laboratories	Cat# A300-140[a] RRID:AB_2149790
Mouse IgG anti-αTubulin	Sigma	Cat# T 6074 RRID:AB_477582
Goat anti-Mouse IgG (H+L) Alexa fluor 488	ThermoFisher	Cat# A-11001 RRID:AB_2534069
Goat anti-rabbit IgG (H+L) Alexa fluor 568	ThermoFisher	Cat# A-11011 RRID:AB_143157
Goat anti-rabbit IgG (H+L) Alexa fluor 647	ThermoFisher	Cat# A-21246 RRID:AB_2535814
IRDye 680RD anti-rabbit IgG secondary antibody	LI-COR	Cat# 926-68021 RRID:AB_10706309
IRDye 800CW anti-mouse IgG secondary antibody	LI-COR	Cat# 926-32210 RRID:AB_621842
Bacterial and virus strains		
DH5α Competent Cells	Invitrogen	Cat# 18265017
Biological samples		
Plexiform neurofibromas (pNFs)	Hospital Universitario La Paz, Madrid, Spain. Hospital Universitario 12 de octubre, Madrid, Spain. Hospital de Bellvitge, Barcelona, Spain. Hospital de Manises, Valencia, Spain.	This manuscript
pNF-derived Schwann cells	IGTP	This manuscript

(*Continued on next page*)

Continued

REAGENT or RESOURCE	SOURCE	IDENTIFIER
pNF-derived fibroblast cells	IGTP	This manuscript
Chemicals, peptides, and recombinant proteins		
DMEM	Gibco	Cat# 2196035
Ham's F12	Gibco	Cat# 21765029
mTeSR plus	Stemcell Technology	Cat# 100-0276
FBS	Gibco	Cat# 10270106
Goat serum	Gibco	Cat# 16210-064
GlutaMAX	Gibco	Cat# 35050038
Penicillin/Streptomycin	Gibco	Cat# 15140122
Normocin	Invivogen	Cat# ant-nr-1
DMSO	Sigma	Cat# 276855
Collagenase Type 1	Wothington	Cat# LS004196
Neutral Protease (dispase)	Wothington	Cat# LS02104
Poly-L-Lysine	Sigma	Cat# P1524
Laminin	Gibco	Cat# 23017015
3-Isobutyl-1-Methylxanthine sigmaultra (IBMX)	Sigma	Cat# I7018
Recombinant Human Heregulin beta-1	Peprotech	Cat# 100-03
Forskolin	Sigma	Cat# F6886
N-2 supplement	Gibco	Cat# 17502048
Insulin	Sigma	Cat# I5500
Matrigel Growth Factor Reduced	Cultek	Cat# 45354230
Accutase	Merck	Cat# SCR005
Supperscript III reverse transcriptase enzyme	Life Technologies	Cat# 18080093
NaCl	Merck	Cat# 1064045000
Tris	Millipore	Cat# 648310
EDTA	Sigma-Aldrich	Cat# ED2P-500
Igepal CA-630	Sigma-Aldrich	Cat#I8896
DTT	ThermoFisher	Cat# R0861
PMSF	Sigma-Aldrich	Cat#10837091001
Sodium Orthovanadate	Sigma-Aldrich	Cat# S6508
NaF	Sigma-Aldrich	Cat# S1504
Leupeptin	Sigma	Cat# 62070
Aprotinin from bovine lung	Sigma	Cat# A1153
PhosSTOP	Roche	Cat# 4906845001
Beta mercaptoethanol	Sigma	Cat# 63689
Bromophenol blue sodium salt	Sigma	Cat# 114405
SDS	Merck	Cat# 817034
Glycine	Fisher Scientific	Cat# BP3815
Glycerol	Sigma	Cat# G7757
Odissey blocking buffer (TBS)	LI-COR	Cat# 927-50000
BSA	Sigma	Cat# 5470
PBS	Biowest	Cat# L0615-500
Saponin	Millipore	Cat# 558255
Paraformaldehyde	Santa Cruz Animal Health	Cat# sc-281692
Formalin	DIAPATH	Cat# F0048
Triton-X100	Sigma	Cat# X100

(*Continued on next page*)

Continued

REAGENT or RESOURCE	SOURCE	IDENTIFIER
DAPI	Stemcell Technology	Cat# 75004
citric acid	Sigma	Cat# W230633
Vectashield	Vector Laboratories	Cat# H-1000-10
Sucrose	Sigma	Cat# S7903
OCT	VWR International	Cat# 411243
Paraffin	VWR International	Cat# 2079-A
Harrys' Hematoxylin	QCA	Cat# 995883
Eosin	Bio-Optica	Cat# 05-10003E
ArciTect Cas9-eGFP Nuclease	Stemcell Technology	Cat# 76005
ArciTect crRNA	Stemcell Technology	Cat# 76010
ArciTect tracrRNA	Stemcell Technology	Cat# 76016
ArciTect annealing buffer	Stemcell Technology	Cat# 76020
Gateway BP Clonase II Enzyme	Invitrogen	Cat# 11789020
Kanamycin	Merck	Cat# k4000
Critical commercial assays		
Maxwell 16 LEV simply RNA Purification Kit	Promega	Cat# AS1270
Dead Cell Removal MicroBeads kit	Miltenyi Biotec	Cat# 130-090-101
Pierce BCA Protein Assay kit	Thermo Fisher	Cat# 23225
CC1 buffer	Ventana	Cat# 950-124
Ultraview DAB detection system	Ventana	Cat# 760-500
TransIT-X2 transfection reagent	Mirus	Cat# MIR6003
TruSeq Stranded Total RNA Library Prep Gold (48 Samples)	Illumina	Cat# 20020598
Kapa Library Quantification kit for Illumina	Roche	Cat# 7960140001
AmpFlSTR® Identifiler™ PCR Amplification Kit	Applied Biosystems	Cat# 4322288
Deposited data		
RNA-seq and scRNA-seq	This paper	EGA (https://ega-archive.org/), accession number EGA: EGAS00001005907
Code	This paper	https://doi.org/10.5281/zenodo.5808855
Experimental models: Cell lines		
Human: 5PNF_TDiPSsv_MM_4 (alias NF1_A)	IGTP/ Spanish National Stem Cell Bank-Institute of Health Carlos III (BNLC-ISCIII)	Carrió et al., 2019
Human: 3PNF_SiPSsv_MM_11 (alias NF1_B)	IGTP/ Spanish National Stem Cell Bank-Institute of Health Carlos III (BNLC-ISCIII)	Carrió et al., 2019
Human: FiPS Ctrl1-SV4F-7 (alias *NF1*(+/+) FiPS or WT)	Spanish National Stem Cell Bank-Institute of Health Carlos III (BNLC-ISCIII)	This manuscript
Human: *NF1*(-/-) edited FiPS Ctrl1-SV4F-7 (alias NF1_C)	IGTP	This manuscript
Experimental models: Organisms/strains		
Athymic nude mice	Harlan	N/A
Oligonucleotides		
See Table S3. Primer Table	This manuscript	N/A
sgRNA targeting sequence: NF1: GTTGTGCTCAGTACTGACTT	This manuscript	N/A

(*Continued on next page*)

Continued

REAGENT or RESOURCE	SOURCE	IDENTIFIER
Recombinant DNA		
Gateway pDONR 221 Vector	Invitrogen	Cat# 12536017
Software and algorithms		
CLC workbench 8 software	Qiagen	https://digitalinsights.qiagen.com/products-overview/discovery-insights-portfolio/analysis-and-visualization/qiagen-clc-main-workbench/
FACSDiva (v 6.2)	BD Biosciences	https://www.bdbiosciences.com/en-es/products/software/instrument-software/bd-facsdiva-software#Overview
LASX software	Leica	https://www.leica-microsystems.com/products/microscope-software/p/leica-las-x-ls/
Inkscape	https://inkscape.org/	2.7.10
Fiji	ImageJ	https://imagej.net/software/fiji/
GraphPad Prism (v 7.03)	GraphPad Software, Inc.	https://www.graphpad.com/scientific-software/prism/
Image Studio Lite (v 5.2)	LI-COR	https://www.licor.com/bio/image-studio-lite/resources
Salmon (v1.1.0)	Patro et al. (2017)	https://combine-lab.github.io/salmon/
R	https://cran.r-project.org/	3.5.1
Bioconductor	https://bioconductor.org	3.7
Tximport	Soneson et al. (2016)	https://bioconductor.org/packages/release/bioc/html/tximport.html
DESeq2	Love et al. (2014)	https://bioconductor.org/packages/release/bioc/html/DESeq2.html
Apglm	Zhu et al. (2018)	https://bioconductor.org/packages/release/bioc/html/apeglm.html
clusterProfiler	Yu et al. (2012)	https://bioconductor.org/packages/release/bioc/html/clusterProfiler.html
Dendextend	Galili (2015)	https://cran.r-project.org/web/packages/dendextend/vignettes/dendextend.html
Cell Ranger (v3.1.0)	10xgenomics	https://support.10xgenomics.com/single-cell-geneexpression/software/overview/welcome
DropletUtils	Griffiths et al. (2018)	https://bioconductor.org/packages/release/bioc/html/DropletUtils.html
Scater	McCarthy et al. (2017)	https://bioconductor.org/packages/release/bioc/html/scater.html
singleR	Aran et al. (2019)	https://bioconductor.org/packages/release/bioc/html/SingleR.html
Seurat	https://doi.org/10.1016/j.cell.2021.04.048	http://satijalab.org/seurat/
Other		
H.sapiens UCSC Reference Transcriptome	https://hgdownload.soe.ucsc.edu/goldenPath/hg38/bigZips/?C=M;O=A	refMrna.fa.gz
H.sapiens UCSC reference genome	https://hgdownload.soe.ucsc.edu/goldenPath/hg38/bigZips/?C=M;O=A	hg38.fa.gz
H.sapiens NCBI reference genoma	https://www.ncbi.nlm.nih.gov/assembly/GCF_000001405.39/	GRCh38 v93
Human Primary Cell Atlas	Mabbott et al. (2013)	https://www.humancellatlas.org/

RESOURCE AVAILABILITY

Lead contact

Further information and requests for resources and reagents should be directed to and will be fulfilled by the lead contact, Eduard Serra (eserra@igtp.cat).

Materials availability

Edited *NF1*(-/-) FiPS Ctrl1-SV4F-7 line (line NF1_C in this manuscript) generated in this study has been deposited and banked at the Spanish National Stem Cell bank (BNLC-ISCIII) under the name NF1C-FiPS-SV4F7.

Data and code availability

RNA-seq and scRNA-seq data have been deposited at EGA (https://ega-archive.org/) and are publicly available under the accession number EGA: EGAS00001005907 as of date of publication. Accession number is also listed in the key resources table.

The code used in this paper is available on Zenodo: https://doi.org/10.5281/zenodo.5808855. The DOI is also listed in the key resources table.

Any additional information required to analyzed the data reported in this paper is available from the lead contact upon request.

EXPERIMENTAL MODEL AND SUBJECT DETAILS

Patients, plexiform neurofibromas (pNFs), and tumor processing

NF1 patients diagnosed according to standard diagnostic criteria (DeBella et al., 2000) kindly provided tumor samples after giving written informed consent, with the approval by the Clinical Research Ethics Committee of Germans Trias i Pujol Hospital, Badalona, Spain. Tumor specimens were obtained after surgery of five plexiform neurofibromas (pNFs) (3PNF, 19PNF, 20PNF1, 23PNF, 30PNF) from five independent patients (two males, three females; ages 8–45 years). Immediately after excision, tumor samples were placed in DMEM medium (Gibco) containing 10% FBS (Gibco) + 1x GlutaMax (Gibco) + 1x Normocin antibiotic cocktail (InvivoGene) and shipped at room temperature to our laboratory. Tumors were processed as follows: surrounding fat tissue and skin were removed, and tumors were cut into 1-mm pieces and cryopreserved in 10% DMSO (Sigma) + 90% FBS (Gibco) until used.

pNF-derived Schwann cells (SCs) and fibroblast cultures

pNF-derived Schwann cells (SCs) and pNF-derived fibroblasts (Fbs) were isolated as described previously (Serra et al., 2000). Briefly, cryopreserved pNFs were thawed, cut into smaller pieces using a scalpel, and digested with 160 U/mL Collagenase Type 1 (Worthington, Lakewood, NJ) and 0.8 U/mL Dispase (Worthington, Lakewood, NJ) for 16 hours at 37°C, 5% CO_2. To establish SC cultures, dissociated cells were seeded onto 0.1 mg/mL Poly-L-lysine (Sigma) and 4 mg/mL Laminin (Gibco)-coated dishes in Schwann Cell Media (SCM), which is DMEM (Gibco) with 10% FBS (Gibco), 500 U/mL Penicillin/500 mg/mL Streptomycin (Gibco), 0.5 mM 3-isobutyl-1-methylxanthine (IBMX, Sigma), 2.5 mg/mL Insulin (Sigma), 10 nM Heregulin-b1 (PeproTech), and 0.5 μM Forskolin (Sigma). Cells were maintained at 37°C under a 10% CO_2 atmosphere. To establish Fb cultures, tumor dissociated cells were plated in DMEM supplemented with 10% FBS media and 1x GlutaMAX (Gibco) and 500 U/mL Penicillin/500 mg/mL Streptomycin (Gibco). Cells were maintained at 37°C under a 5% CO_2 atmosphere.

Human iPS cell culture

The following human iPSC lines were used in this study: 5PNF_TDiPSsv_MM_4; 3PNF_SiPSsv_MM_11; FiPS Ctrl1-SV4F-7. All of them are banked at the Spanish National Stem Cell Bank-Institute of Health Carlos III (BNLC-ISCIII). Their used was approved by the local ethical committee (Clinical Research Ethics Committee of Germans Trias i Pujol Hospital, Badalona, Spain, Project No PI-13-021). Human iPSCs were cultured in 1:20 diluted Growth Factor Reduced Matrigel (Corning) with mTeSR media (StemCell Technologies) and maintained at 37°C under a 5% CO_2 atmosphere. Cells were passaged, when necessary, with Accutase (Thermo Fischer Scientific).

The iPSC lines used were authenticated by PCR-based DNA fingerprinting analysis using the AmpFlSTR® Identifiler™ PCR Amplification Kit panel from Applied Biosystems.

iPSC lines and CRISPR/Cas9 gene edition

We used two *NF1*(-/-) iPSC lines derived from pNFs previously generated and extensively characterized in our lab (Carrió et al., 2019): 5PNF_TDiPSsv_MM_4 (in this article NF1_A) and 3PNF_SiPSsv_MM_11 (in this article NF1_B) and banked at the Spanish National Stem Cell bank (BNLC-ISCIII). As a control *NF1*(+/+) iPSC cell line, we used the fibroblast induced pluripotent stem cell line (FiPS Ctrl1-SV4F-7, in this article *NF1*(+/+) FiPS or WT) obtained from BNLC-ISCIII. We used a third *NF1*(-/-) iPSC line generated in our lab by CRISPR/Cas9 editing of the control FiPS Ctrl1-SV4F-7 line by using the ArciTect ribonucleoprotein (RNP) system from StemCell Technologies. The sgRNA targeting exon 2 of the NF1 gene (GTTGTGCTCAGTACTGACTT) was introduced into the cells using TransIT-X2 transfection reagent (Mirus) following manufacturer's instructions. Single-cell clones were generated, amplified and DNA was extracted to analyze *NF1* mutations by DNA Sanger sequencing. For the sequencing of each allele, the Gateway Technology

cloning method (Invitrogen) was performed using the pDONR 221 vector. Transformed *E. coli* DH5α grew in kanamycin. Sequences were analyzed using CLC workbench 8 software (Qiagen).

The new established edited *NF1*(-/-) iPSC line (named NF1_C in this article) was fully characterized for pluripotency and differentiation potential, and karyotype analysis at the Barcelona Stem Cell Bank (node of the BNLC-ISCIII) following standard methodology (see Figure S2).

Animal models

All mouse experiments were conducted in accordance with relevant Spanish national laws (RD 1201-/2005) and international guidelines and regulations (European Union rules 2010/63/UE), about protection of animals used for experimentation and other scientific purposes. The experimental protocols were approved by the IDIBELL Animal Ethic Experimentation Committee (CEEA-IDIBELL approval No 9111) in Spain and complied with International Association for Assessment and Accreditation of Laboratory Animal Care procedures (AAALAC). Six-week-old male nude mice (Harlan) were used and maintained under sterile air flow isolators conditions, artificial light-dark cycle of 12 hours, regulated temperature of 22°C, relative humidity of 55%, and fed with autoclaved standard food and acidified water *ad libitum*.

METHOD DETAILS

Differentiations toward neural crest (NC) and Schwann cells (SCs) in 2D

Neural crest (NC) differentiation was performed as described by Menendez et al. (2013), with some modifications previously reported in Carrió et al. (2019).

The SC differentiation protocol was based on the protocol described by Ziegler et al. (2011), with some modifications reported in Carrió et al. (2019). Briefly, 4 x 10^4 NC cells/cm^2 were plated onto 0.1 mg/mL Poly-L-lysine (Sigma) and 4 mg/mL Laminin (Gibco)-coated plates and cultured in SC differentiation medium: DMEM:F12 (3:1) (Gibco); 100 U/mL Penicillin/100 mg/mL Streptomycin antibiotics (Gibco); 1% FBS (Gibco); 5 μM Forskolin (Sigma); 50 ng/mL Heregulin β1 (Peprotech); and 2% N2 supplement (Gibco). The medium was replaced twice a week and samples were collected at 7, 14, and 30 days for subsequent analysis.

Differentiation towards SC in 3D: spheroid generation

4 x 10^4 NC cells/cm^2 were plated onto 0.1 mg/mL poly-L-lysine (Sigma) and 4 mg/mL laminin (Gibco)-coated plates and cultured in SC differentiation medium with modifications: DMEM:F12 (3:1) (Gibco); 100 U/mL Penicillin/100 mg/mL Streptomycin antibiotics (Gibco); 1% FBS (Gibco); 0.5 μM Forskolin (Sigma); 50 ng/mL Heregulin β1 (Peprotech); and 2% N2 supplement (Gibco). At day 5, cells were detached from plates using Accutase, counted using a hemocytometer (Neubauer chamber), and 1.2 x 10^6 SC differentiating cells were transferred into a well of an AggreWell™800 24-well plate (Stem Cell Technologies) in SC differentiation media. To generate heterotypic spheroids, 8.4 x 10^5 of 5-day differentiating SCs were transferred together with 3.6 x 10^5 pNF-derived Fbs into AggreWell™ 800 plates. The medium was changed twice a week slowly removing 1 mL and replacing 1 mL of fresh SC differentiation medium. Nine days after (a total of 14 days of SC differentiation), spheroids were collected and processed for subsequent analysis.

RNA extraction and RT-qPCR analysis

Total RNA from primary cells, iPSCs, NC cells, differentiating SCs, and spheroids was extracted using the 16 LEV simplyRNA Purification Kit (Promega) following manufacturer's instructions in the Maxwell 16 Instrument (Promega). RNA was quantified with a Nanodrop 1000 spectrophotometer (Thermo Scientific). RNA (0.5 μg) was reverse-transcribed using the Superscript III reverse transcriptase enzyme (Life technologies) according to manufacturer's instructions. Quantitative polymerase chain reaction (qPCR) was performed with Roche Universal Probe Library (UPL) technology and analyzed using the Light-Cycler® 480 Real-Time PCR System (Roche Diagnostics). Gene expression was normalized to two selected reference genes (*EP300* and *TBP*) and expressed as Normalized Relative Expression (NRE). Primer sequences used are listed in Table S2. We analyzed and graphically represent data using Microsoft Excel spreadsheet (Terribas et al., 2013) and GraphPad Prism (version 7.03).

RNA-seq and analysis

RNA-seq libraries were prepared in the IGTP Genomics Core Facility using the TruSeq stranded mRNA Illumina, quantified with the KAPA library quantitation kit for Illumina GA and the Agilent Bioanalyzer, and sequenced at Centre Nacional d'Anàlisis Genòmic (CNAG) in Barcelona in a HiSeq platform pooling 3 samples per lane (paired-end, 2x100).

RNA-seq data was aligned with Salmon v1.1.0 (Patro et al., 2017) against the reference genome and transcriptome (UCSC's refMrna and hg38 genome). We imported transcript-level estimates into R and summarized them to gene-level using tximport (Soneson et al., 2016). We then filtered out genes with less than 5 counts in more than one sample and generated a principal component analysis (PCA) plot to check the general quality of the samples. To build the NC-SC differentiation roadmap from the control samples (WT), we identified differentially expressed genes (DEG) between all timepoint pairs using DESeq2 (Love et al., 2014) with Wald test and the Bayesian shrinkage estimator *apglm* (Zhu et al., 2018). We considered a gene a stage specific marker if it was significantly upregulated (adjusted p-value < 0.05) in that stage when compared with other stages. Genes specific to the 30 days stage

were tested for functional enrichment using clusterProfiler (Yu et al., 2012). Likewise, to identify genes specific to the differentiation of each *NF1*(-/-) cell line while accounting for the lack of replicates, we selected the genes upregulated (log fold-change > 0, irrespective of p-value) at 30 days compared with other stages and performed functional enrichment.

To create the heatmaps, we standardized all logcounts subtracting the mean and dividing by the standard deviation considering all samples and using that value to set the color of each cell. The dendrogram was computed with the Euclidean distance and plotted with the dendextend R package (Galili, 2015).

To explore the transcriptional profile of heterotypic spheroids (Data S4) we selected the roadmap genes with standardized logcounts greater than 0 in NF1_B and NF1_C cell lines. Genes that were differentially expressed in a comparison between SC and Fb (following the methods stated above) were marked.

Single-cell RNA-Seq and analysis

scRNA-seq analysis was performed at CNAG in Barcelona. pNFs were thawed and digested, as explained above. Then, the Dead Cell Removal MicroBeads kit (Miltenyi Biotec) was used to eliminate dead cells. Cells were then resuspended in DMEM + 10% FBS (Gibco) + 1x GlutaMAX (Gibco), filtered with a 40 μm filter and cell viability was calculated with the TC20^{TM} Automated Cell Counter (Bio-Rad). Cells were run in the Chromium Single Cell Gene Expression (10X Genomics) to build the 3' transcriptome libraries and sequenced in 2 lanes on an Illumina sequencer for a mean of 225.8 million reads pairs per sample.

FASTQ files were processed with Cell Ranger version 3.1.0 (10× Genomics) using the count pipeline and the pre-built reference package version 3.0.0, based on GRCh38 and Ensembl version 93. UMIs per gene per cell matrices were then loaded into R using DropletUtils (Griffiths et al., 2018). We performed quality check, filtering and normalization using scater (McCarthy et al., 2017) before selecting the top 10% genes with highest variability. We performed a dimensionality reduction step with PCA and T-distributed Stochastic Neighbor Embedding (TSNE) followed by a clustering based on k-nearest neighbors. We used singleR (Aran et al., 2019) and the Human Primary Cell Atlas (Mabbott et al., 2013) to assign cell types to each cell cluster. To assign cells in the SC component NC early differentiating and committed identities, we first defined three gene sets from the stage-specific markers identified in control cells: NC, 7 and 14 days for early differentiating and 30 days for committed. We computed a score for each cell and gene set with the function AddModuleScore from Seurat (https://doi.org/10.1101/2020.10.12.335331) and normalized it by L2-normalization. Each cell was assigned to the gene-set with the highest normalized score if any of them was greater than zero.

Western Blot

Cells were washed twice with chilled PBS and lysed with RIPA buffer (50 mM Tris-HCl (pH 7.4), 150 mM NaCl (Merck), 1mM EDTA (Sigma), 0.5% Igepal CA-630 (Sigma)) supplemented with 3mM DTT (Thermo Fisher), 1mM PMSF (Sigma), 1mM sodium orthovanadate (Sigma), 5mM NaF (Sigma), 10 ug/ml leupeptin (Sigma), 5ug/ml aprotinin (Sigma) and 1xPhosSTOP (Roche). Lysates were quantified using the Pierce BCA Protein Assay Kit (Thermo Fisher Scientific). Lysates were boiled with 1X Laemmli buffer (50% glycerol (v/v) (Sigma), 10% SDS (m/v) (Merck) , 0.05% bromophenol blue (m/v) (Sigma), 25% Tris HCl 1M pH 6.8 (v/v) (Millipore), 5% beta-mercaptoethanol (v/v) (Sigma) in distilled water) and 90 μg of protein was subjected to SDS-PAGE and transferred onto PVDF membranes (18 hours 90 mA at 4°C). Membranes were blocked with Odyssey Blocking Buffer (TBS, LI-COR) and incubated with rabbit anti-NF1 Antibody (Bethyl laboratories) at 4°C overnight; and with mouse anti-αtubulin (Sigma) 1 hour at room temperature. Membranes were then incubated with IRDye 680RD anti-Rabbit and IRDye 800CW anti-Mouse secondary antibodies (1:10,000 each, LI-COR) for 1 hour at room temperature and scanned with the Odyssey CLx (LI-COR) using the Image Studio Lite (LI-COR).

Flow cytometry of pNFs

Cryopreserved pNF pieces were thawed and digested as previously mentioned to obtain a single-cell suspension. Then, cells were washed with 1% BSA (Sigma) in PBS, incubated for 30 minutes on ice with unconjugated primary antibody p75 (1:1000), washed with 1% BSA in PBS, incubated with Alexa Fluor 488-conjugated secondary antibodies 1:1000 for 30 minutes on ice. Cells were then permeabilized with saponin (Thermo Fisher Scientific) for 10 minutes on ice, incubated with unconjugated primary antibody S100B (1:1000) for 30 minutes on ice, washed with 1% BSA in PBS, incubated with Alexa Fluor 647-conjugated secondary antibodies (Thermo Fisher Scientific) for 30 minutes on ice, washed with 1% BSA in PBS and resuspended in 100 μL of 1% BSA in PBS. Cells were analyzed by flow cytometry using BD LSR Fortessa SORP and BD FACSDiva 6.2 software. Doublets were discarded. At least 100 cells were counted for each p75+/S100B-, p75+/S100B+, p75-/S100B+, and p75-/S100B- cell population.

Engraftment experiments

For the first engraftment experiment, 2 x10^6 cells resuspended in 100 μL SC differentiation medium of control *NF1*(+/+) WT and the *NF1*(-/-) NF1_A and NF1_B at NC stage, and 7 and 14 days of SC differentiation were injected into the exposed sciatic nerve of the mice using a 27G syringe. There were 2 mice per experimental condition; each mouse received two injections, one in the right sciatic nerve and the other in the left sciatic nerve making a total of 4 injections per group.

For the 3D spheroid engraftment experiment, spheroids containing a total of approximately 2 million cells were resuspended in 1:2 diluted Growth Factor Reduced Matrigel (in a total volume of 70 μL SC differentiation medium) and injected into the exposed sciatic nerve of the mice using a 25 G syringe. We injected a *NF1*(+/+) control cell line and the 3 independent *NF1*(-/-) cell lines (NF1_A, NF1_B and NF1_C). For each cell line, we injected homotypic and heterotypic spheroids. As *NF1*(+/+) homotypic spheroids could

not be generated, instead, we injected *NF1*(+/+) heterotypic spheroids as controls. pNF-derived Fbs used for the formation of spheroids were also injected to control their capacity to engraft and generate cell growth as single cultures.

In both experiments, tumor growth was monitored by manual palpation, and after 4 months, mice were euthanized and tumors fixed in formalin for paraffin embedding or processed for OCT embedding.

Immunocytochemical analysis

Cells were fixed in 4% paraformaldehyde (PFA) (Chem Cruz) in PBS for 15 minutes at room temperature, permeabilized with 0.1% Triton-X100 in PBS for 10 minutes, blocked in 10% FBS in PBS for 15 minutes, and incubated with the primary antibodies, p75 and S100B overnight at 4°C. Secondary antibodies were Alexa Fluor 488- and Alexa Fluor 568- (Thermo Fisher Scientific). Nuclei were stained with DAPI (Stem Cell Technologies, 1:1000). Slides were mounted with Vectashield (Vector laboratories), and coverslips were secured with polish nail.

Spheroids were fixed in 4% PFA (Chem Cruz) in PBS for 30 minutes at room temperature. The staining protocol was the same as for cells.

Fluorescent and phase contrast images from cells and spheroids were captured using the DMI 6000B microscope (Leica) and LAS X software (Leica).

Confocal microscopy

Confocal microscopy visualization of spheroids was performed using an Abberior STEDYCON confocal/STED microscope (Gottingen, Germany) mounted on the inverted Nikon Eclipse Ti2-U body (Amsterdam, Netherlands) equipped with a 100×/1.45 NA oil immersion objective. Tiled image Z-stacks for each channel (Excitation: 405 nm, 488 nm and 561 nm) were acquired sequentially at each pixel position with the following parameters: pinhole size: 1.1 Airy, XY pixel size: 300 nm, Z pixel size: 500 nm. Following acquisition, images were stitched and deconvolved (default express deconvolution parameters) using SVI Huygens software. Maximum projections of 3 consecutive Z slices as well as cropping and thresholding was performed using Fiji (ImageJ distribution) software.

Immunohistochemical analysis of paraffin samples

Tumors were embedded in paraffin, cut into 5 μm slices, and Hematoxylin & Eosin (H&E), toluidine blue staining and S100B, SOX10 and Ki67 immunostaining was performed in the IGTP-Germans Trias i Pujol University Hospital (HUGTP) Biobank Facility and Anatomy pathology Department, using standard protocols.

Immunohistochemical staining was performed on glass slides after deparaffination and rehydration of formalin-fixed paraffine embedded tissue. The automatic processing was performed in a Benchmark Ultra (Ventana). Briefly, rehydrated slides were subjected to heat antigen retrieval in CC1 buffer, incubation with primary antibodies and development with the Ultraview DAB detection system (Ventana).

Fluorescent immunohistochemistry of paraffin samples

Sections were rehydrated using standard procedures, and antigen retrieval was performed by boiling the samples in citric acid for 10 min. Samples were permeabilized in 0.3% Triton-X in PBS for 30 min at room temperature, blocked in 1% bovine serum albumin, 10% goat serum (Gibco), 0.1% Triton-X in PBS for 1 hour at room temperature, and incubated with primary antibodies (S100B, Ku80) diluted in incubation buffer (1% bovine serum albumin with 10% goat serum in PBS and 0.3% TritonX100) overnight at 4°C. Then, slides were washed 3 times for 10 minutes each in PBS1X, incubated with secondary antibodies (Alexa Fluor 488 goat anti-mouse, and Alexa Fluor goat 568 anti-rabbit, 1:1000 each) diluted in incubation buffer for 45 minutes, washed again and incubated with DAPI (Stem Cell Technologies, 1:1000) diluted in PBS for 10 minutes. Sections were mounted with Vectashield (Vector laboratories) and secured with polish nail. Images were captured using the DMI 6000B microscope (Leica) and LAS X software (Leica).

Fluorescent immunohistochemistry of OCT samples

Tissue samples were fixed in 4% PFA overnight at 4°C. Then samples were incubated in 15% sucrose solution until the tissue shrunk, and in 30% sucrose solution overnight at 4°C. Samples were then embedded in optimal cutting temperature (OCT) compound (VWR) and frozen at −80°C. 5 μm OCT slices were cut for subsequent staining. OCT was removed by PBS washing, and antigen retrieval was performed with citric acid boiling the samples for 10 min. Tissue sections were permeabilized in 0.3% TritonX100 in PBS for 30 minutes. Afterwards, samples were incubated in blocking buffer (0.1% TritonX100, 1% BSA with 10% goat serum (Gibco) in PBS) for 1 hour and incubated with primary antibodies (hNu, S100, GAP43) diluted in incubation buffer (0.1% TritonX100, 1% BSA with 10% goat serum in PBS) overnight at 4°C. Tissue sections were then washed and incubated with secondary antibodies (Alexa Fluor 488 anti-mouse, 1:1000) diluted in incubation buffer 2 hours at room temperature. After washing, sections were incubated with DAPI (Stem Cell Technologies, 1:1000) diluted in PBS1X for 10 minutes and mounted with Vectashield (Vector laboratories). Images were captured using the DMI 6000B microscope (Leica) and LAS X software (Leica).

QUANTIFICATION AND STATISTICAL ANALYSIS

For RT-qPCR analysis (Figure S2) data was analyzed and graphically represented using Microsoft Office Excel spreadsheet (Terribas et al., 2013) and GraphPad Prism (version 7.00). Quantitative data are shown as the mean ± standard error (SEM) of three differentiation experiments. No statistical test was performed on this data.

Bioinformatic analysis of RNA-seq and scRNA-seq is thoroughly described in the "RNA-seq and analysis" and "Single-cell RNA-seq and analysis" in the method details section, including the exact software and statistical methods used. We applied the default multiple testing correction recommended by the different software packages when applicable. Significance level was established at $p < 0.05$ except if otherwise stated. The meaning of value of n, and/or dispersion and precision measure (SEM) can be found in the Figure legends and Results section. Sample sizes for mice experiments can be found in Figure legends and Table S1.

Cell Reports, Volume *38*

Supplemental information

Modeling iPSC-derived human neurofibroma-like tumors in mice uncovers the heterogeneity of Schwann cells within plexiform neurofibromas

Helena Mazuelas, Míriam Magallón-Lorenz, Juana Fernández-Rodríguez, Itziar Uriarte-Arrazola, Yvonne Richaud-Patin, Ernest Terribas, Alberto Villanueva, Elisabeth Castellanos, Ignacio Blanco, Ángel Raya, Jakub Chojnacki, Holger Heyn, Cleofé Romagosa, Conxi Lázaro, Bernat Gel, Meritxell Carrió, and Eduard Serra

Figure S1

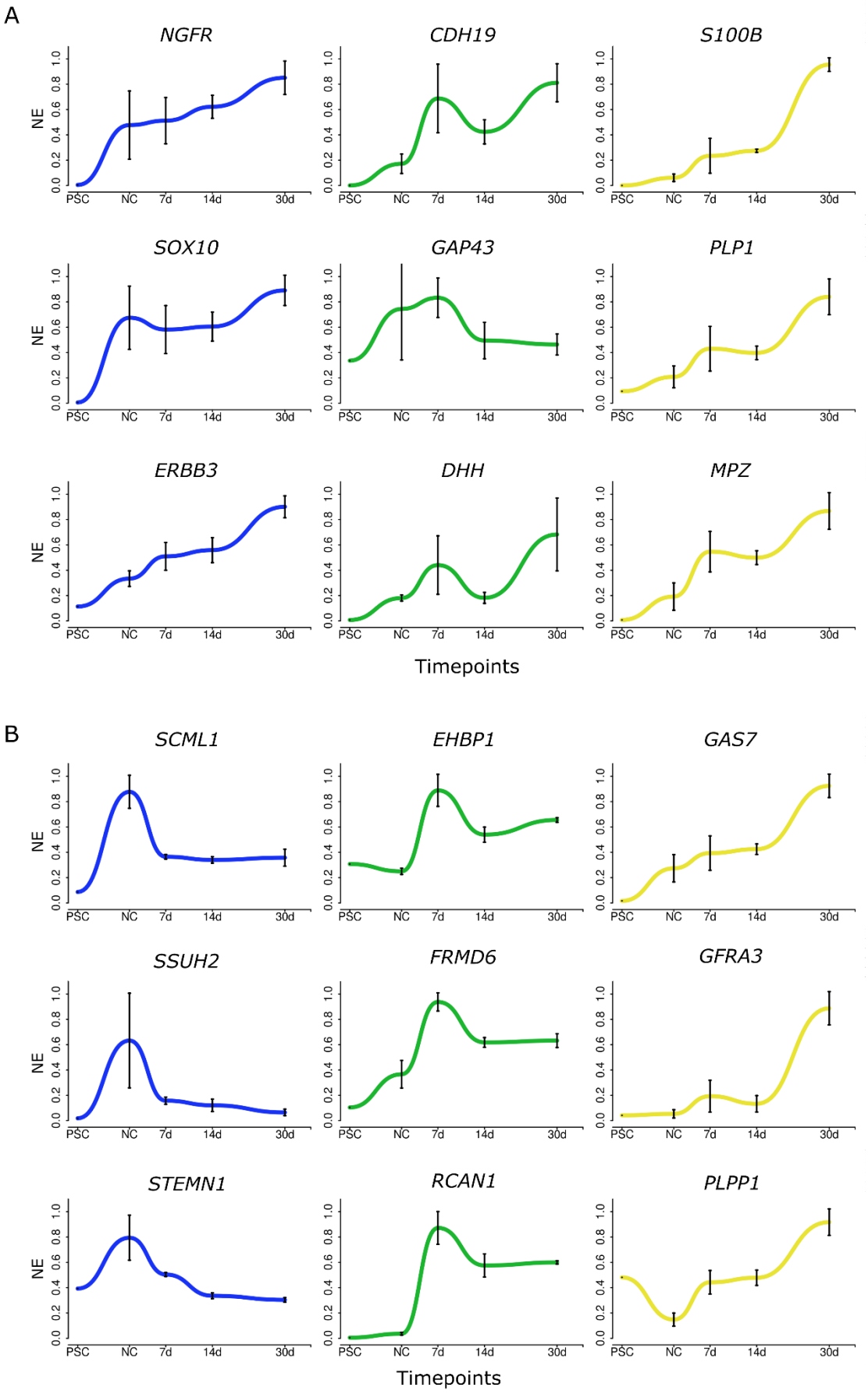
A
NGFR
CDH19
S100B
SOX10
GAP43
PLP1
ERBB3
DHH
MPZ
NE
0.0 0.2 0.4 0.6 0.8 1.0
PSC NC 7d 14d 30d
Timepoints
B
SCML1
EHBP1
GAS7
SSUH2
FRMD6
GFRA3
STEMN1
RCAN1
PLPP1
NE
0.0 0.2 0.4 0.6 0.8 1.0
PSC NC 7d 14d 30d
Timepoints

Figure S1. Expression dynamics of classic neural crest (NC)-Schwann cell (SC) markers and newly selected roadmap genes in *NF1*(+/+) cells, from RNA-seq analysis. Related to Figure 1. Individual graphs showing expression profile of classic **(A)** and newly identified **(B)** markers in *NF1*(+/+) control cells at five different time points during NC-SC differentiation: pluripotent stage (PSC), NC and 7, 14, and 30 days after the induction of SC differentiation. Values represent three independent differentiation experiments and are expressed as normalized expression (NE) curves, showing the mean ± SEM.

Figure S2

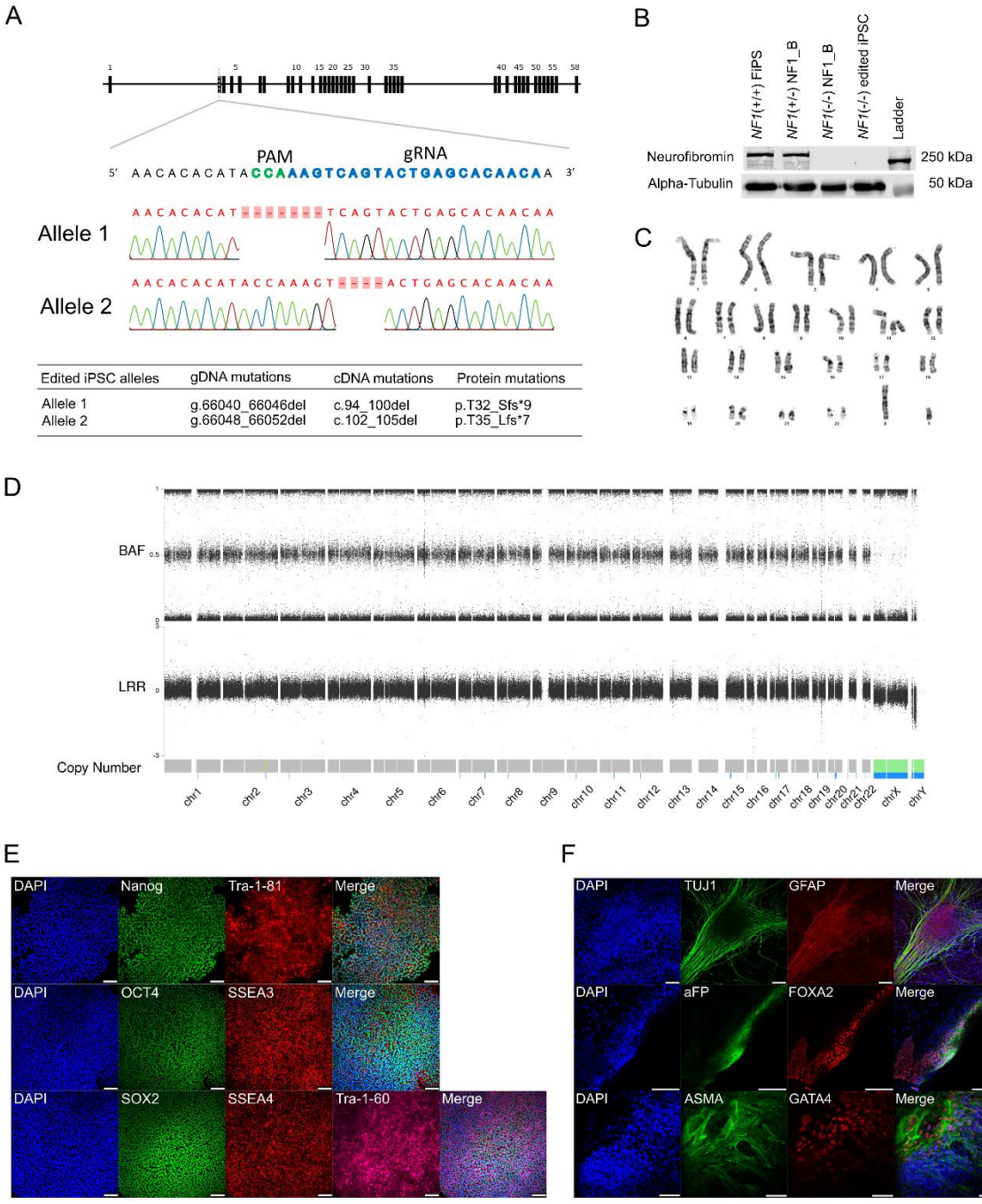

Edited iPSC alleles	gDNA mutations	cDNA mutations	Protein mutations
Allele 1	g.66040_66046del	c.94_100del	p.T32_Sfs*9
Allele 2	g.66048_66052del	c.102_105del	p.T35_Lfs*7

Figure S2. **Generation and characterization of the *NF1*(-/-) edited iPSC line (NF1_C) using CRISPR/Cas9. Related to Figure 2.** The *NF1* gene was knocked out in control *NF1*(+/+) iPSC cells (FiPS) using the Architect Ribonucleic Protein (RNP) complex system (StemCell technologies). **(A)** Schematic representation of the *NF1* gene showing the location of the designed gRNA in exon 2. Below, Sanger sequencing analysis showing edited frame shift mutations in both *NF1* alleles. Allele 1 carries a 7 bp deletion and allele 2 a 4 bp deletion. The table below indicates the exact genomic and cDNA location of these mutations. **(B)** Western blot analysis showing the absence of neurofibromin in the *NF1*(-/-) edited iPSC line generated. *NF1*(+/+) FiPS, *NF1*(+/-) NF1_B and *NF1*(-/-) NF1_B cells were used as controls. **(C)** Karyotype analysis of NF1_C iPSC line at passage 10. **(D)** Genomic structure of NF1_C cell line analyzed by SNP-array. B-allele frequency (BAF) and logR ratio (LRR) are displayed, showing the absence of copy number alterations and a 2n genome. **(E)** Characterization of pluripotency markers in NF1_C cell line. Representative images of colonies stained positive for the pluripotency associated markers NANOG, OCT4, and SOX2 (in green), TRA-1-81, SSEA3, SSEA4 (in red), and TRA-1-60 (pink). Scale bars, 100 µm. **(F)** *In vitro* differentiation potential of NF1_C iPSC line. Generation of cell derivatives of the three primary germ layers including ectoderm (TUJ1 in green and GFAP in red), endoderm (aFP in green and FOXA2 in red) and mesoderm (ASMA in green and GATA4 in red). Scale bars, 100 µm.

Figure S3

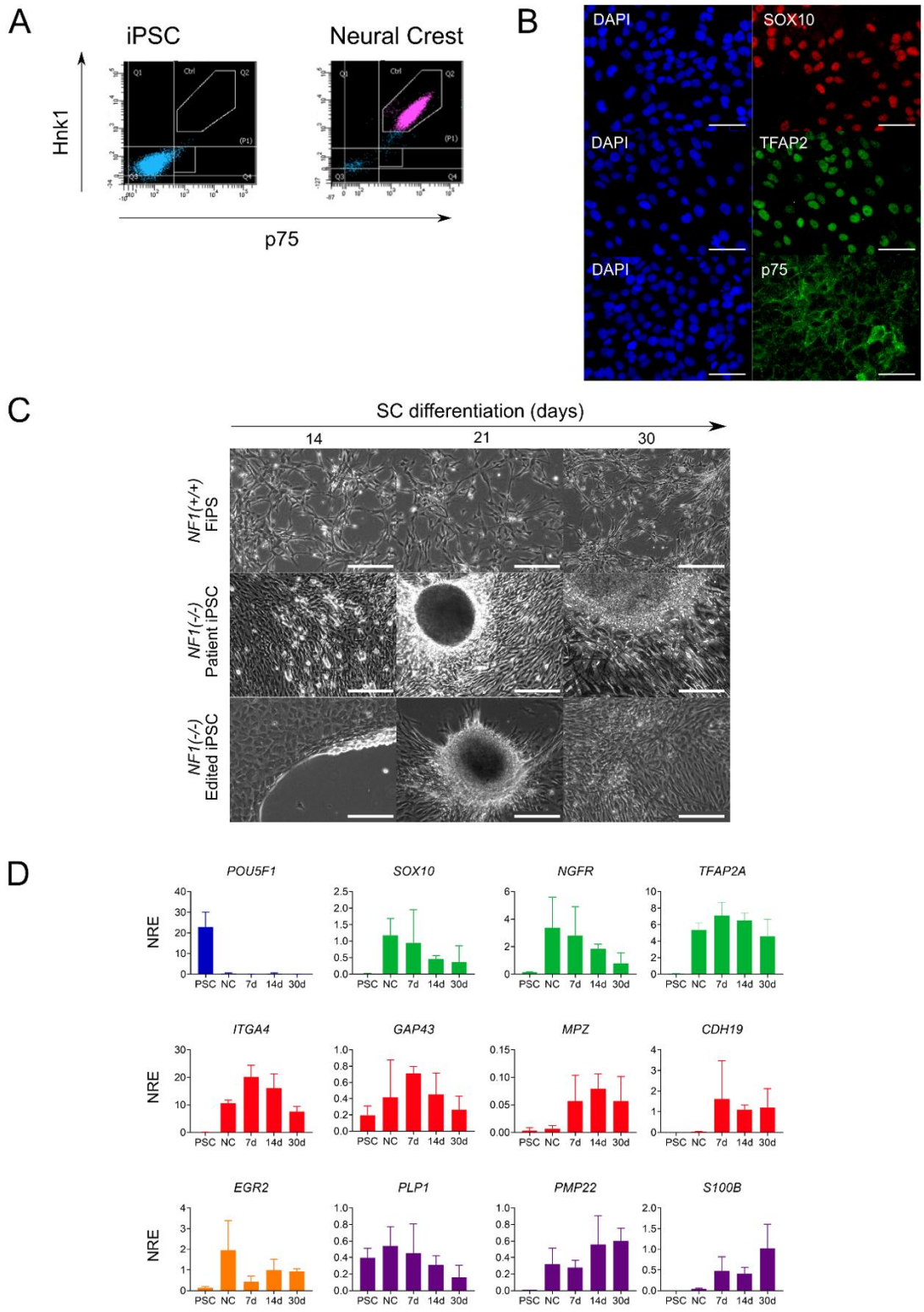
A
iPSC
Neural Crest
Hnk1
p75
B
DAPI
SOX10
DAPI
TFAP2
DAPI
p75
C
SC differentiation (days)
14
21
30
NF1(+/+) FiPS
NF1(-/-) Patient iPSC
NF1(-/-) Edited iPSC
D
POU5F1
SOX10
NGFR
TFAP2A
ITGA4
GAP43
MPZ
CDH19
EGR2
PLP1
PMP22
S100B
NRE
PSC NC 7d 14d 30d

Figure S3. Differentiation potential of the *NF1*(-/-) edited iPSC line (NF1_C) towards the neural crest (NC)- Schwann Cell (SC) lineage. Related to Figure 2. (A) Flow cytometry analysis for p75 and Hnk1 before (left graph) and after (right graph) NC differentiation of NF1_C iPSC line, following the protocol described in Carrió et al (2019). The percentage of double p75 and Hnk1-positive cells reached 98% after 24 days of NC differentiation. **(B)** Immunocytochemistry analysis showing NF1_C iPSC line differentiated to NC cells. Expression of NC lineage markers such as SOX10 (red), TFAP2 (green) and, p75 (green) are shown. Scale bar, 50 μm. **(C)** Representative bright-field images during SC differentiation (from NC cells) at different timepoints (14, 21 and 30 days), for control *NF1*(+/+) FiPS, *NF1*(-/-) patient-specific (NF1_B) iPSC line and the newly generated NF1_C iPSC line, showing the high cell density and the formation of 3D spheres in both *NF1*(-/-) cell lines. Scale bars, 50 μm. **(D)** RT-qPCR expression analysis of several NC-SC lineage markers in NF1_C iPSC line at five different time points during differentiation: pluripotent stage (PSC), NC stage and 7, 14, and 30 days after the induction of SC differentiation. Expression data is shown as the mean normalized relative expression (NRE) ± SEM from three independent differentiation experiments.

Figure S4

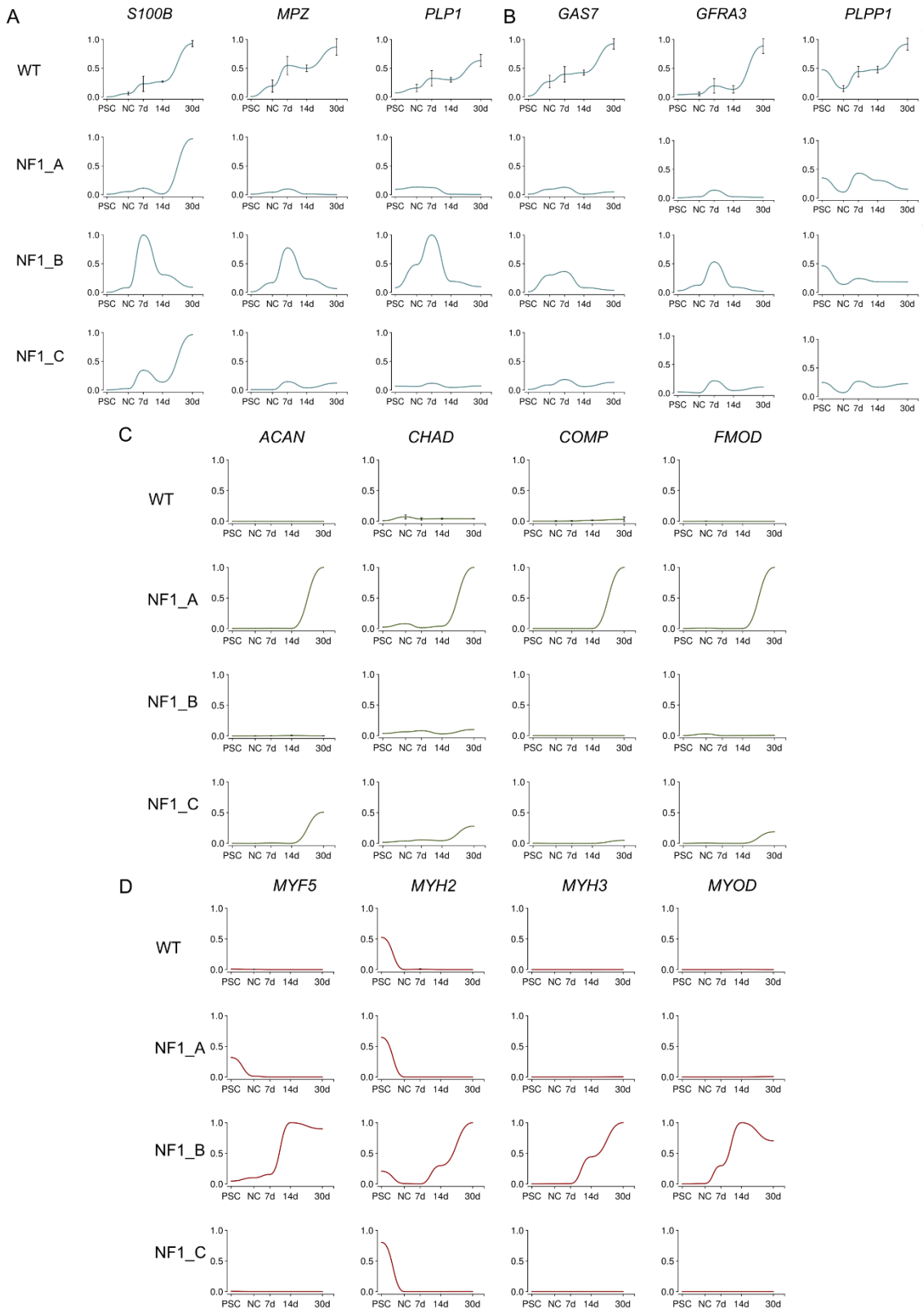
A
S100B
MPZ
PLP1
B
GAS7
GFRA3
PLPP1
WT
NF1_A
NF1_B
NF1_C
C
ACAN
CHAD
COMP
FMOD
D
MYF5
MYH2
MYH3
MYOD
1.0
0.5
0.0
PSC NC 7d 14d 30d

Figure S4. Expression pattern analysis of classic and roadmap Schwann Cell (SC) markers, and chondrocyte and muscle differentiating markers in *NF1*(+/+) (WT) and *NF1*(-/-) cell lines throughout the *in vitro* NC-SC differentiation process. Related to Figure 2. Expression pattern from RNA-seq analysis showing classic **(A)** and roadmap **(B)** SC markers, and markers of chondrocyte **(C)** and muscle **(D)** differentiation in *NF1*(+/+) (WT) and *NF1*(-/-) cell lines throughout the differentiation process. Three independent differentiation experiments are shown for the control *NF1*(+/+) WT line and values are expressed as normalized expression (NE) curves, showing the mean ± SEM. For the other three *NF1*(-/-) cell lines one experiment per cell line is shown.

Figure S5

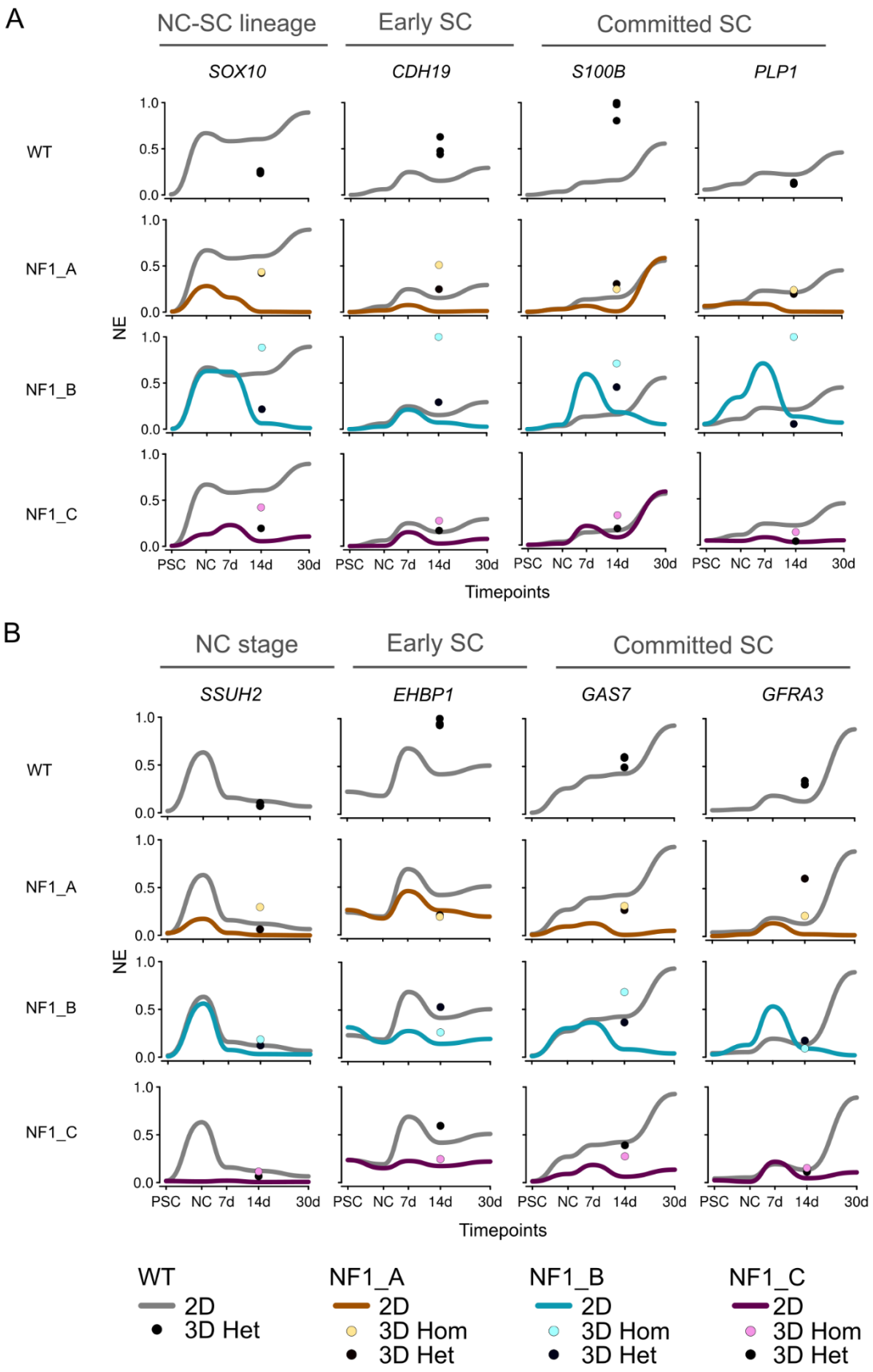
A
NC-SC lineage
Early SC
Committed SC
SOX10
CDH19
S100B
PLP1
WT
NF1_A
NF1_B
NF1_C
NE
1.0
0.5
0.0
PSC NC 7d 14d 30d
Timepoints
B
NC stage
Early SC
Committed SC
SSUH2
EHBP1
GAS7
GFRA3
WT
2D
3D Het
NF1_A
2D
3D Hom
3D Het
NF1_B
2D
3D Hom
3D Het
NF1_C
2D
3D Hom
3D Het

Figure S5. Expression pattern comparison of some neural crest (NC)- Schwann Cell (SC) markers between 2D and 3D models. Related to Figure 3. Expression pattern of classic (A) and roadmap selected (B) NC-SC markers from RNAseq data of 2D and 3D models. Each graph shows the expression of each marker throughout the 2D differentiation process (lines) for NF1(+/+) (WT) (grey line) and NF1(-/-) (NF1) (color line), and the expression of homotypic and heterotypic spheroids at 14 days of SC differentiation (color and black dots, respectively). WT n=3 (the mean of three independent differentiation experiments); *NF1*(-/-) n= 3 biological replicates (values of each cell line are graphed separately).

Figure S6

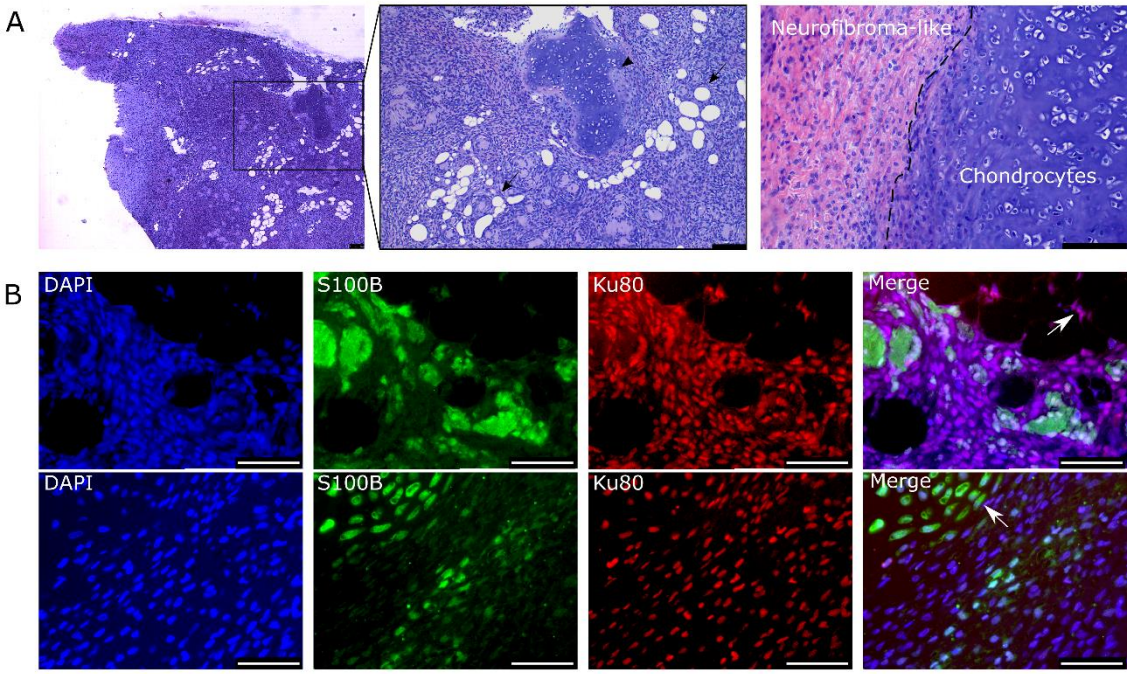
A
Neurofibroma-like
Chondrocytes
B
DAPI
S100B
Ku80
Merge
DAPI
S100B
Ku80
Merge

Figure S6. *NF1*(-/-) heterotypic spheroids generate small areas of fat and chondrocytes. Related to Figure 5. (A) H&E-stained *NF1*(-/-) heterotypic tumors showing areas of fat (black arrows) and cartilage (arrowhead) Scale bar: 100 µm. **(B)** Representative fluorescence micrographs showing expression of Ku80 (red) and S100B (green) in paraffin section of *NF1*(-/-) heterotypic tumors. Ku80 stains human nuclear cells. White arrows point human adipocyte (top) and chondrocyte (bottom) cells. Scale bar: 50 µm

Figure S7

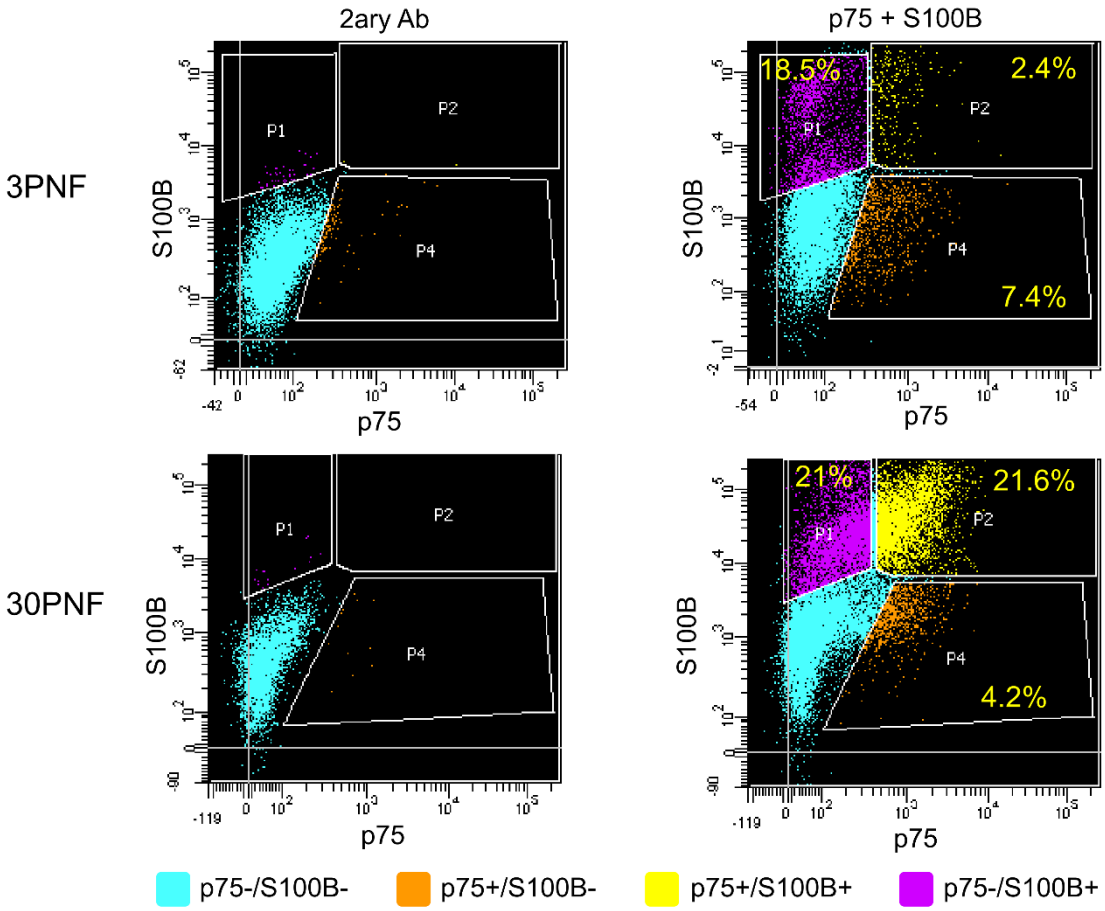
2ary Ab
p75 + S100B
3PNF
30PNF
S100B
p75
P1
P2
P4
18.5%
2.4%
7.4%
21%
21.6%
4.2%
p75-/S100B-
p75+/S100B-
p75+/S100B+
p75-/S100B+

Figure S7. Flow cytometry analysis for p75 and S100B in 2 additional human pNFs from NF1 patients (3PNF and 30PNF). Related to Figure 6. Left panel: Control non-stained cells. Right panel: p75 and S100B co-stained cells. The percentage of the different populations are shown inside each graph.

Table S1. Results from the *in vivo* spheroid engraftment experiment showing the number of grown tumors. Related to Figure 4 and 5.

	Injections	Grown tumors	NF-like tumors	% NF-like tumors NF1_B NF1_C
NF1(+/+) Heterotypic spheroids				
- FiPS	6	0		
Total	6	0 (0%)		
Fb cultures				
- 5PNF-derived	2	0		
- 3PNF-derived	2	0		
Total	4	0 (0%)		
NF1(-/-) Homotypic spheroids				
- NF1_A	6	2	2	
- NF1_B	5	2	2	2/5
- NF1_C	6	2	1	1/6
Total NF1_B&C				3/11 (27.3%)
Total	17	6 (35.3%)	5 (29.4%)	
NF1(-/-) Heterotypic spheroids				
- NF1_A	6	0	0	
- NF1_B	5	4	3	3/5
- NF1_C	6	4	4	4/6
Total NF1_B&C				7/11 (63.3%)
Total	17	8 (47.1%)	7 (41.2%)	

Table S2. Summary of the main histological characteristics of tumors grown after the engraftment of *NF1*(-/-) homotypic and heterotypic spheroids, described by an NF1 expert pathologist. Related to Figure 4 and 5.

Injected Line	Mice	Homotypic spheroids	Heterotypic spheroids
NF1_B (-/-)	A1	No tumor	**Areas of Neurofibroma-like tumor** Immature spindle cells disorganized in a myxoid background No mitosis S100B diffuse cytoplasmic and focal nuclear positivity SOX10 positive
	B1	**Areas of Neurofibroma-like tumor** Infiltrative small tumor Immature spindle cells in a fascicular pattern with a myxoid/collagenized background No mitosis S100B diffuse cytoplasmic and focal nuclear positivity SOX10 positive	**Areas of Neurofibroma-like tumor** Immature spindle cells disorganized in a myxoid/collagenized background No mitosis Presence of Meissner corpuscles S100B diffuse cytoplasmic and focal nuclear positivity SOX10 positive
	B2	No tumor	No tumor
	D1	**Areas of Neurofibroma-like tumor** Immature spindle cells disorganized in a myxoid/collagenized background No mitosis Presence of Meissner corpuscles S100B focal and cytoplasmic positivity SOX10 positive Areas of fat	**Areas of Neurofibroma-like tumor** Immature spindle cells disorganized in a myxoid/collagenized background. No mitosis Presence of Meissner corpuscles S100B diffuse cytoplasmic and focal nuclear positivity SOX10 positive
	D2	No tumor	No tumor
NF1_C (-/-)	A3	No tumor	No tumor
	A4	No tumor	**Areas of Neurofibroma-like tumor** Immature oval to spindle cells disorganized in a collagenized background mixed with few myxoid matrix. No mitosis Focal epithelioid change in some S100B cells S100B cytoplasmic diffusely positive SOX10 positive Areas of cartilage
	B3	No tumor	**Areas of Neurofibroma-like tumor** Immature oval to spindle cells disorganized in a myxoid/collagenized background No mitosis

			Focal epithelioid change in some S100B cells S100B cytoplasmic diffusely positive SOX10 positive Areas of cartilage and fat
	B4	**Areas of immature Neurofibroma-like tumor** Infiltrative tumor Immature oval to spindle cells disorganized in a myxoid background No mitosis S100B negative SOX10 negative	**Areas of Neurofibroma-like tumor** Immature oval to spindle cells disorganized in a collagenized background with few myxoid matrix No mitosis Presence of mast cells S100B diffuse cytoplasmic and focal nuclear positivity Areas of fat
	D3	No tumor	Mainly Cartilage
	D4	**Areas of Neurofibroma-like tumor** Infiltrative small tumor Immature oval to spindle cells disorganized in a myxoid background No mitosis S100B cytoplasmic diffusely positive SOX10 positive	**Areas of Neurofibroma-like tumor** Immature oval to spindle cells disorganized in a collagenized background with few myxoid matrix. No mitosis S100B cytoplasmic diffusely positive Areas of cartilage and fat
NF1_A (-/-)	C1	No tumor	No tumor
	C2	No tumor	No tumor
	C3	**Areas of Neurofibroma-like tumor** Infiltrative small tumor Immature oval to spindle cells disorganized in a myxoid background No mitosis S100B positive	No tumor
	E1	No tumor	No tumor
	E2	**Areas of Neurofibroma-like tumor** Immature oval to spindle cells disorganized in a myxoid/collagenized background No mitosis S100B cytoplasmic weak and diffusely positive	No tumor
	E3	No tumor	No tumor

Table S3. **Primers used for RT-qPCR analysis. Related to STAR Methods.**

Gene	Sequence (5´-3´)		UPL
POU5F1	*Forward*	cttcgcaagccctcatttc	60
	Reverse	gagaaggcgaaatccgaag	
NGFR	*Forward*	ccttccacgctgtctcca	60
	Reverse	cctaggcaagcatcccatc	
SOX10	*Forward*	gacacggttttccacttccta	25
	Reverse	gtcctcgcaaagagtccaac	
TFAP2A	*Forward*	ggtgaaccccaacgaagtc	73
	Reverse	accgtgaccttgtacttcgag	
S100B	*Forward*	ggaaggggtgagacaagga	73
	Reverse	ggtggaaaacgtcgatgag	
CDH19	*Forward*	tgtaccagaggaaatgaatacgac	78
	Reverse	catatatgtcacctgttctttcatca	
ITGA4	*Forward*	atgcaggatcggaaagaatc	78
	Reverse	ccacaaggttctccattaggg	
PLP1	*Forward*	cttcaacacctggaccacct	60
	Reverse	ccatgggagaacaccataca	
GAP43	*Forward*	gctccaagcctgatgagc	12
	Reverse	gctctgtggcagcatcac	
EGR2	*Forward*	gctgctacccagaaggcata	60
	Reverse	ggatgaggctgtggttgaa	
PMP22	*Forward*	ctgtcgatcatcttcagcattc	29
	Reverse	agcactcatcacgcacagac	
MPZ	*Forward*	ttcccatctcctgcatcc	55
	Reverse	ctgggccacctggtagag	
EP300	*Forward*	gcagcctgcaactccact	20
	Reverse	gaggatttgatacctgtccttca	
TBP	*Forward*	aggaattgaggaagttgctgag	67
	Reverse	cgctggaactcgtctcacta	

Data S5. Additional scRNAseq data. Related to Figure 6.

Table of contents

19PNF

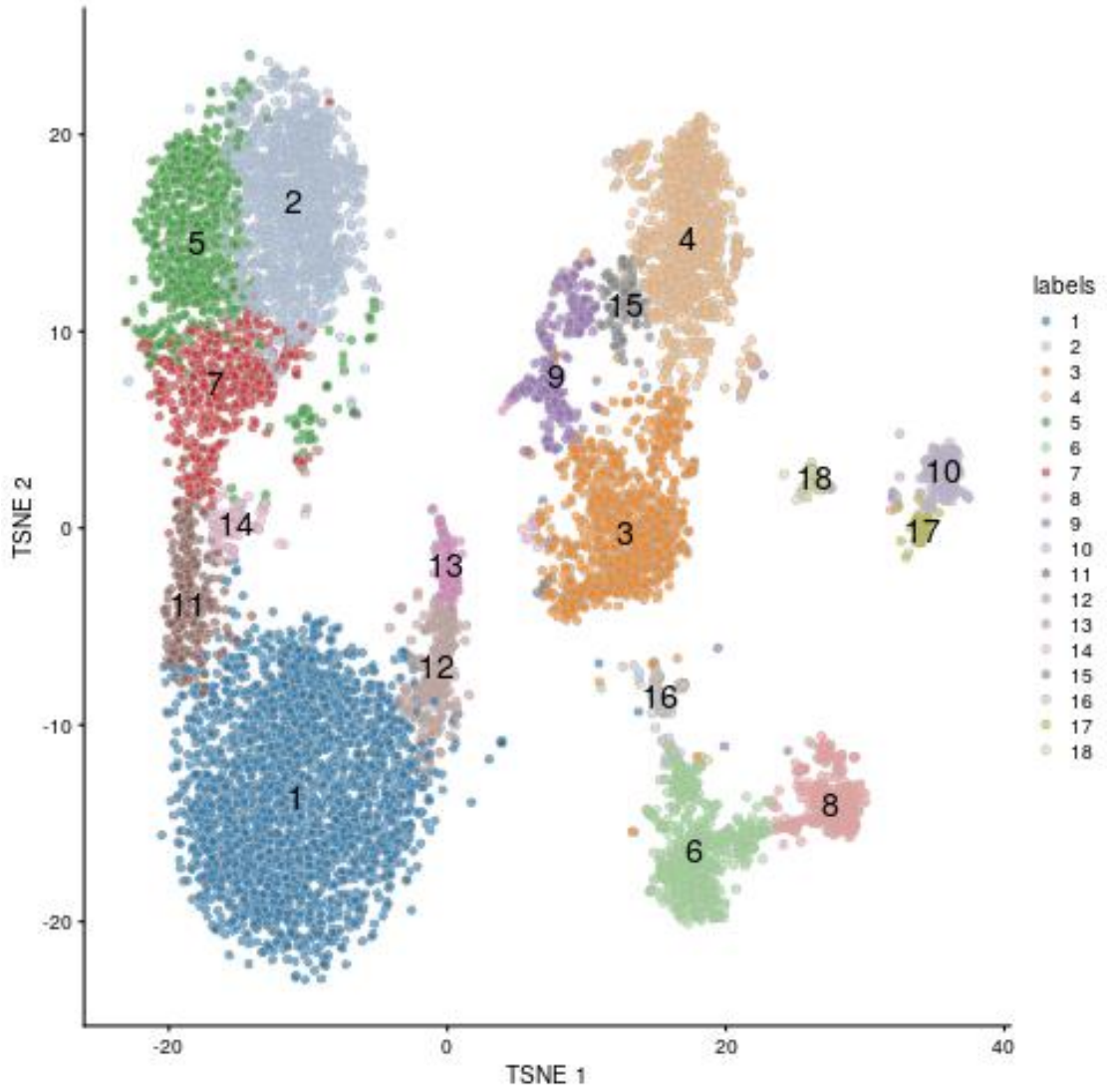

Data S5.1. T-distributed Stochastic Neighbor Embedding (TSNE) plot showing cell clustering of 19PNF. A total of 5087 cells are represented divided in 17 different clusters. Each point is a cell and each color represent a cluster.

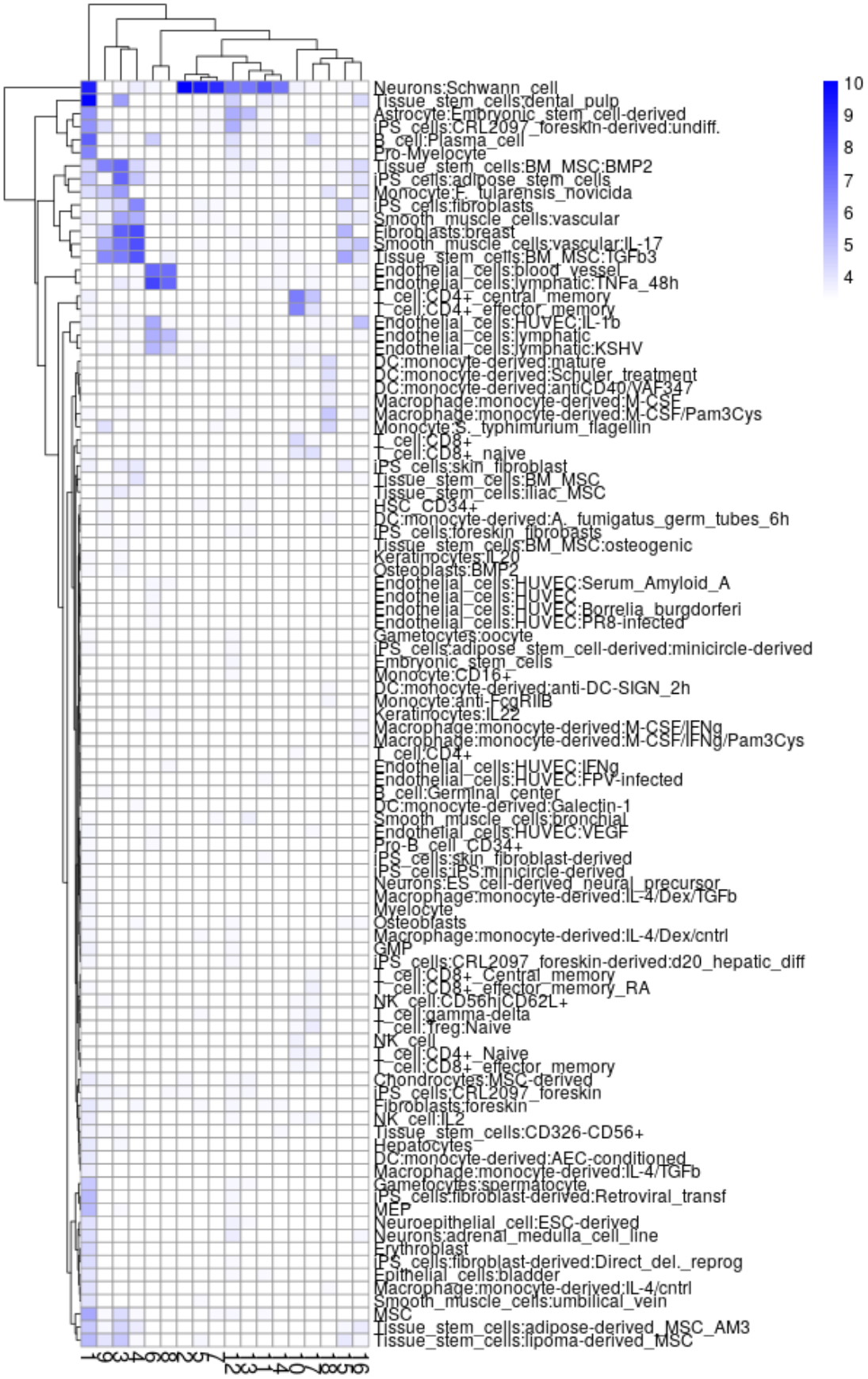

Data S5.2. Heatmap representing the annotation scoring obtained of each cluster with singleR package of 19PNF.

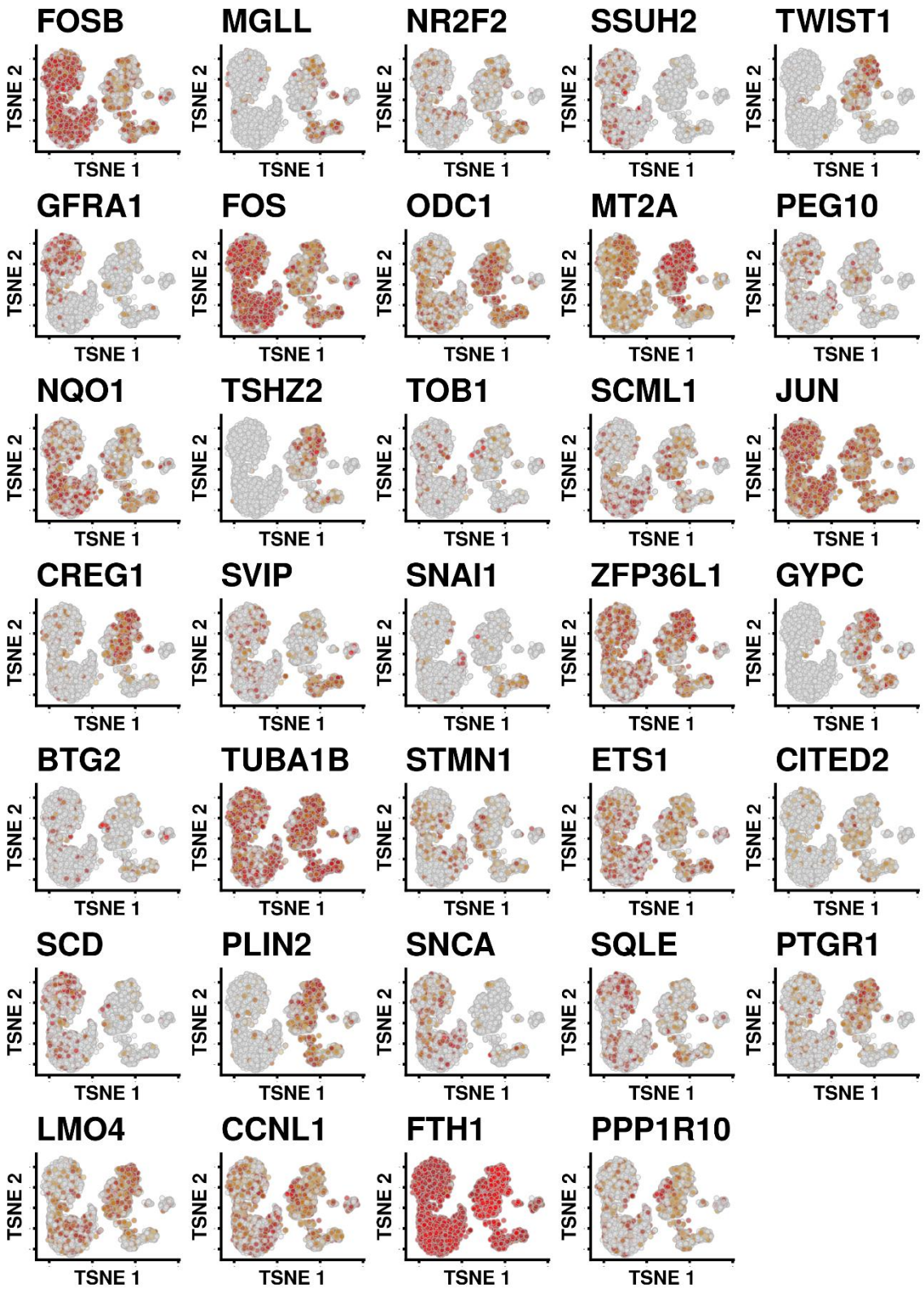

Data S5.3. 19PNF TSNE representation of single-cell RNA-seq of NC roadmap markers.

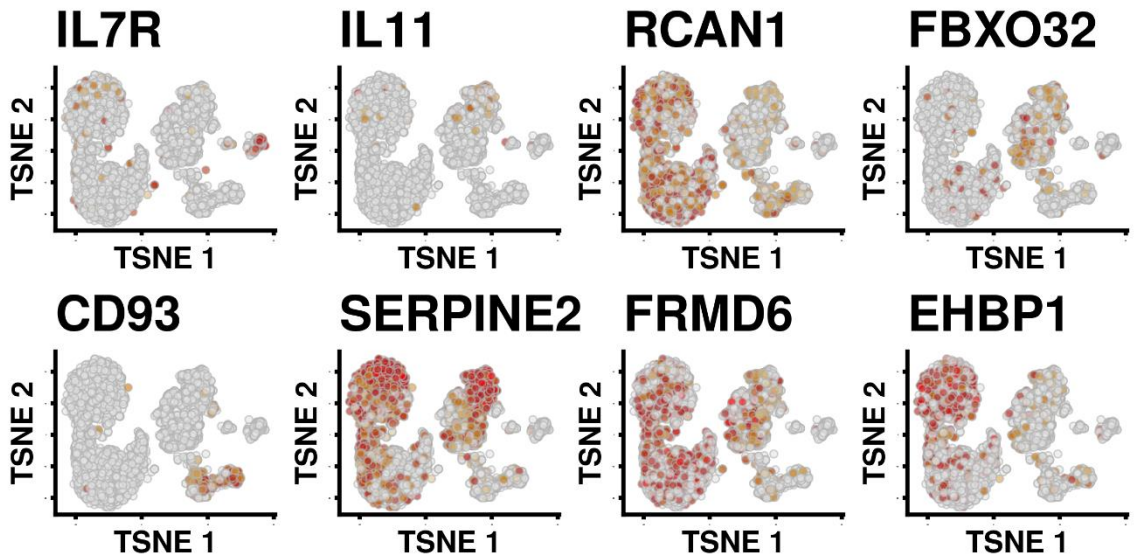

Data S5.4. 19PNF TSNE representation of single-cell RNA-seq of day 7 roadmap markers.

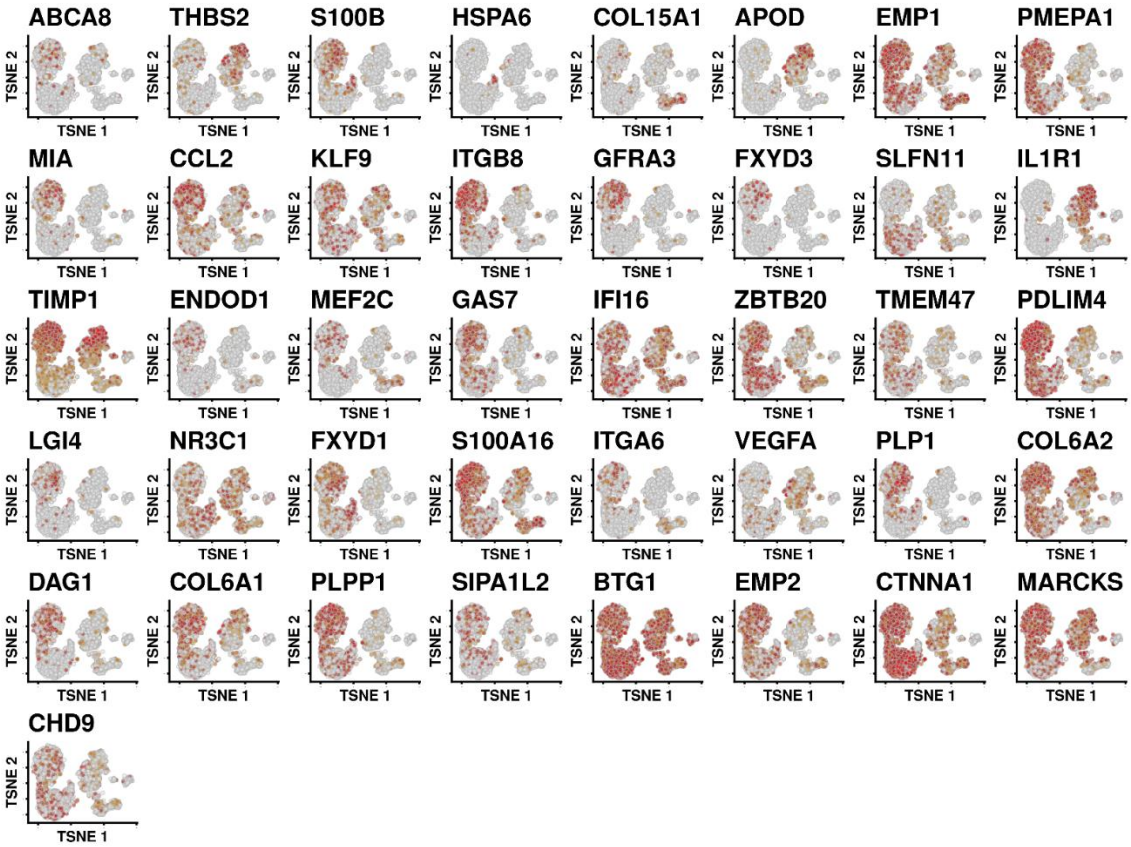

Data S5.5. 19PNF TSNE representation of single-cell RNA-seq of day 30 roadmap markers.

20PNF

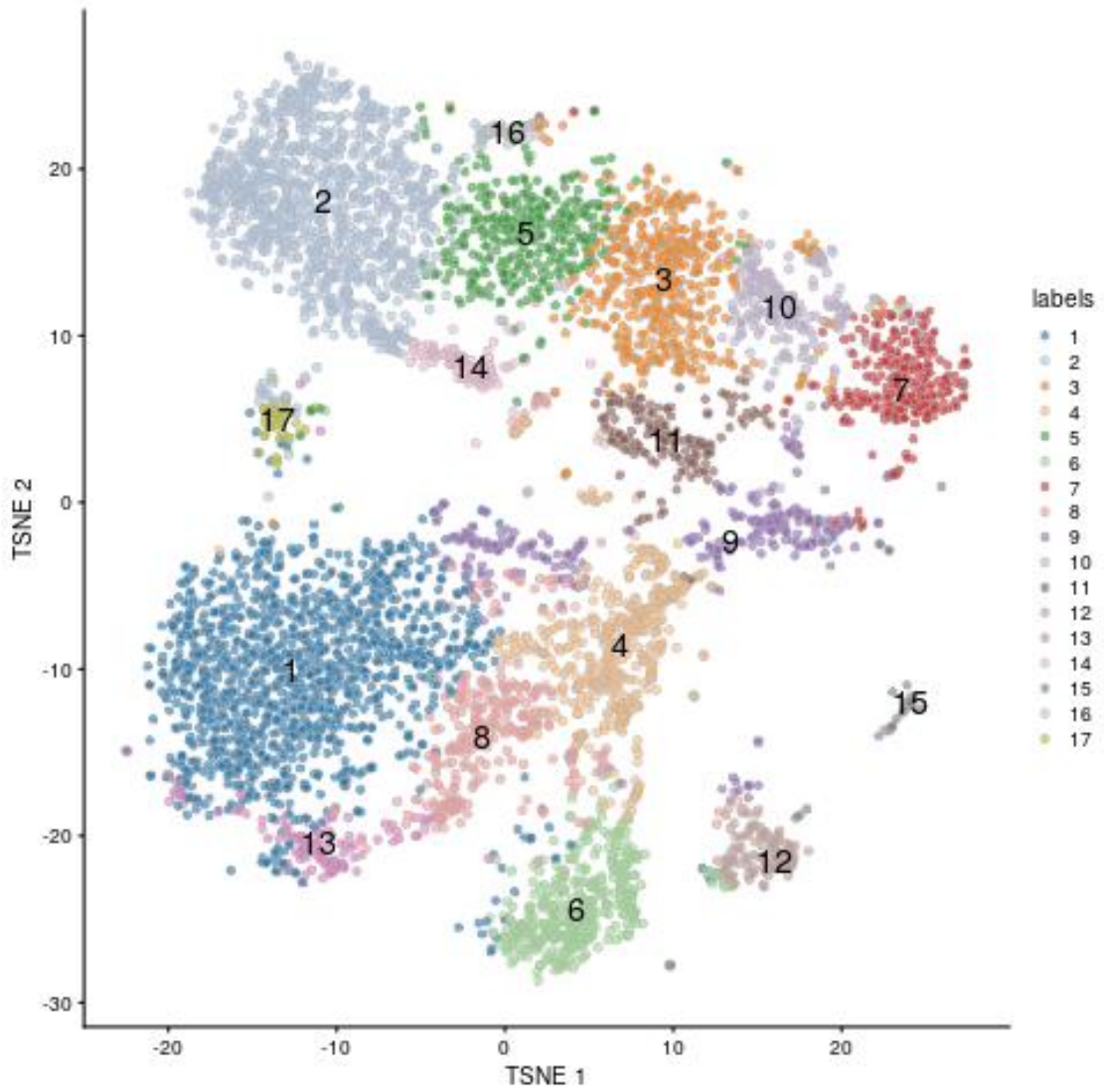

Data S5.6. TSNE plot showing cell clustering of 20PNF. A total of 6155 cells are represented divided in 17 different clusters. Each point is a cell and each color represent a cluster.

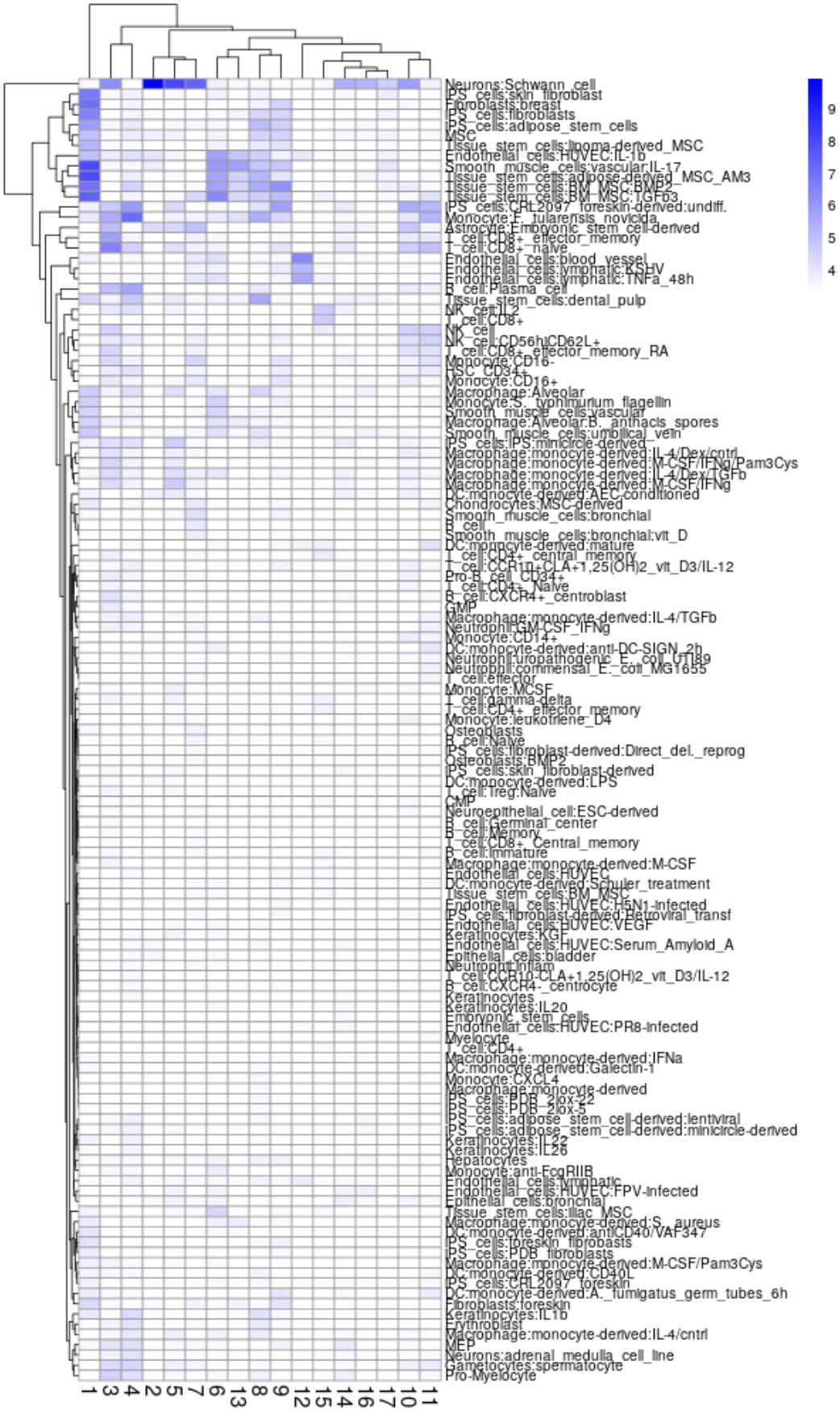

Data S5.7. Heatmap representing the annotation scoring obtained of each cluster with singleR package of 20PNF.

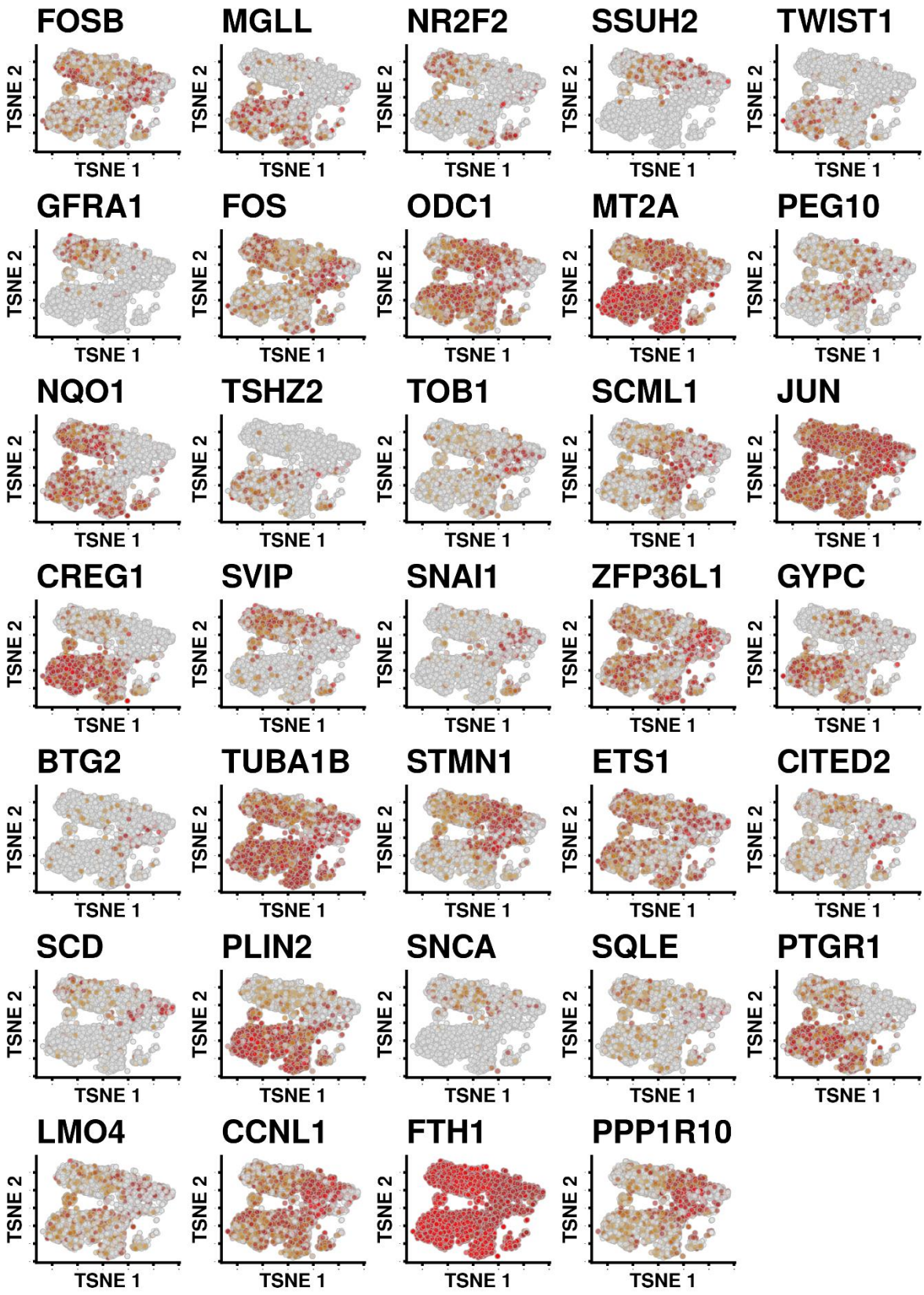

Data S5.8. 20PNF TSNE representation of single-cell RNA-seq of NC roadmap markers.

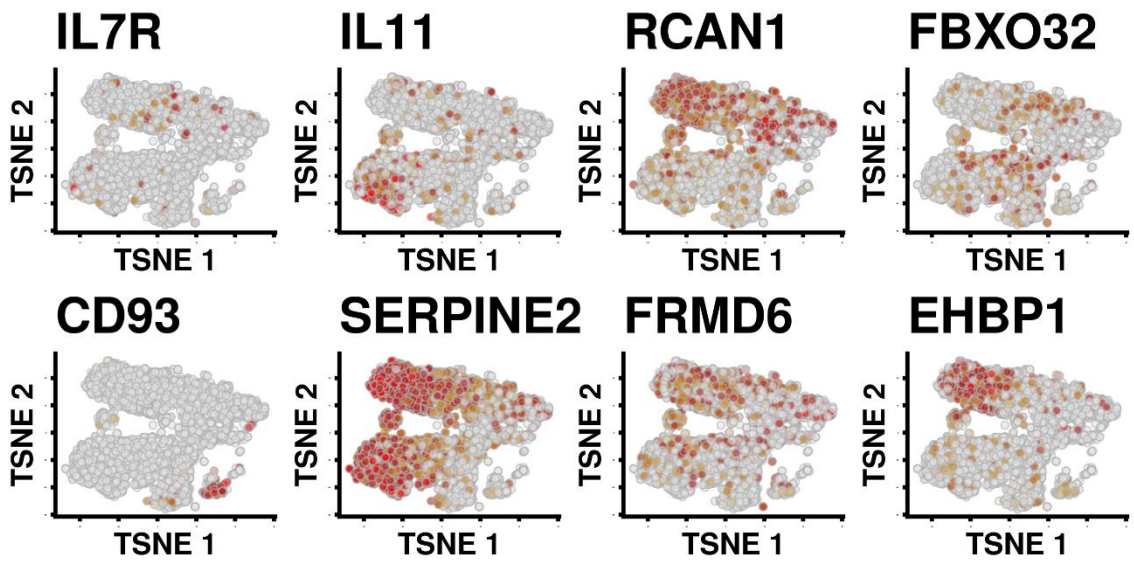

Data S5.9. 20PNF TSNE representation of single-cell RNA-seq of day 7 roadmap markers.

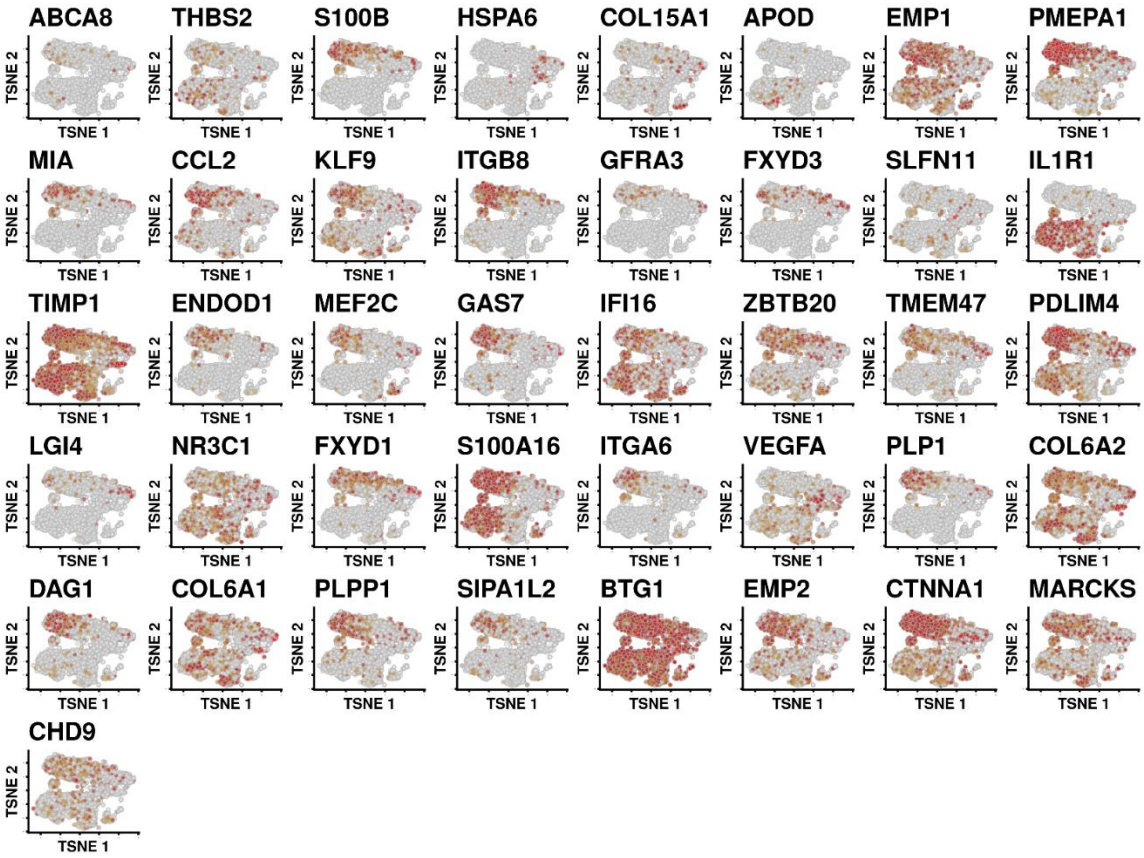

Data S5.10. 20PNF TSNE representation of single-cell RNA-seq of day 30 roadmap markers.

23PNF

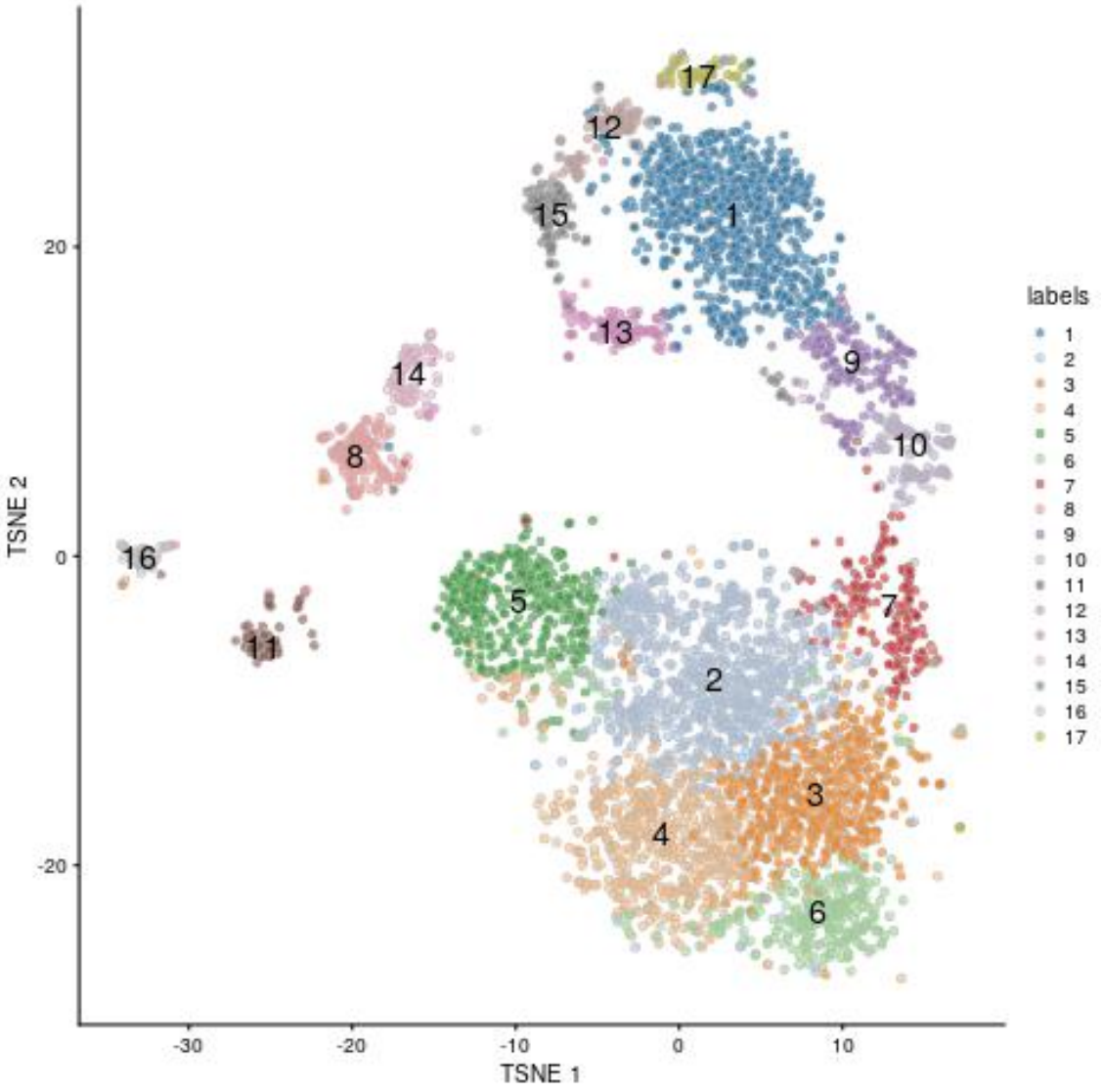

Data S5.11. TSNE plot showing cell clustering of 23PNF. A total of 9092 cells are represented divided in 17 different clusters. Each point is a cell and each color represent a cluster.

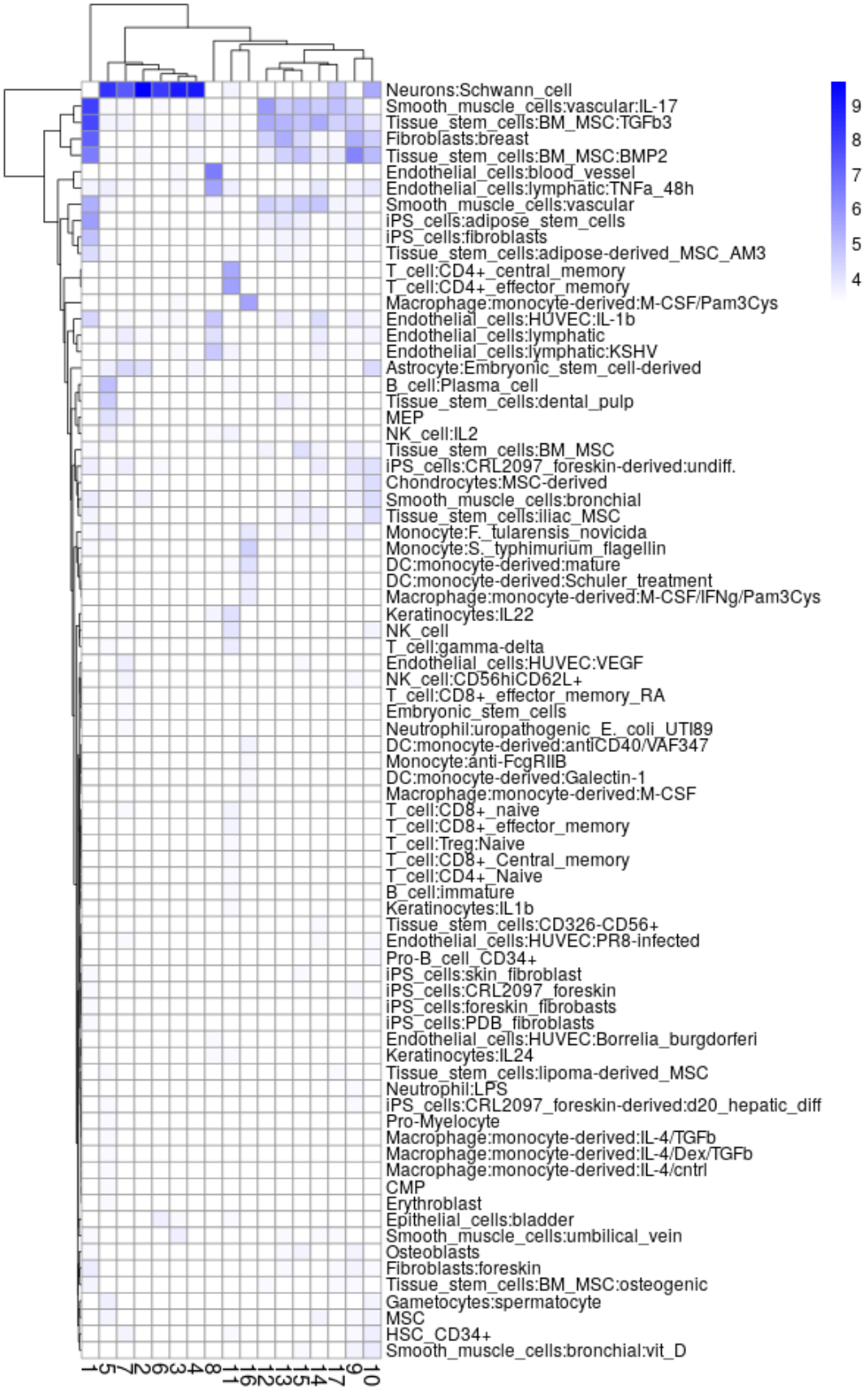

Data S5.12. Heatmap representing the annotation scoring obtained of each cluster with singleR package of 23PNF.

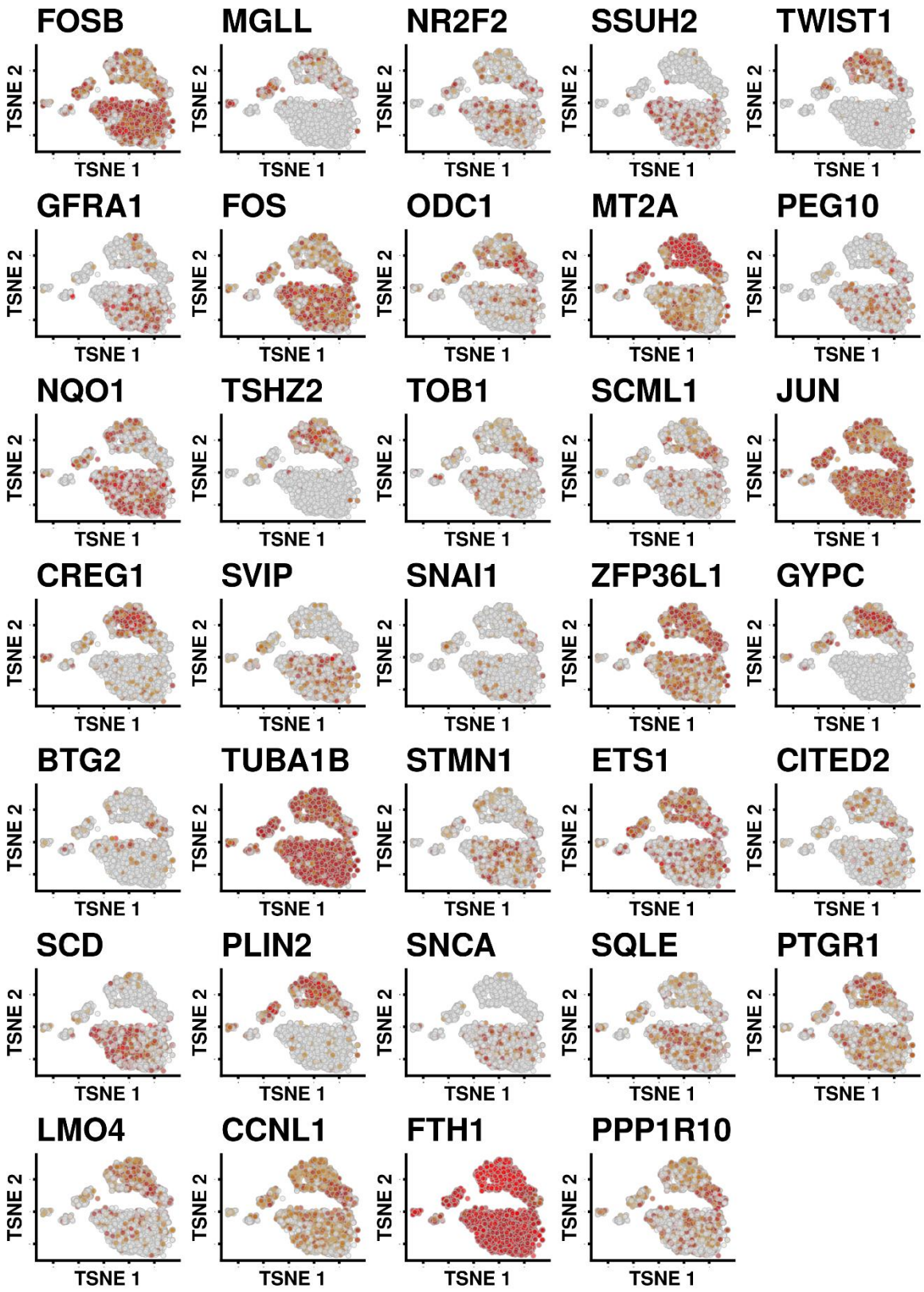

Data S5.13. 23PNF TSNE representation of single-cell RNA-seq of NC roadmap markers.

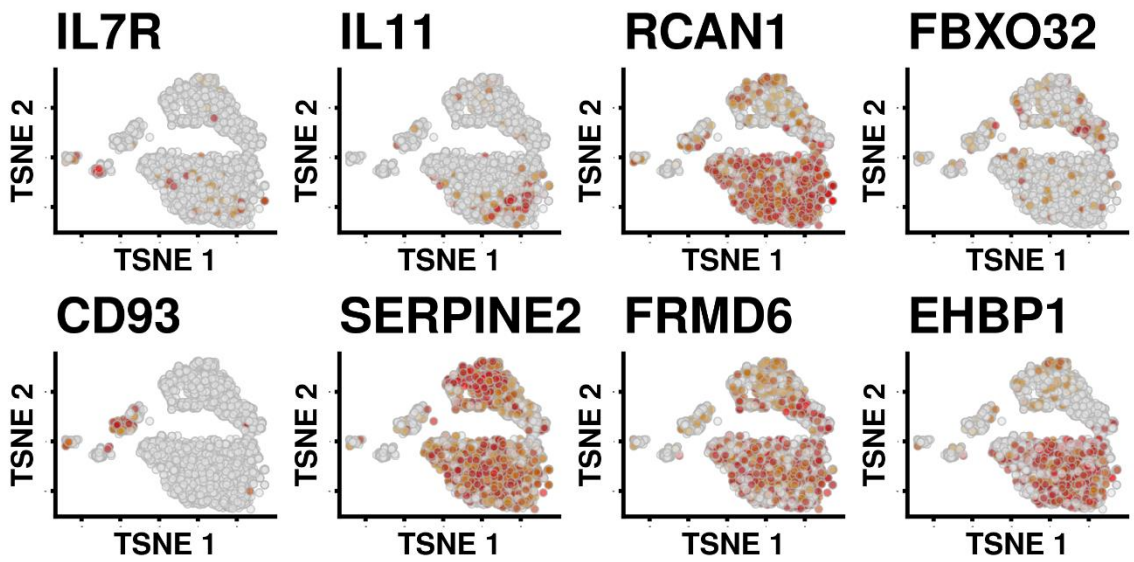

Data S5.14. 23PNFTSNE representation of single-cell RNA-seq of day 7 roadmap markers.

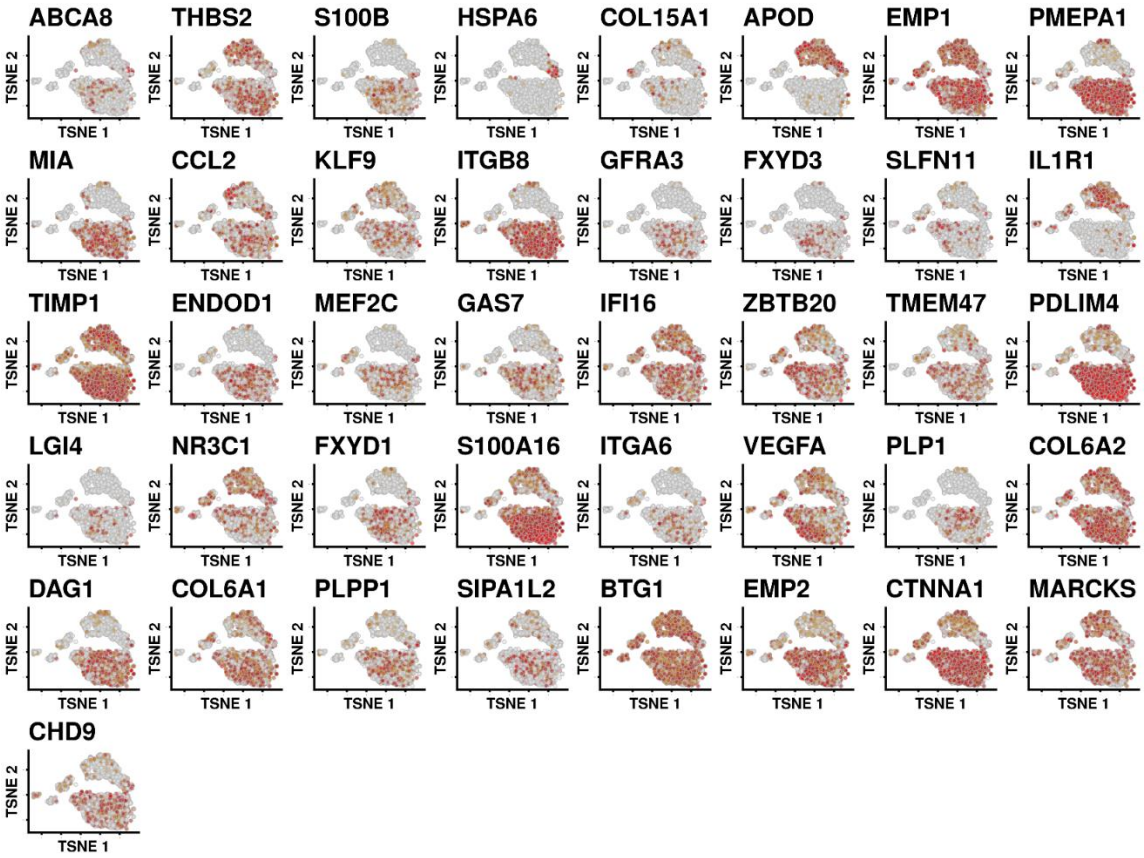

Data S5.15. 23PNF TSNE representation of single-cell RNA-seq of day 30 roadmap markers.